DISSERTATION

Interaction of Titanium Dioxide Surfaces with Liquid Water

Ausgeführt zum Zwecke der Erlangung des akademischen Grades eines Doktors der technischen Wissenschaften unter der Leitung von

Univ.Prof. Dr.techn. Ulrike Diebold

und

Ao.Univ.Prof. Dr.techn. Michael Schmid

Institut für Angewandte Physik E134

eingereicht an der Technischen Universität Wien
Fakultät für Physik

von

Ing. Jan Balajka

01328696
Siccardsburggasse 27/14
1100 Wien

Wien, August 2018

Acknowledgement

I take this opportunity to express my gratitude to everyone who supported me during my PhD study.

First of all, I would like to thank my supervisor Ulrike Diebold for being a great advisor, always helpful and interested even in small everyday problems. Thank you for giving me the freedom to learn by doing. I would like to express my appreciation to Michael Schmid for being the person to ask when the instruments were not working or when I could not make sense out of the data. I am grateful to Gareth Parkinson for the opportunity to participate on his projects, Stijn Mertens for sharing his knowledge on electrochemistry, Martin Setvín and Margareta Wagner for teaching me the laboratory practice of ultrahigh vacuum surface science. Many thanks to Jiří Pavelec for his creative solutions and for helping me with various projects. I thank all the students and colleagues whom I had the chance to work with, mainly Zdeněk Jakub, Mojmír Komora, Alex Riss, Jan Hulva and Florian Kraushofer, and all group members for creating a stimulating yet friendly environment. Many experiments would not have been possible without Rainer Gärtner and Herbert Schmidt who turned ideas into real objects.

I gratefully acknowledge financial support by the European Research Council (ERC) Advanced Grant "OxideSurfaces", and the Austrian Science Fund FWF Wittgenstein prize and Doctoral College "Solids4Fun".

Much of the work was possible due to a fruitful collaboration. For that, I would like to thank Melissa Hines, Will DeBenedetti, Ulrich Aschauer and Annabella Selloni.

I am grateful to Miquel Salmeron and Martin Sterrer for kindly agreeing to review this thesis.

Finally, I thank my family and Anna for supporting me during my studies.

Abstract

Metal oxides are an important class of materials as most metals spontaneously develop an oxide layer in ambient conditions. These materials are not only abundant, but also offer a wide range of interesting properties. A prototypical example is titanium dioxide (TiO_2), which is utilized in many industrial applications such as in photocatalysis, dye-sensitized solar cells, and heterogeneous catalysis.

At present, the surfaces of TiO_2 are well understood under highly idealized ultra-high vacuum (UHV) conditions. In reality, however, surfaces are surrounded by gases and covered with liquids. Many practical processes involve a solid surface immersed in an aqueous solution. In air, surfaces are automatically covered by a thin film of condensed water. It is often the solid-liquid interface that defines the performance of a material in application. Understanding atomic scale processes closer to real conditions is essential for a rational design of materials, and further improvement and increased efficiency in applications.

The investigation of surfaces under ambient conditions remains a challenge due to the restricted number of available experimental techniques and a high risk of contamination. We have designed an experimental apparatus that allows dosing ultrapure liquid water on the surface of a sample (typically a single crystal) without exposure to air. The apparatus is coupled to an existing surface-science chamber, which enables reproducible sample preparation and sample characterization by UHV-based analytical techniques.

Within the thesis, the interaction of liquid water with the two lowest-energy terminations of TiO_2 rutile was studied. The (110) surface was found to retain its bulk-terminated (1×1) structure upon immersion in pure liquid water. In addition, we clarified the origin of a molecularly ordered overlayer previously reported by several research groups. This overlayer consists of a mixture of carboxylates, and, upon exposure to air, spontaneously forms on the surface. Despite their relatively low atmospheric concentration, carboxylic acids adsorb on TiO_2(110) with a high affinity and block the undercoordinated surface cation sites.

In contrast, the (011) termination of TiO_2 rutile was identified to change its surface structure upon contact with liquid water. As predicted by DFT calculations, the

original (2×1) reconstruction was lifted, and dissociated water remained on the unreconstructed (1×1) surface in the form of an ordered (2×1) overlayer. Apart from detailed experimental results, the thesis also covers the design of the UHV-compatible apparatus for dosing pure liquid water, a brief description of the used techniques and a short introduction into the investigated surfaces.

Kurzfassung

Metalloxide sind eine wichtige Materialklasse, da sich auf den meisten Metallen unter Umgebungsbedingungen spontan eine Oxidschicht ausbildet. Diese Materialien sind nicht nur reichlich vorhanden, sondern bieten auch eine breite Palette interessanter Eigenschaften. Ein prototypisches Beispiel ist Titandioxid (TiO_2), das in vielen industriellen Anwendungen wie der Fotokatalyse, in Farbstoffsolarzellen und der heterogenen Katalyse eingesetzt wird.

Zur Zeit sind die Oberflächen von TiO_2 unter hoch idealisierten Ultrahochvakuumbedingungen (UHV) gut verstanden. In Realbedingungen sind die Oberflächen jedoch von Gasen umgeben und mit Flüssigkeiten bedeckt. Viele praktische Verfahren verwenden die Oberfläche eines Festkörpers, der in eine Wasserlösung eingetaucht ist. In der Luft sind Oberflächen automatisch von einem dünnen Kondenswasserfilm bedeckt. Es ist oft diese Fest-Flüssig-Grenzfläche, die das Verhalten eines Materials in der Anwendung definiert. Das Verständnis der Prozesse auf atomaren Maßstab ist wesentlich für die zielgerichtete Entwicklung von Materialien, um die Effizienz in Anwendungen weiter zu steigern und zu verbessern.

Die Untersuchung von Oberflächen unter Umgebungsbedingungen bleibt aufgrund der begrenzten Anzahl verfügbarer experimenteller Methoden und einer hohen Wahrscheinlichkeit einer Kontamination eine Herausforderung. In dieser Dissertation wurde eine Versuchsapparatur entwickelt, die es ermöglicht, hochreine Flüssigkeiten ohne Lufteinwirkung auf die Oberfläche einer Probe (typischerweise eines Einkristalls) zu dosieren. Diese Apparatur ist mit einer vorhandenen Ultrahochvakuum (UHV)-Kammer gekoppelt, die eine reproduzierbare Probenpräparation und Probencharakterisierung mit UHV-basierten Analysemethoden ermöglicht.

In dieser Arbeit wurde die Wechselwirkung von flüssigem Wasser mit den beiden niederenergetischen Orientierungen von Rutil TiO_2 untersucht. Es stellte sich heraus, dass die (110)-Oberfläche ihre Volums-terminierte (1×1) Struktur beim Eintauchen in reines flüssiges Wasser beibehält. Darüber hinaus wurde den Ursprung einer molekular geordneten Überstruktur geklärt, über die bereits von mehreren Forschungsgruppen berichtet wurde. Diese Überstruktur besteht aus einer Mischung aus Carboxylatgruppen und bildet sich bei Kontakt mit Luft spontan auf der Oberfläche. Trotz ihrer relativ niedrigen Konzentration in der Atmosphäre adsorbieren die Carbonsäuren an TiO_2 (110) mit einer hohen Affinität und blockieren die unterkoordinierten Oberflächenkationen.

Im Gegensatz dazu wurde auf der (011)-Orientierung von Rutil TiO_2 eine Veränderung der Oberflächenstruktur bei Kontakt mit flüssigem Wasser gefunden. Wie durch auf Dichtefunktionaltheorie basierende Berechnungen vorhergesagt, wird die ursprüngliche

(2×1)-Rekonstruktion aufgehoben und dissoziiertes Wasser adsorbiert auf der unrekonstruierten (1×1)-Oberfläche in einer geordnete (2×1) Überstruktur.

Neben den detaillierten Versuchsergebnissen umfasst die Arbeit auch das Design der UHV-kompatiblen Apparatur zur Dosierung von reinem flüssigem Wasser, eine kurze Beschreibung der verwendeten Methoden und eine kurze Einführung in die untersuchten Oberflächen.

Contents

1 Introduction **1**

1.1 Metal oxides . . . 1

1.2 Titanium dioxide . . . 3

1.2.1 TiO_2 rutile surfaces . . . 4

1.3 Solid-liquid interfaces . . . 5

1.4 Research objective of the thesis . . . 7

2 Experimental Techniques and Setups **9**

2.1 Experimental techniques . . . 9

2.1.1 Scanning tunneling microscopy . . . 9

2.1.2 X-ray photoelectron spectroscopy . . . 13

2.1.3 Low-energy electron diffraction . . . 18

2.1.4 Low-energy ion scattering . . . 20

2.1.5 Preparation of oxide single crystals . . . 21

2.2 Experimental setups . . . 22

2.2.1 Omega chamber . . . 22

2.2.2 LT-STM chamber . . . 37

3 Apparatus for dosing liquid water in ultrahigh vacuum **39**

3.1 Vapor pressure of H_2O . . . 40

3.2 Experimental setup . . . 40

3.2.1 Water drop chamber . . . 41

3.2.2 Cold finger . . . 45

3.3 Experimental procedure . . . 50

3.3.1 Cleaning of the H_2O supply . . . 52

3.3.2 ”Steam-washing” of the drop chamber . . . 54

3.3.3 Growth of icicles . . . 56

3.3.4 Liquid H_2O dosing . . . 56
3.3.5 Pumping out . . . 58
3.3.6 Repeated use of the cold finger . . . 58
3.4 Purity evaluation . . . 60
3.5 Limits and potential improvements . . . 62
3.6 Other possible applications . . . 64

4 Interaction of TiO_2 rutile (110) with liquid H_2O and air 67
4.1 Introduction . . . 67
4.2 Results . . . 68
4.2.1 Clean liquid H_2O . . . 68
4.2.2 Identification of impurities . . . 69
4.2.3 Reactions of gases with liquid H_2O . . . 76
4.3 Discussion . . . 79
4.4 Conclusion . . . 81

5 Interaction of TiO_2 rutile (011) with H_2O 83
5.1 Introduction . . . 83
5.2 Experimental results - liquid H_2O . . . 85
5.2.1 Structure after liquid H_2O exposure . . . 85
5.2.2 Surface spectroscopy . . . 88
5.3 Computational results - dissociated water on TiO_2(011) . . . 91
5.4 Discussion - liquid H_2O . . . 92
5.5 Low-temperature adsorption of H_2O . . . 96
5.6 Segregation of impurities on rutile TiO_2(011) . . . 98
5.7 Conclusion . . . 102

6 Summary and outlook 103

References 107

Chapter 1

Introduction

1.1 Metal oxides

Metal oxides are vital to many technological processes due to the wide range of diverse properties. Materials of this class span the range from the best insulators (*e.g.*, Al_2O_3) and semiconductors (*e.g.*, TiO_2) to metal-like conductive (*e.g.*, Fe_3O_4) and superconductors (*e.g.*, $YBaCu_3O_7$).[1] Different oxides exhibit various magnetic properties such as diamagnetism (MoO_2), paramagnetism (RuO_2), ferromagnetism (CrO_2) or antiferromagnetism (NiO). They are used as heterogeneous catalysts or as a support for dispersed metal catalyst in diverse chemical reactions.

Metal oxides are the most earth-abundant inorganic materials,[2] and typically robust under reaction conditions. An oxide is the lowest-energy state of most metals in air.[1] The majority of metals are therefore spontaneously oxidized at the surface when exposed to the ambient, while the thickness of the oxide layer depends on conditions such as temperature, partial oxygen pressure and time of exposure. Generally undesirable corrosion of metals mostly involves formation of oxides at the surface.[1] As all solid materials interact with their surroundings through their surfaces, investigations of oxide surfaces are interesting from both applied and fundamental points of view.

Bulk structure of oxides can be rather complex, and many metals form several oxides with different stoichiometry and structure. Most metal oxides, however, adopt one of the following five forms:[3] rocksalt (*e.g.*, MgO), rutile (*e.g.*, TiO_2), corundum (*e.g.*, α-Fe_2O_3), wurtzite (*e.g.*, ZnO) or perovskite (*e.g.*, $SrTiO_3$).

While the bulk structure of most crystalline materials has been accurately estab-

lished with X-ray crystallography, the knowledge of exact geometric surface structures is still limited.[1] At the surface, the bulk symmetry of a crystal is interrupted, and atoms at the surface relax and may reconstruct to minimize the surface free energy. The structure, but also electronic properties at the surface can thus differ substantially from those of the bulk. The situation is even more complex when the surface is covered with adsorbates, exposed to high-pressure gases, or in contact with liquids. Different chemical reactions can occur due to the rich variety of surface sites and the ability of surface cations to assume different valence states.[3] Despite the undisputed importance of surfaces, only a small fraction of the atoms of a solid reside at the surface. The concentration of atoms at the surface (typically in the order of 10^{16} atoms cm^{-2}) is considerably lower that the population of bulk (10^{23} atoms cm^{-3}).[4] Therefore, surface-sensitive analytic techniques need to enhance the signal contribution from the topmost atomic layers.[5] However, techniques capable of high surface sensitivity have been developed and are now routinely used (some are described in chapter 2).

Investigations of oxide surfaces present additional challenges compared to elemental solids, such as metals. The main difficulty when working with oxides in an ultrahigh vacuum is the surface preparation.[1,6] Reproducible preparation of geometrically ordered surfaces with a controlled stoichiometry requires an established procedure. The preparation procedure has to be found for each new compound, often by trial and error, and can generally differ among different phases or terminations of the same material.[1] Even then the stoichiometry and structure are not necessarily representatives of those of bulk.

In many cases, surface preparation induces defects in the surface, which may have profound effect on structure and chemical reactivity of surfaces.[1,2,7] Point defects, representing deviations from long-range periodicity of crystal lattice, often control electrical, optical, and many other properties of materials.[8] Small changes in stoichiometry result in so-called intrinsic defects; oxygen and metal vacancies or interstitials.[2] These defects change the density of charge carries, which can dramatically alter the conductivity. The most common point defect on oxides under reducing conditions is an oxygen vacancy.[3] The vacancy lowers the coordination of the surrounding metal cations, thus providing a highly reactive site for some chemical reactions.

Defects, however, do not need to be unwanted side-effects in surface investigations. They can be intentionally introduced and actively controlled in order to en-

gineer a material with better performance in applications.[2,8]

1.2 Titanium dioxide

Titanium dioxide (TiO_2) has become a prototypical oxide material in surface science due to its applications in many fields, and the ease of preparation.[9] TiO_2 crystallizes in three main forms: the thermodynamically stable rutile phase, and metastable anatase and brookite phases. Both metastable phases irreversibly convert to rutile upon annealing at high temperature.[10,11] The bulk structure is usually explained in terms of Ti^{4+} ions in the center of slightly distorted octahedra, surrounded by six O^{2-} ions in the corners.[12] These octahedra can be considered the basic building units of the lattice. Each octahedron shares corners with neighboring octahedra rotated by 90° and additionally, it shares edges with the two adjacent, parallel octahedra on each side (see Fig. 1.1). The unit cell is tetragonal with dimensions a=b=4.584 Å, c=2.953 Å.[9]

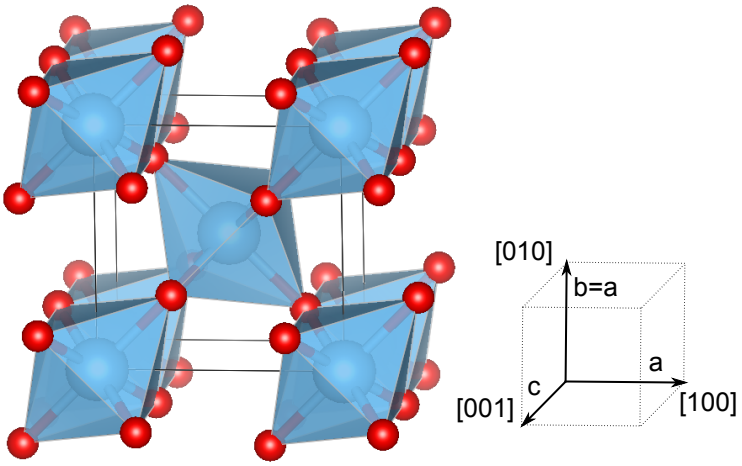

Figure 1.1 | Bulk structure of TiO_2 rutile. Titanium (blue, Ti^{4+}) ions are in the center of tetrahedra, surrounded by oxygen (red, O^{2-}) ions in the corners. Directions of the tetragonal lattice are shown in the right.

With a bandgap of 3.0 eV (for rutile, 3.2 eV for anatase),[9] TiO_2 is insulating when stoichiometric. However, intrinsic defects, such as oxygen vacancies, generate excess electrons and thus provide conductivity. The reduction of the bulk introduces states in the band gap, reflected by a color change from initially transparent in case of a stoichiometric crystal to dark blue for a reduced crystal.[2,13] Extra conductivity can be

provided by extrinsic defects, such as donor impurities or dopants. Natural crystals often contain trace impurities of Fe, Nb, Ta, Ca, or Mg, which gives rise to a variety of colors of mineral samples.[14]

Pure TiO_2 is white in powder form due to its high refractive index (2.9),[15] and it is used as a pigment in paints. Due to its nontoxicity and biocompatibility, titania is used in biomedical implants, cosmetic products, and food colorants. Titanium dioxide gained considerable popularity as a photocatalytic material.[16] Its semiconducting nature enables efficient generation of electron-hole pairs by exciting valence electrons to the conduction band upon irradiation with light. A certain fraction of these photo-generated charge carriers travel to the surface without recombination, where they can initiate chemical reactions. An important example of such a process is photocatalytic water splitting.[17] In this process, oxygen and hydrogen are generated from water on the irradiated TiO_2 surface without applying an electric potential. Similarly, photo-excited charge carriers can react with adsorbed water and oxygen to produce radical species. These species then cause degradation of organic compounds adsorbed on the surface, eventually leading to the production of CO_2 and H_2O as the final decomposition products.[9] Photo-assisted degradation of organic pollutants is at the heart of the self-cleaning properties of TiO_2 utilized in environmental remediation such as air and water purification, bactericidal and protective coatings.[18,19]

A major limitation of TiO_2 as a photocatalyst is that only a small fraction of sunlight is harvested. Irradiation by near-UV light (<400 nm) is needed to excite electron-hole pairs, which is due to the relatively wide bandgap of TiO_2. The efficiency was successfully improved by doping TiO_2 with cations or anions or by functionalizing the titania surface with light-absorbing dyes matching the frequency spectrum of natural sunlight.[20] TiO_2 also finds use as a solid-state gas sensor, as its electrical conductivity responds to the pressure of oxygen in surrounding environment and changes upon adsorption of molecules on the surface. Other oxides such as ZnO and SnO_2, however, are used more extensively for this purpose.

1.2.1 TiO_2 rutile surfaces

The (110) surface is the most stable termination of TiO_2 rutile with the lowest surface free energy.[21] The surface exhibits a bulk-terminated structure with minor relaxations. Two kinds of titanium atoms and two kinds of oxygen atoms are found

on the surface, all arranged in rows along the [001] direction. The rows of five-fold coordinated titanium (Ti_{5c}) with a dangling bond perpendicular to the surface are neighboring the bulk-like three-fold coordinated oxygen (O_{3c}) rows (see Fig. 1.2a). On top of six-fold coordinated Ti atoms (Ti_{6c}, as in the bulk) are two-fold coordinated oxygen atoms (O_{2c}) physically protruding from the surface. Some of these so-called bridging oxygens (O_b), are removed during sample preparation in UHV, resulting in oxygen vacancies (V_O). Although the (110) surface is very stable and non-polar, reconstructions occur upon annealing in oxidizing or reducing conditions.[9,13,22]

The second lowest energy surface, the (011) surface, exhibits rather different structure (Fig. 1.2b). In ultrahigh vacuum, the surface forms a (2×1) reconstruction terminated by *zig-zag* rows of two-fold coordinated oxygen atoms, asymmetrically bonded to five-fold titanium atoms.[23] Reduced samples exhibit oxygen vacancies and pairs are frequently observed.[24] Both surfaces are discussed in more detail within the context of following chapters.

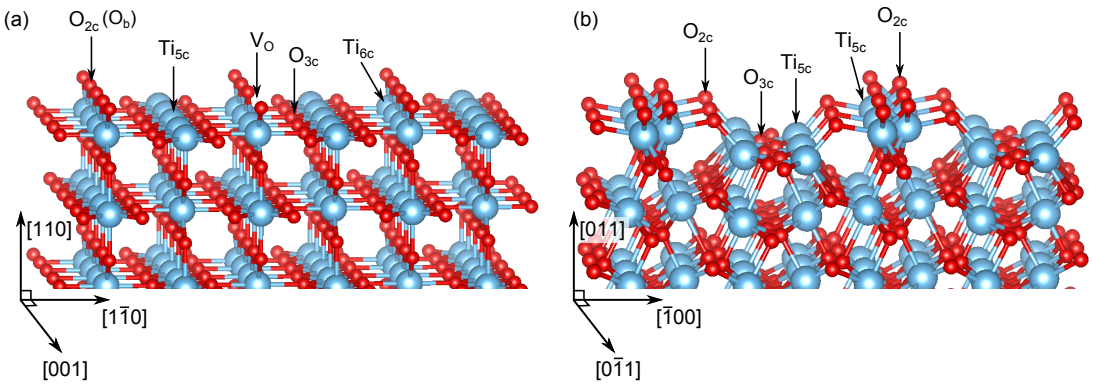

Figure 1.2 | Atomic models of lowest-energy rutile TiO_2 surfaces. (a) (110) surface, **(b)** (011)-(2×1) surface based on coordinates from Ulrich Aschauer.

1.3 Solid-liquid interfaces

Although much of the knowledge on surfaces has been acquired in ultrahigh vacuum, these represent model studies under highly idealized conditions. Real processes, however, take place at the interfaces with gases and liquids. In many large-scale industrial procedures such as electrolysis, galvanization, and passivation, solids are immersed in aqueous solutions.[25] The fine details of the interface determine macroscopic properties of materials such as wetting, corrosion resistance, or its perform-

ance in chemical and catalytic reactions. The phenomena at solid-liquid interface govern many natural processes in meteorology and geochemistry.[26] In ambient, surfaces are spontaneously covered with a thin water film formed by condensation of atmospheric humidity.[27] In practice, most surfaces are covered with water, and TiO_2 is not an exception.

The interaction of water with various classes of solids has been studied extensively.[26,28–30] Most of the investigations, however, were conducted under UHV conditions. Only recently, several reports studied the interface between solution and oxide surface.[31–35] However, such studies are still relatively sparse, mainly for practical reasons. Water does not exist as a liquid in vacuum without background H_2O pressure. Liquid water inserted in vacuum would instantly evaporate and freeze due to the sudden heat loss. On the other hand, many surface-science techniques are based on charged or neutral particles (ions, electrons, or atoms). As these particles strongly interact with gas environment, conventional particle-based techniques are restricted to UHV. Some technical solutions to overcome this limitation are outlined in the following chapters. There are two possible ways to investigate the properties of solid-liquid interfaces, namely *in-situ* or *ex-situ*.[25] While the *in-situ* approach has the undoubted advantage of investigating the interface directly under realistic conditions, the number of available experimental techniques is limited. The *ex-situ* approach takes advantage of a wide range of UHV-based techniques. However, the possibility has to be taken into account that changes may occur to the surface between the experiment and the analysis. Both approaches are experimentally challenging if one does not want to sacrifice the degree of control that is provided in UHV studies.[9] It is a major concern and challenge to perform these experiments in a sufficiently clean way. Due to the very high doses involved, impurities that are present at even very low concentrations might become significant.

Surface-science experiments with liquids and high-pressure gases are essential to test the relevance of the knowledge acquired in UHV for practical applications.[9] They can provide insights about the stability of defects under high-pressure environment, and examine their anticipated high importance for adsorption and chemical reactions.[9] The so-called bridging of the pressure gap[36] is necessary to investigate structure-reactivity relations in chemical reactions. As demonstrated in the literature, results acquired in UHV do not necessarily apply to the solid-liquid interface. An example of such pressure gap is a high water pressure threshold for hydroxylation of

regular $Fe_3O_4(001)$ surface sites,[37] while at low pressures [$p(H_2O)<10^{-4}$ Torr], water dissociated only at the defects.

The experiments conducted within the thesis utilized the *ex-situ* approach to bring a single-crystalline sample in contact with liquid H_2O combined with sample preparation and analysis in UHV. A number of similar setups were reported in the literature, which combine an electrochemical cell with a UHV chamber for *ex-situ* analysis and reliable sample preparation. These systems are utilized to perform electrochemical measurements on well-defined (mostly metal) electrodes characterized at the atomic scale. Sample transfer directly from a cell to the UHV enabled to capture the actual state of the surface during the electrochemical experiment. These are generally referred to as *emersion* experiments.[38] In practice, samples were transferred from a UHV chamber into a separate chamber and sealed off by various mechanisms. One possibility is pressing the manipulator against a sealing surface[39] or passing the polished manipulator through differentially pumped O-rings.[40,41] If samples were mounted on an exchangeable holder, they could be handed over to another manipulator inside the side chamber and separated by a valve from the UHV. After venting (typically with air or inert gas) the sample was either transferred through another valve to an external electrochemical cell, or the cell itself was introduced into the vented compartment. In electrochemical measurements, samples are commonly facing down in so-called hanging meniscus configuration.[42–45] This geometry allows to establish the contact with an electrolyte only at the surface of a flat sample. Other designs work with a flow of the electrolyte across the sample,[46,47] with the advantage that the sample can be easily rinsed with clean water before re-insertion to UHV. Comprehensive reviews of other variants of electrochemical cells attached to a UHV chamber are provided in refs. [38, 48].

1.4 Research objective of the thesis

The aim of the thesis is to investigate the surfaces of technologically important TiO_2 material under realistic conditions. The liquid water environment was selected as a representative of these conditions. While this environment is only one step towards the complex conditions of real systems in applications, such experiments are essential for further considerations. Experiments with liquid water substantially deviate from the typical practice of surface science, and results need to be interpreted

with caution due to the high chance of experimental artifacts such as impurities.

The results obtained in experiments with liquid water on the (110) and (011) surfaces of TiO_2 are summarized in following chapters as well as a description of the experimental equipment used, including the design of an apparatus for dosing liquid water in UHV-compatible conditions.

Chapter 2

Experimental Techniques and Setups

This chapter briefly describes the basic principles of experimental techniques used within the thesis. A detailed description of the used experimental setups is in the second part of the chapter.

2.1 Experimental techniques

2.1.1 Scanning tunneling microscopy

Scanning tunneling microscopy (STM) is an imaging technique that allows to analyze a surface at the atomic scale directly in real space. Since the invention by Binnig and Rohrer,[49] it became one of the main techniques for the determination of structural and electronic properties of surfaces. An STM setup consists of a sharp metallic tip placed in close proximity of the sample (at a distance of a few Å). When a bias voltage (typically in the range from mV to a few V) is applied between the sample and the tip, electrons have a certain probability of penetrating the vacuum gap between the tip and the sample; this phenomenon is known as quantum tunneling effect. To explain the physical principle of STM, a simplified case of electron tunneling through a one-dimensional rectangular potential barrier is often considered.[50–52] For electrons near the Fermi level, the height of the barrier (minimum energy required to escape the potential well) is the work function ϕ as indicated in Fig. 2.1. In quantum-mechanical representation, an electron is described by a wave function ψ that satis-

fies the one-dimensional, time-independent Schrödinger equation

$$\left(-\frac{\hbar^2}{2m}\frac{d^2}{dz^2} + V(z)\right)\psi(z) = E\psi(z)\,, \tag{2.1}$$

where $\hbar$=1.05 × 10^{-34} m^2 kg s^{-1} is the reduced Planck constant, m=9.11 × 10^{-31} kg is the electron mass, z is the position coordinate, V is the potential energy barrier and E is the total energy of the electron. Inside the tip or the sample (regions A and C in Fig. 2.1) the energy of electron fulfills $E > V(z)$, and the solution of equation 2.1 is a travelling wave function

$$\psi(z) \propto \exp(\pm ikz), \quad \text{where} \quad k = \frac{\sqrt{2m(E-V)}}{\hbar} \tag{2.2}$$

is the wave vector. In general, the potential might not be constant across the barrier as indicated in Fig. 2.1a. However, for simplicity, we substitute the potential in the gap with its average value and consider only a rectangular barrier. Inside the barrier (region B in Fig. 2.1), the energy of electron $E < V(z)$ and the solution of the equation 2.1 is an exponentially decaying wave function:

$$\psi(z) \propto \exp(-\kappa z), \quad \text{where} \quad \kappa = \frac{\sqrt{2m\phi}}{\hbar} \tag{2.3}$$

is the decay constant. Here we used the fact that for the states at Fermi level $V-E$ is the work function ϕ. The probability that electron resides at position z is proportional to $|\psi(z)|^2$ which has a nonzero value inside the barrier and therefore a certain probability to penetrate the barrier. The tunneling current decays exponentially with barrier width (tip-sample distance) d as

$$I \propto |\psi(d)|^2 \propto \exp(-2\kappa d). \tag{2.4}$$

For typical values of the work function of metals (3–5 eV), the tunneling current increases by nearly one order of magnitude for every 1 Å decrease in tip-sample distance. Assuming that the current can be measured with less than 1% error, a vertical (z) resolution in the pm range can be achieved. The exponential decay of the tunneling current over distance is the reason for the high resolution of STM and its ultimate surface sensitivity. The atoms located higher on the tip or deeper under the surface

have a negligible contribution to the tunneling current, as the tunneling probability is substantially lower. In a simplified case that the tip and the sample are electrically connected without an applied voltage, Fermi levels are aligned and electrons can tunnel in both directions with equal probability. A nonzero net tunneling current occurs when bias voltage U, is applied. In Fig. 2.1, the electrons occupying the states with energy in the range between $E_{\mathrm{F,tip}} - eU$ and $E_{\mathrm{F,tip}}$ can tunnel through the gap into the empty states of the sample.

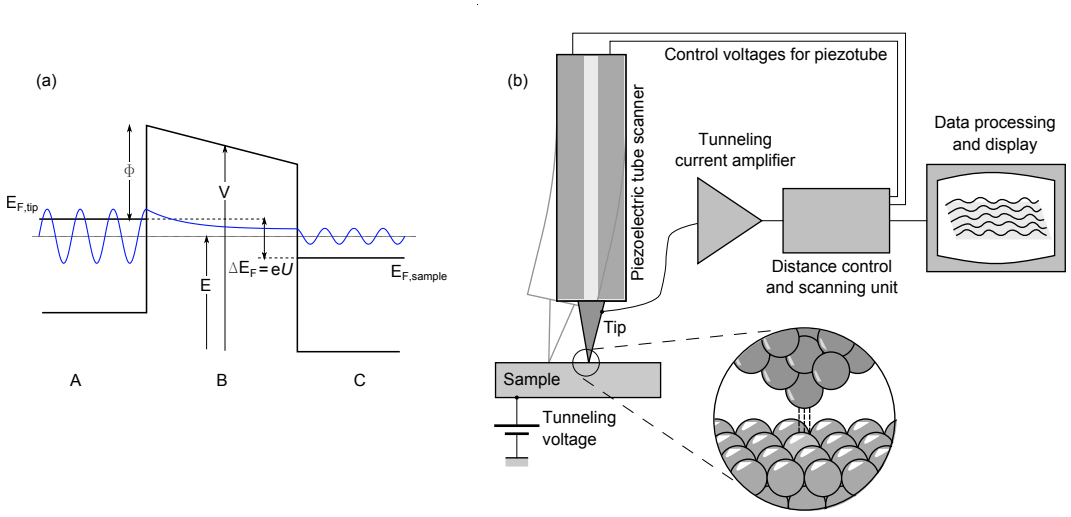

Figure 2.1 | Principle of scanning tunneling microscope. (a) Diagram of electron tunneling through a potential barrier, the potential is marked with the solid black line, and the electron wave function with a blue line. **(b)** Schematic of STM setup, adapted and reprinted from ref. [53] with permission of Michael Schmid.

Contrast in STM

Depending on the polarity of the bias voltage, electrons can tunnel either from the tip into the sample (into the empty states of the sample) or from the filled states of the sample into the tip. In an STM experiment, the tip scans across the surface at a constant bias voltage and the tunneling current is stored as a function of position in the form of a 2D image. Instead of keeping the tip at a fixed distance and recording the tunneling current (constant height mode), the height of the tip can be actively varied via a feedback loop to maintain a pre-set current value (constant current mode). When the tip is at a position $\mathbf{r}$ of the surface, the tunneling current is directly proportional to the number of sample states within the energy interval eU,

responsible for the tunneling current[50]:

$$I \propto \sum_{E_F - eU}^{E_F} |\psi(\mathbf{r})|^2 \exp(-2\kappa \mathbf{d}). \tag{2.5}$$

This restricts the use of STM to the analysis of conductive surfaces (metals, some semiconductors), while for insulators the tunneling current (eq. 2.5) would be zero. STM, therefore, does not give a direct image of the surface topography. Instead, an STM image is a convolution of topography and local density of states (LDOS) near the Fermi level. For small bias voltages ($eU \ll \phi$) the tunneling current can be expressed as:[51]

$$I \propto U \rho_S(\mathbf{r}, \mathbf{E}_F)\,, \tag{2.6}$$

where $\rho_S(\mathbf{r}, \mathbf{E}_F)$ is the LDOS at Fermi level and at the current tip position on the sample surface.

The nature of STM allows not only to image the structure but also achieve chemical contrast,[54] as was demonstrated, e.g., by imaging PtRh alloy single crystal in ref. [55]. Here, Rh atoms appeared brighter than Pt atoms and the chemical ordering on the surface could be studied at the atomic scale. On other surfaces, electronic effects dominate over the geometric structure and lead to phenomena such as inverted contrast, as exemplified on rutile TiO_2(110) surface. This prototypical oxide surface is terminated by rows of bridging oxygen atoms. Although geometrically protruding, the bridging oxygen atoms are imaged as dark with STM while lower-lying surface titanium atoms are imaged as bright.[56] An oxygen vacancy, a common defect formed after UHV sample preparation is imaged as a bright protrusion in STM,[56] while with noncontact AFM it appears as a dark depression.[2]

Technical aspects of STM

For the tunneling to occur, the tip has to be controllably approached to the sample at very small separation. The high resolution of STM requires to control of the tip position with pm precision. The accurate tip position is controlled in three dimensions by a scanner with piezoelectric drivers. A piezoelectric material responds to an applied voltage with a reproducible elongation or contraction depending on the polarity of the applied voltage. It is also the voltage applied to a piezoelectric driver which

is stored in an STM image as the quantity representing the tip height in constant-current mode. Piezoelectric drivers are also used for scanning during image acquisition. By applying a sawtooth voltage signal in one direction and voltage ramp in the perpendicular direction, the tip is scanned in the xy plane. In various designs, either the tip or the sample can be scanned while the other one is stationary.

Atomic resolution in STM also requires high mechanical stability and the need to eliminate possible vibrations. The corrugation detected by STM is in the order of 10-100 pm,[50,57] while typical floor vibrations in a laboratory environment are in the range of μm.[57] The amplitude of external mechanical disturbances has to be reduced well below the level of atomic corrugation before it has a chance to couple to the relative motion inside the STM. This is typically achieved by a rigid construction of the STM itself and by multi-stage vibration-isolation systems. Common approaches are springs or pneumatic suspensions, stacks of metal plates (heavy, high resonance frequency) separated by elastomer pieces (*e.g.*, Viton, high internal damping, and low resonance frequency), or by eddy-current damping.

STM can also be operated under rather extreme conditions out of ultrahigh vacuum. Several designs involve high pressure of gases[58] and combine it with heating of the sample to high temperature during imaging, in order to study surfaces of catalysts at industrial conditions.[59–61] Other STM instruments allow for imaging the surface immersed in liquid, *e.g.*, in an electrolyte under electrochemical potential control.[62,63] Some groups employ high-speed STMs to study dynamic processes at surfaces such as growth, etching, adsorption, and surface chemical reactions.[64,65]

2.1.2 X-ray photoelectron spectroscopy

X-ray photoelectron spectroscopy (XPS) is a frequently used technique for the quantitative analysis of surface chemical composition. In this technique, electrons are ejected from core levels upon absorption of an X-ray photon of energy $h\nu$, where ν is the frequency of the photon. The energy distribution of the emitted electrons is analyzed by an electron spectrometer. An XPS spectrum is then a plot of intensity (typically counts or counts per second) as a function of the kinetic energy E_K of detected electrons. As the excitation energy $h\nu$ is known, the binding energy E_B w.r.t.

Fermi level of the electrons can be obtained by direct subtraction:

$$E_B = h\nu - E_K - \phi_A \,, \tag{2.7}$$

where ϕ_A is the work function of the analyzer. The set of binding energies within a spectrum is a unique identifier of the presence of a chemical element in the investigated sample. In principle, XPS maps the filled states of an element, as all electrons, whose binding energy is less than the incident photon energy, will contribute to the spectrum. The electrons, if they escape without losing energy, form sharp characteristic peaks of the spectrum. The secondary electrons, which have lost part of their energy on their way out of the sample (inelastically scattered) create the continuous background superimposed on the primary spectral lines. The photoemission process is schematically shown in Fig. 2.2. Here an electron is ejected from a core level by the incident X-ray beam. In addition to the binding energy, the electron has to overcome the work function of the sample ϕ_S to escape to the vacuum. The kinetic energy of the emitted electron outside the sample is $E_{K,0}$. The electron is then detected with the analyzer whose work function is generally different than that of a sample.[4] As the sample and the detector are electrically connected, their Fermi levels equilibrate and the electron is accelerated or retarded by a contact potential difference $\phi_S - \phi_A$ to the kinetic energy E_K. Only the analyzer work function plays a role in equation 2.7. In practice, the energy scale of the analyzer is calibrated such that the binding energy of electrons emitted from the Fermi edge (the highest kinetic energy) corresponds to zero.

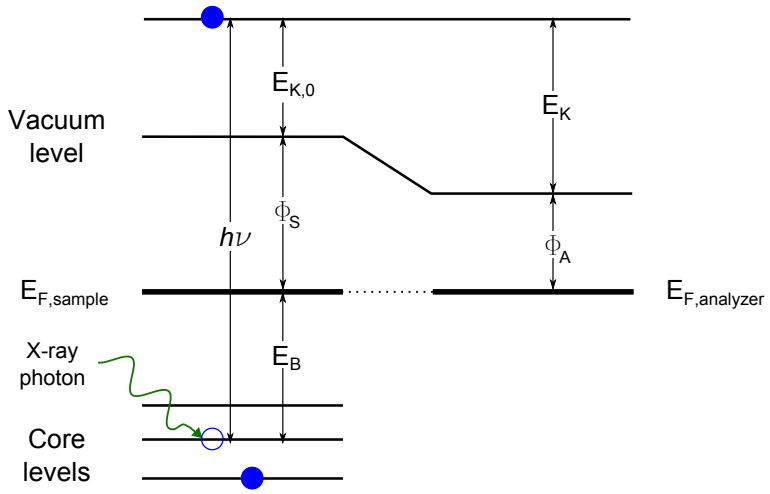

Figure 2.2 | Energy diagram of X-ray photoelectron spectroscopy.

Surface sensitivity

X-ray radiation penetrates several micrometers deep into a sample, exciting electrons from thousands of atomic layers. The excited electrons then interact strongly with electrons and cores of the lattice as they travel through the solid. During each interaction, electrons change their direction and lose part of their energy. The probability of inelastic scattering (inelastic cross-section) depends strongly on the kinetic energy of the electron. Electrons with sufficient energy can excite another electron of a lattice atom from an occupied state to an empty state above the Fermi level. Electrons with lower kinetic energy cause excitations from the valence band only. As the kinetic energy further decreases, the number of unoccupied states available to accommodate both the excited and incoming electron shrinks. Therefore, Pauli repulsion on the low-energy side and the decrease of excitation probability on the high-energy side give rise to a minimal inelastic mean free path (ca 5 Å) at the energy around 100 eV, as summarized as a universal mean free path curve in ref. [66]. XPS takes advantage of the short inelastic mean free path around the minimum to enhance its surface sensitivity. The majority of electrons excited by an X-ray beam suffer inelastic collisions and only electrons emitted from the top few layers have a significant probability of being detected without inelastic losses. As the inelastic mean free path changes along the energy scale, the depth of analysis also varies with the kinetic energy of the electrons. In practical XPS measurements, the surface sensitivity can be enhanced by collecting electrons emitted under a grazing angle rather than normal to the surface. In this case, the probing depth is reduced by a factor of $\cos\alpha$, where α is the emission angle measured from the surface normal. The emission angle is typically adjusted by rotating the sample within the fixed geometry of X-ray source and the electron analyzer.

Spectra interpretation

Photoelectron peaks are described by the core level from which the electron was ejected, typically using the so-called spectroscopist's notation.[4] Transitions are labelled nl_j, where n is the principal quantum number (of integer values 1, 2, 3,…), l is the azimuthal quantum number (taking integer values $0 \ldots n-1$) usually given as a letter (s, p, d, f, …). As a result of spin-orbit coupling, peaks with $l > 0$ (p, d, f,…) are usually split in two. The subscript j identifying these doublets takes values of $|l \pm 1/2|$

and the relative intensities are expressed by the quantity $2j+1$ given by their relative occupancies. Electrons form the p orbital ($l = 1$) form two peaks ($np_{1/2}$ and $np_{3/2}$), and the ratio of their intensities is 1:2. For electrons from d orbital (peaks $nd_{3/2}$ and $nd_{5/2}$), the ratio is 2:3. After photoemission, the ionized atom relaxes by filling the core hole with another electron from a higher level. The energy can be released as an X-ray photon (X-ray fluorescence),[4] however, for lighter elements, emission of Auger electron is much more probable.[67] During the Auger process, the excess energy gained by the internal transition (filling a core hole) is given to a third electron, which is then emitted to the vacuum. The kinetic energy of the Auger electron does not depend on the primary X-ray radiation and is given by the energy difference of the internal transition and the binding energy of the emitted electron. An Auger process thus involves three electrons, which all need to be included to identify the transition. In the XPS spectra, the so-called X-ray notation is used to separate Auger peaks from photoelectron lines. The principle quantum numbers are given by capital letters K, L, M,..., and the subscript is an index of the subshell (includes l and j). Auger transition KL_1L_3 describes a process, where an electron is photo-emitted from the *1s* orbital (K), the hole is filled by an electron from *2s* orbital (L_1), and the energy difference is used in emission of an electron from the $2p_{3/2}$ orbital (L_3), which is detected.

With non-monochromatic sources, X-ray satellite peaks are often observed due to higher-energy excitation as well as X-ray ghost lines due to the emission of X-rays from impurities at the anode, *e.g.*, cross-contamination in dual-anode sources.

Chemical sensitivity

A valuable feature of XPS is its ability to distinguish different chemical bonding configurations in addition to element identification. The number of valence electrons of the atom depends on how many of these electrons are used to make a chemical bond. In oxide lattices, *e.g.*, the metal atom has lost some of the valence electrons in favor of the more electronegative oxygen. The core level electrons are then ejected with slightly higher binding energy due to the additional attraction of the metal atom in an oxidized state. Conversely, if the atom finds itself in a reduced state, extraction of the core electrons will cost less energy. Thus, the binding energy of the core levels responds to the chemical environment and allows to identify the chemical state of

the present atoms. The chemical shift varies among elements from a fraction of to several eV.[4]

Technical aspects of XPS

In laboratory sources, the X-ray radiation is generated from an anode bombarded with high-energy electrons. The anode needs to be water-cooled to avoid overheating, which could cause evaporation and melting. An example of a twin anode X-ray source is shown in Fig. 2.6 (section 2.2.1). The use of two anodes with different photon energies within the same source allows to differentiate between photoelectron transitions and Auger peaks and facilitates element identification. Unlike photoelectron peaks, the Auger peaks do not move on the kinetic energy scale when a different excitation energy is used. Alternative X-ray sources are synchrotron facilities, where the X-rays are generated by deflecting an electron beam along a curved trajectory with bending magnets and along an oscillatory trajectory with undulators. X-ray emission occurs at each deflection event of the electron beam. X-ray radiation from a synchrotron is more intense than that from a laboratory source by many orders of magnitude, and its wavelength can be continuously varied.

A hemispherical analyzer is typically used to measure the energy of emitted electrons in XPS with high resolution.[4] It consists of two concentric hemispheres with a gap between them. Electrons enter the gap tangentially and follow a circular trajectory due to the potential difference applied between the two hemispheres. However, only a fraction of electrons within a relatively small kinetic energy range (pass energy) have the right trajectory to enter a detector of the opposite side of the gap. To enable high energy-resolution, electrons are retarded to lower kinetic energy by a transfer lens before entering the hemispherical analyzer. In general, higher energy resolution is achieved with lower pass energy and a larger diameter of the hemisphere. After passing the hemispherical analyzer, individual electrons are multiplied before they are counted in the detector. Channel electron multipliers (channeltrons) are commonly used to enhance the signal.

XPS under near-ambient conditions

The short inelastic mean free path of electrons due to their strong interaction with matter usually restricts the use of XPS to ultrahigh vacuum. However, considerable

efforts have been made to extend the chemical analysis by XPS into more realistic conditions where a solid sample is in the presence of gases and liquids.[68,69] The instruments are usually based on minimizing the travel distance of emitted electrons in a high-pressure environment. This can be achieved by collecting the electrons close to the sample at a distance smaller than the mean free path in the gas environment. Ref. [70] describes a differentially pumped lens system of the analyzer with electrostatic focusing of the electrons to increase the throughput. An alternative approach to differential pumping is to study the surface of a liquid in a μm-sized jet stream.[71] The technique also allows to study the solid-liquid interface with the limitation that the investigated sample has to be in the form of nanoparticles contained in the stream.[33] Another possibility is the use of single-layer graphene as a photoelectron-transparent barrier, as demonstrated in ref. [72]. Here, copper nanoparticles supported on a graphene membrane were exposed to high pressure of gas on one side and investigated by XPS, by collecting photoelectrons on the other (vacuum) side of the membrane.

2.1.3 Low-energy electron diffraction

Low-energy electron diffraction is a technique for determination of surface structure in reciprocal space. It is based on a spatial collection of electrons elastically scattered by the surface of a single crystal. The de Broglie wavelength λ associated with an electron of energy E is

$$\lambda = \frac{h}{\sqrt{2mE}} \approx \sqrt{\frac{150}{E(\mathrm{eV})}} \left[\text{Å}\right] , \tag{2.8}$$

where h=6.63 $\times$ 10^{-34} $\mathrm{m^2\,kg\,s^{-1}}$ is the Planck constant. For the typical energies in LEED (30-200 eV) the wavelength of electrons is 1-2 Å, of the order or smaller than interatomic distances.[5] LEED is a surface-sensitive technique, due to very short inelastic mean free path of electrons in this energy range. Elastic scattering, therefore, occurs mainly in the topmost layers of the crystal. Inelastically scattered electrons from deeper layers are instrumentally suppressed as discussed in the following.

A crystal lattice represents an ordered, periodic array of scattering centers. Electrons scatter at individual surface atoms and interfere with each other, forming a diffraction pattern. In case of diffraction on the surface, the Laue diffraction condi-

tion relating the diffraction pattern to the reciprocal lattice is[5]

$$\Delta\mathbf{k}^{\parallel} = \mathbf{G}_{\mathbf{hk}}\,, \tag{2.9}$$

where $\Delta\mathbf{k}^{\parallel}$ is the scattering vector component parallel to the surface and $\mathbf{G}_{\mathbf{hk}}$ is a vector of surface reciprocal lattice. Beams that fulfill the condition 2.9 interfere constructively and are projected as bright spots on a fluorescent screen. A typical experimental LEED setup[73] consists of a hemispherical screen to observe the diffraction pattern, an electron gun and a sample placed in the center of curvature of the hemispherical screen. The electron gun is placed behind the fluorescent screen and aligned towards the sample through an opening in the screen.

Electrons are emitted from a cathode at negative potential and accelerated towards the sample on ground. A set of grids (usually two to four) is located in front of the fluorescent screen on the sample side. The first screen is on ground potential to ensure that scattering on the sample is not affected by an electric field. The second and the third grids (suppressor) are both on negative potential close to that of the cathode, used to prevent inelastically-scattered electrons from reaching the fluorescent screen. Electrons which lost part of their energy during (inelastic) scattering are repelled and do not contribute to the diffraction pattern. A pair of suppressor grids is used instead of a single grid to increase the homogeneity of electric field. Greater deviation of the suppressor potential from the cathode potential leads to brighter diffraction pattern but also to brighter background due to inelastically scattered electrons. The last grid is on ground potential again in order to shield the rest of the grids from the high electric field of the fluorescent screen (typically +5 kV), where the electrons retarded by the suppressor are reaccelerated to induce fluorescence. In the reverse-view configuration, the diffraction pattern on the fluorescent screen is then observed, or monitored with a camera, from the side of the electron gun.

Qualitatively, a sharp LEED pattern is an indication of a well-ordered surface without structural imperfections of crystallographic defects. The position of the diffraction spots bears the information about the symmetry of the surface, surface reconstruction and geometry of adsorbate superstructures. LEED can also be used quantitatively (LEED *IV*), to confirm proposed structural models. Here, the intensities of individual diffraction spots are recorded as a function of energy. The experimental *I*-*V* curves are then compared to the calculated curves of the proposed surface

model and the agreement between the experiment, and the prediction is evaluated.[5]

2.1.4 Low-energy ion scattering

Low-energy ion scattering (LEIS) is a surface analysis method providing elemental composition of the outermost atomic layer. Ions (usually inert gases He^+, Ne^+ or Ar^+) emitted from an ion source are accelerated to energies of typically from 100 eV to a few keV[74] and scatter upon collision with surface atoms of the investigated sample. The energy distribution of scattered ions is then analyzed, *e.g.*, using a hemispherical analyzer, similar as for analysis of photoelectrons in XPS (section 2.1.2). The scattering process can be described as an elastic binary collision between incident ion of kinetic energy E_0 and mass m_1 with a surface atom of mass m_2. Applying the conservation laws of energy and momentum, the kinetic energy E_1 of the scattered ion can be expressed as[74]

$$E_1 = E_0 \left[\frac{\cos\theta \pm (q^2 - \sin^2\theta)^{1/2}}{1+q} \right]^2 , \tag{2.10}$$

where $q = m_2/m_1$ and θ is the scattering angle, *i.e.*, the deviation of the incident ion from the straight trajectory. The energy of the scattered ions varies with different angles. In practice, the scattering angle is fixed by the relative orientation of the ion source and the analyzer. The values of E_0, m_1, and θ are known, and E_1 is measured in the experiment. Equation 2.10 can then be solved for m_2 corresponding to each E_1 detected in the spectrum, thus identifying the masses of atoms at the surface.

The mass resolution depends on the primary ion and is not constant across the range of elements. With He^+ ions (mass 4) for example, oxygen (mass 16) and fluorine (mass 19) can be easily distinguished,[75] while the peaks of heavier iron (mass 56) and cobalt (mass 59) are much closer and would likely overlap. The best resolution is achieved when the mass of the primary ion is chosen as close as possible to the mass of the surface atom.

The main advantage of LEIS is its extreme surface sensitivity. The reason for the sensitivity is high neutralization probability of ions penetrating into deeper layers. After the primary ion is neutralized, it can no longer be detected by the analyzer. On materials with relatively open surface structure, *e.g.*, some oxides, the technique may not be strictly sensitive to the topmost layer as observed in ref. [76]

The kinetic energy of the incident ion can also be dissipated in a series of collisions giving sufficient energy to an atom near the surface to be ejected (sputtered) into the vacuum. Besides sputtering ion bombardment leads to intermixing of atoms and loss of the ultimate surface sensitivity. In the experiment, beam damage should be reduced by minimizing the ion beam current and the exposure time required for acquisition of the spectra.

2.1.5 Preparation of oxide single crystals

In UHV, single-crystalline samples are usually prepared by cycles of sputtering with ions of inert gas and high-temperature annealing. While sputtering removes impurities from the surface by removing layers of the crystal, it introduces a significant disorder and intermixing. The sputter-induced damage is typically healed by high-temperature annealing, where the mobility of atoms is increased, and the surface is allowed to recover its equilibrium crystallinity. The sputter yield (i.e., the probability of removing an atom by incident ion) depends on the sputtering angle and varies with the mass of the surface atom. On compound surfaces, preferential sputtering of one element over the other typically occurs. On oxide surfaces, oxygen is sputtered with higher efficiency than the metal. As ultrahigh vacuum by its nature is a reducing environment, an oxygen-deficient composition can often be found even after UHV annealing. While a certain degree of reduction may be beneficial (*e.g.*, providing conductivity due to O-vacancies on TiO_2),[2] an overly reduced surface leads to changes of the surface reconstruction,[13,22] or even changes of the bulk structure.[77] To compensate for prefferential sputtering, oxide crystals can be annealed in background pressure of oxygen instead of UHV. At increased oxygen chemical potential, the thermodynamically-preferred stoichiometric surface can be achieved.[2] On ternary oxides, *e.g.*, $SrTiO_3$, also the metal components are sputtered at different yield, and the stoichiometry has to be compensated by evaporation of constituent metals.[76] Alternatively, stoichiometric single-crystalline surfaces can be prepared by cleaving in UHV along defined crystallographic plane.[78,79]

2.2 Experimental setups

2.2.1 Omega chamber

Most of the experiments reported in this thesis were conducted in a chamber based on an Omicron Compact lab UHV system, colloquially called *Omega*. It consists of the main chamber (base pressure 1×10^{-10} mbar), where sample preparation and analysis took place, and a separately-pumped transfer chamber (base pressure 1×10^{-9} mbar). The transfer chamber is also used as a load lock for inserting samples. Within the thesis, the transfer chamber was modified (as described in section 2.2.1) and extended with a small side chamber for dosing ultrapure liquid water on UHV-prepared samples (the apparatus is described in detail in the following chapter 3). The main chamber is pumped with a turbomolecular pump (TPU 240 from Pfeiffer, pumping speed 240 l/s for nitrogen) backed with a dual-stage rotary vane pump (Pfeiffer Duo 5 M, 5 m^3/h). A zeolite trap is mounted between the rotary vane pump and the turbomolecular pump. Additional pumping of the main chamber is provided by an ion pump (VacIon Plus 150 StarCell from Varian, 125 l/s for N_2) operated with a Varian MultiVac controller, and a triple-filament titanium sublimation pump (TSP, ST22 from VG) controlled by a power supply from Omicron. The pressure in the main chamber is measured by a Bayard-Alpert nude ionization gauge (UHV-24 from Varian), operated with a Varian Multi-Gauge controller. The pressure in the roughing line between the rotary pump and the turbomolecular pump is monitored with an analog Pirani gauge (Varian 801). Manipulation with samples in the main chamber is provided with a manipulator (VG) with translational degrees of freedom in three axes (x,y,z) and rotation around the z-axis. The manipulator is equipped with a radiatively-heated molybdenum sample stage (from Omicron) where samples mounted on Omicron-type plates can be inserted. The temperature of samples is measured by a K-type thermocouple spot-welded to the spring clamp of the sample stage. During the thesis project, the sample stage was electrically insulated from the heating filament, and a separate electrical contact was added to the sample. This enables to ground or bias the sample electrically and perform XPS, LEED or LEIS measurement at the desired temperature. In addition, an independent temperature measurement was added using an infrared pyrometer (Impac 140 from Lumasense). A custom-built electronics box allows to read the temperature and control the settings of the pyro-

meter with a PC or to feed the analog output to a power supply for sample heating. Up to eight samples can be stored in a rotatable carousel inside the main chamber. The sample rack on the magnetic rod of the transfer chamber can store another seven samples. A mechanical wobble stick with a perpendicular pincer grip (VG) is used to transfer samples between the manipulator, the magnetic rod of the transfer chamber and the STM. An overview schematic of the chamber is in Fig. 2.3, details of individual parts are given in the following subsections. The transfer chamber is described in detail in separate section below.

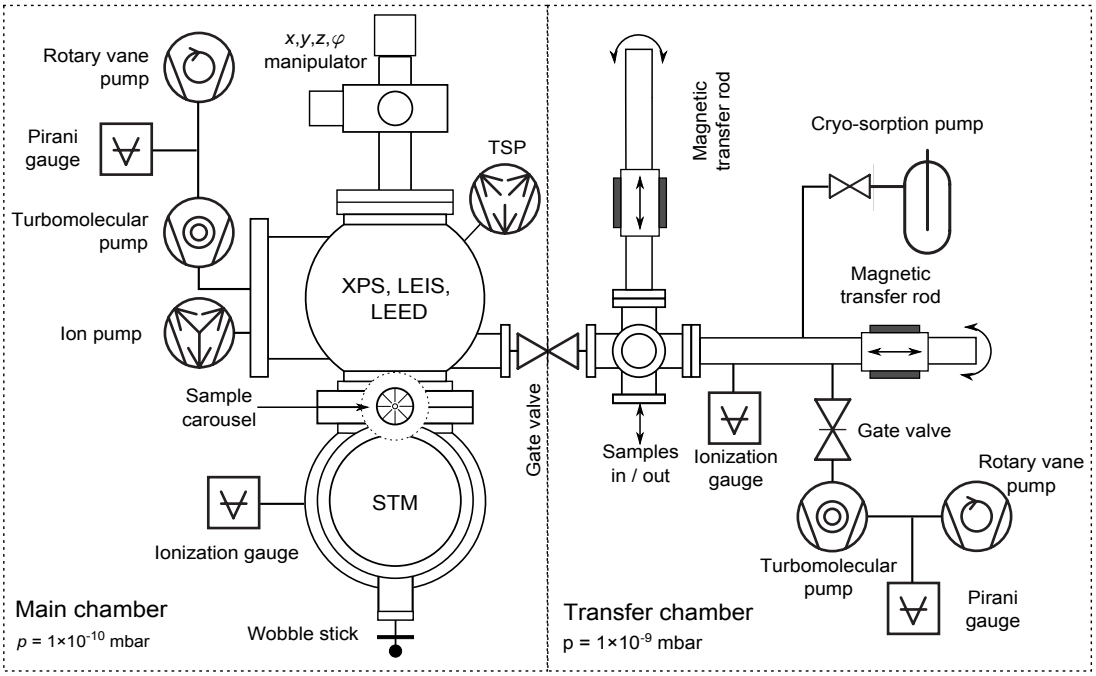

Figure 2.3 | Schematic overview of the UHV chamber *Omega*. (Top-view, individual parts are simplified and not drawn to scale.)

Sample preparation

Samples were usually cleaned by sputtering with Ar^+ ions (1 keV), produced by a SPECS IQE 12/28 ion source. This is a focused-beam source with an electronic control that enables xy scanning of the ion beam. The xy deflection signal is fed into an oscilloscope along with the amplified[80] electric current between the sample and ground induced by sputtering. An image of the sputtered area is reconstructed on the oscilloscope screen, and the ion beam can be aligned on the sample. Focused sputtering minimizes the transport of foreign materials sputtered from the holder onto the

sample as might be the case with broad-beam ion sources. After sputtering, a sample is typically annealed to a high temperature to recover the crystallinity of the surface. Direct current (typically 5-7 A) is passed through a tungsten filament inside of ceramic insulators embedded in the manipulator sample stage. The bottom part of the heater under the filament houses three layers of polished molybdenum plates, which reflect the thermal radiation towards the sample. A programmable direct-current power supply (Delta Elektronika SM 7020, 70 V, 20 A) is used as a current source. The heating power is regulated by a PID controller (Eurotherm 3216). Initially, the sample heater lacked sufficient heating power and was unable to reach temperatures required to obtain a flat surface by annealing (of, *e.g.*, TiO_2). The problem was even more pronounced with bigger, *e.g.*, hat-shaped crystals, where the temperature at the sample base was ca. 620°C (previous maximum) but the surface temperature (measured by IR pyrometer) was lower by more than 100°C. The lack of heating power was partially solved by mounting samples over a hole machined into the sample plate so that the thermal radiation reaches directly the bottom side of the sample. However, using the filament close to its limit gradually led to degradation and eventual failure. During the thesis work, the manipulator heating was upgraded (see Fig. 2.4) by replacing the original (0.2 mm diameter) tungsten filament with a dual (each wire 0.3 mm in diameter) filament. The total length of the tungsten wire is ca. 100 cm. The lower resistance allows to pass higher current through the filament, and the area of the radiation source is more than 4× larger. The Kapton-insulated lead wires between the heater and the feedthrough were doubled (previous rating 5 A, current rating 10 A). After the modification, higher temperatures can be routinely achieved (tested up to 900°C at 7.5 A and 15 V).

A typical cleaning (sputtering and annealing) cycle takes approx. one hour. When working with a new sample or sample that has frequently been taken out of the UHV, a number of cycles are usually required to prepare a clean surface. This presents a time-consuming and repetitive task for the experimentator. During this thesis, sample-cleaning cycles were automatized in order to run unattended, *e.g.*, overnight. Automatic cleaning cycles are directed by a PID controller (Eurotherm 3216), which reads the temperature of the sample and adjusts the heating power accordingly. Via the controller interface, the user defines segments of the desired temperature and duration. Within each of the segments, a relay of the controller can turn on or off the high voltage that accelerates Ar^+ ions towards the sample. A stable pressure of

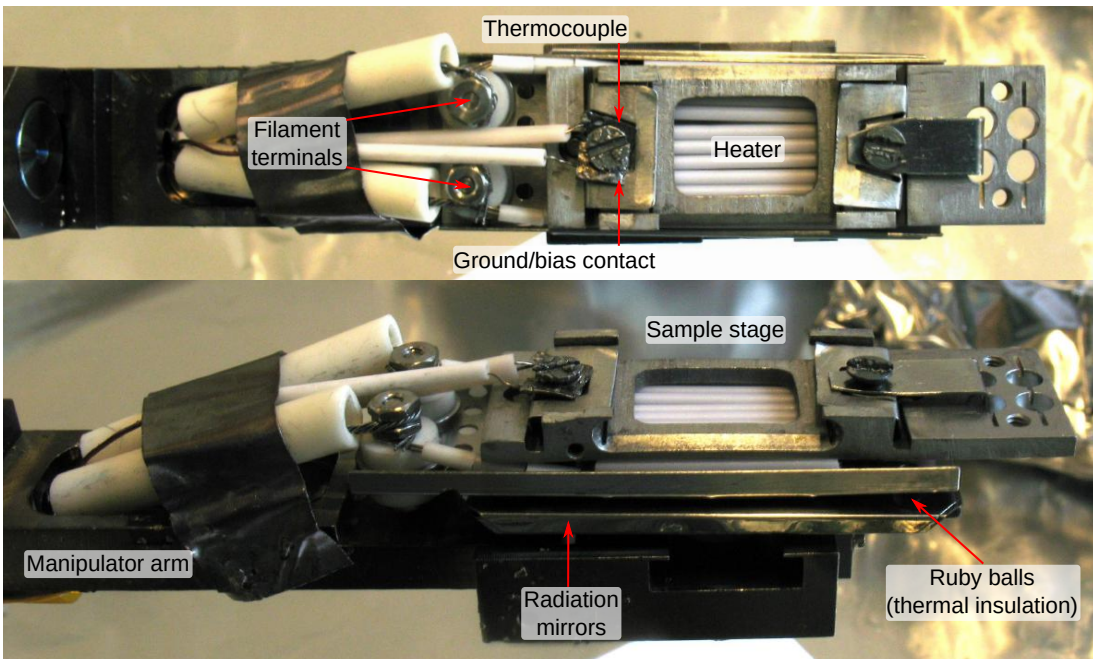

Figure 2.4 | Top and side view of the sample-heating stage of the manipulator. Photos were taken during the heater upgrade.

argon over an extended period of time (*e.g.*, 12 hours) is maintained with a manually and thermomechanically actuated precision leak valve (UDV 146 from Pfeiffer). The valve is manually opened to a higher pressure than required for sputtering. The valve stem contains a bifilar heating coil that is heated according to the voltage applied by a controller (RVG 050 C from Pfeiffer). The controller is connected to the analog output of a pressure gauge in the main chamber and pre-set to the desired pressure (typically 1×10^{-6} mbar). Thermal expansion adjusts the gas flow through the valve and reduces the argon pressure to the required value. The chamber is equipped with four additional variable leak valves (from Varian and Duniway) for dosing a variety of gasses. The purity of these gases and composition of the residual pressure in the main chamber vacuum can be analyzed using a quadrupole mass spectrometer (RGA 100 from SRS). The chamber is also equipped with single-pocket electron-beam evaporator EFM3 from Omicron for evaporation of metals and other materials from rods and crucibles, controlled by an EVC 300 power supply from Focus. The deposition rate is monitored by a heated quartz crystal microbalance (QCM) with a thickness monitor TM 14 from Prevac.

Sample analysis

STM

The chamber is equipped with a UHV STM-1 from Omicron operating at room temperature. The tip is electrically on ground, and the bias voltage is applied to the sample. All images in the thesis were acquired with positive sample bias (*i.e.*, imaging empty states of the sample). A photo of the STM with the tripod tip-scanner and a sample stage with the coarse approach is shown in Fig. 2.5a. STM tips (electrochemically etched from a polycrystalline tungsten wire, 0.5 mm in diameter) are spot-welded to a stainless steel tip holder. The tip holder can be wedged into the STM scanner using a wobble stick or inserted into Omicron-type tip plate (see Fig. 2.5b). The tip can be then transferred in and out of the chamber and replaced or conditioned by head-on sputtering using a custom angled holder. The STM is controlled by RHK electronics recently upgraded to R9 with a custom user interface programmed by Michael Schmid. After preparation, samples should be allowed to cool close to room temperature before insertion into the STM to avoid thermal drift during imaging. As the sample heating stage is thermally insulated from the manipulator, cooling to acceptable temperatures can last more than one hour. In order to reduce the cooling time, a custom cooling stage (designed with Zdeněk Jakub and Jiří Pavelec) made out of oxygen-free copper was mounted into the chamber next to the sample carousel (Fig. 2.55b). Warm samples are inserted with a wobble stick and after ca. 5 minutes they can be transferred into the STM.

XPS

A laboratory dual-anode X-ray source (XR3E2-341 from VG), operated by a high-voltage power supply (SPECS, XRC 1000) was used as an excitation source for XPS. The X-ray source is mounted on the main chamber via a linear bellow retraction mechanism (UHV Design, 50 mm travel) and a custom-modified port-aligner to approach close to the sample and align the direction of the X-ray beam in order to maximize sample illumination. The water-cooled copper anode in the axis of the source is joined with a ca. 3 cm-long silver rod terminated with two oppositely beveled surfaces. Each of the two bevels is coated with a layer of X-ray emissive material, here magnesium and aluminum (see Fig. 2.6a,b). After high positive voltage (typically 12 kV) is applied to the anode, and a current (typically ca. 5 A) is passed through the

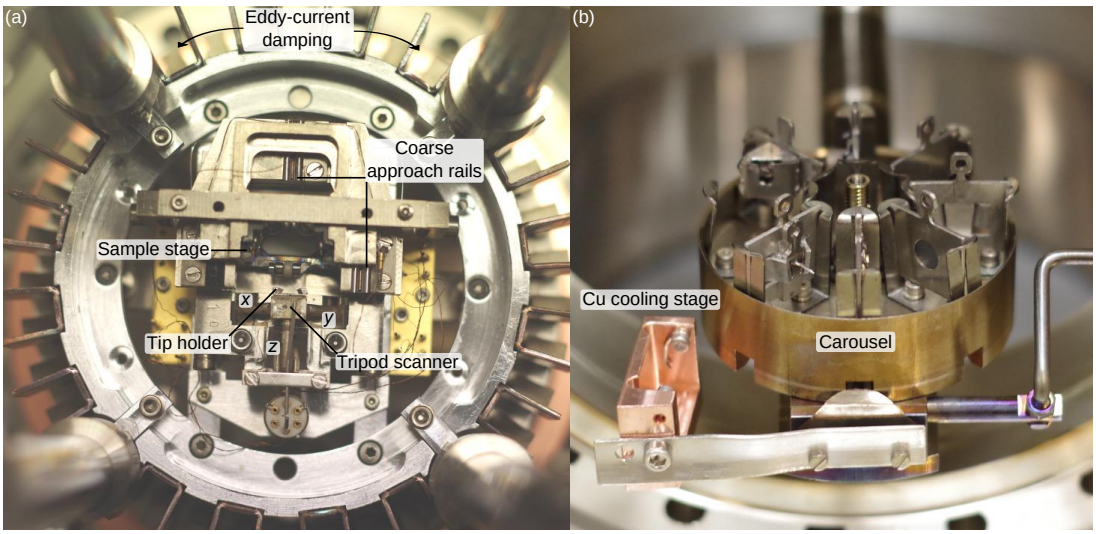

Figure 2.5 | Scanning tunneling microscope Omicron STM-1. (a) Photo of STM during the maintenance of faulty electrical contacts, **(b)** photo of the sample-cooling stage.

filament located near the anode, electrons are emitted from the filament and accelerated towards the coated anode causing emission of X-ray radiation. In practice, the filament current is automatically controlled by the power supply in order to obtain the required emission current (here 16.6 mA), giving the power of 200 W. A thin (ca. 1 μm) aluminum window is mounted at the front of the source (see Fig. 2.6a) to shield the sample from high electric potential of the anode and to protect the sample from impurities, thermally desorbing from the anode heated by electron beam. The window also allows for optional differential pumping of the inner volume of the source through the holes at the back (not included in this system). The emitted X-rays are not monochromatic but contain several characteristic lines and continuous deceleration radiation (Bremsstrahlung). The most intense emission lines for Mg and Al are Mg Kα at 1253.6 eV (FWHM 0.7 eV) and Al Kα at 1486.6 eV (FWHM 0.9 eV),[4] respectively. The aluminum window at the front of the source also protects the sample from irradiation by higher-energy Bremsstrahlung. The ransmission through such a foil has a sharp drop at ca. 1560 eV,[81] and therefore reduces the transmitted intensity of higher-energy radiation (see Fig. 2.6c). Nevertheless, all minor characteristic lines at higher photon energies of both Mg and Al are within the high-transmission part of the curve in Fig. 2.6c. A set of weak satellite peaks at apparently lower binding energy is routinely observed in the XPS spectra using this non-monochromatic source. The strongest satellite lines (ca. 10% of Kα) are usually observed ca. 9 eV lower in

binding energy. The furthest satellite peaks are observed at ca. 49 eV lower binding energy for Mg due to Mg Kβ at 1302.2 eV (intensity 1.7% of Mg Kα) and at ca. 71 eV lower binding energy due to Al Kβ at 1557.5 eV (intensity 2.4% of Al Kα).[82]

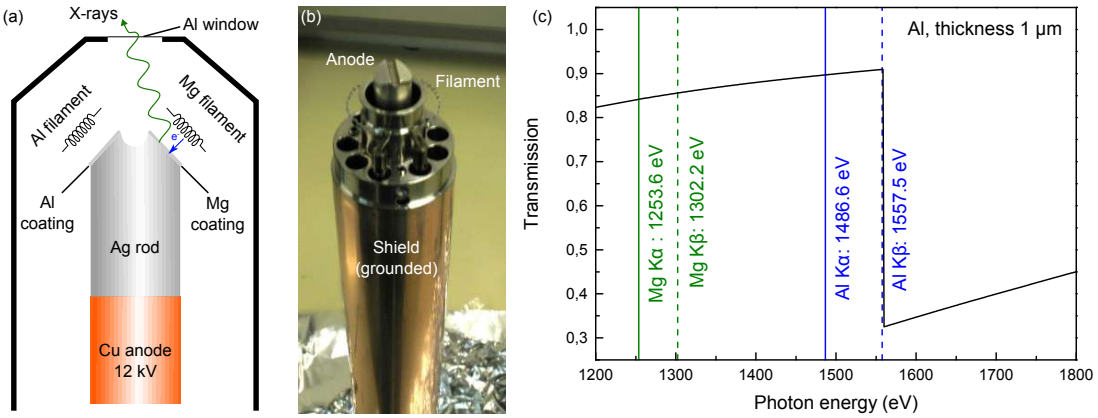

Figure 2.6 | Generation of X-ray radiation for XPS. **(a)** Schematic and **(b)** photograph of the X-ray source VG XR3E2, **(c)** transmission through the thin Al window mounted at the front of the source.

Photoelectrons emitted upon X-ray irradiation are collected with a hemispherical analyzer Phoibos 100 from SPECS (Originally Release 1 analyzer, upgraded to Release 5 in 2004 by addition of the iris mechanism and exchange of lens tubes). The analyzer is equipped with a multichannel detector (MCD-5) with five channel electron multipliers, and it is operated with SPECS HSA 3500 electronics via computer software from SPECS. XPS spectra are usually acquired in normal (0° from the surface normal) or grazing emission (60°–70° from the surface normal). Detailed spectra were typically acquired at 20 eV pass energy for better energy resolution, while higher (60 eV) pass energy was used for most overview scans for better sensitivity. Detailed scans of low-level impurities, such as carbon were often taken at 40 eV pass energy as a compromise between sensitivity and resolution. All XPS measurements within the thesis used the Small Area lens mode, the largest circular entrance slit (6 mm in diameter) and the largest exit slit (6×20 mm).

The analyzer was calibrated in several steps. First, the work function of the analyzer was adjusted so that the Fermi edge of Pt corresponds to zero binding energy. The gain and offset of the energy scale was calibrated using a combined sample with Au and Cu polycrystalline foils mounted on the same plate and placed in the focal spot of the analyzer so that both Au and Cu are detected at the same time. The foils were oriented such that the border between Cu and Au is perpendicular to the en-

trance slit of the analyzer. As the strongest transitions of these elements are relatively distant in binding energy (Cu $2p_{3/2}$ at 933.6 eV and Au $4f_{7/2}$ at 84.0 eV), measuring their positions is suitable for calibration of the energy scale. Independence of peak position on pass energy was calibrated taking advantage of the high-intensity Ag $3d_{5/2}$ 368.3 eV transition of a sputtered silver foil. The focal plane of the analyzer was found by measuring the interface between Ag and Cu foils in different vertical planes and searching for the plane with the steepest slope (sharpest interface).

In early experiments, we were unable to obtain completely clean XPS spectra in the C*1s* region even on a freshly prepared sample. This was attributed to insufficiently clean vacuum in the chamber or contamination of the sputter gas. However, later we found that the residual C*1s* XPS signal does not shift on the energy scale in response to the voltage applied to the sample, unlike the rest of the spectrum. This artificial carbon signal, therefore, does not originate from the sample. We hypothesize that a small fraction of the X-ray radiation is scattered towards the lower parts of the analyzer. As the analyzer is coated with carbon, photoelectrons with a kinetic energy corresponding to the C*1s* transition w.r.t ground are emitted and detected as a part of the measured spectrum. After this finding, we always biased the sample with a nine-volt battery (+9.54 V) during the acquisition of the C*1s* detailed spectrum. Fig. 2.7 shows a C*1s* spectrum of a Fe_3O_4(001) sample, acquired on an electrically grounded sample (blue curve) and the same sample with a bias voltage applied (green curve). As apparent from Fig. 2.7, the artificial carbon peak (from the analyzer) is at the binding energy of so-called adventitious carbon (284 eV).

A nine-volt battery connected to the sample is, however, a somewhat vulnerable setup. If the battery was accidentally shorted, *e.g.*, during the sample transfer, a relatively high current would pass through the grounding wire. Apart from possible damage to the wiring, the voltage of such a battery would drop to an ill-defined value, leading to irreproducible shifts in the spectra. For practical reasons, the nine-volt battery was later replaced with a DC power supply with output voltage set to 9.5 V for easy comparison and with low current-limit set slightly above zero. In case of an accidental short circuit, the voltage immediately drops to zero. The shift in the XPS spectrum can therefore only be either 9.5 eV or 0 eV. For convenience, another strong peak (*e.g.*, Ti*2p* on TiO_2) was acquired both with and without the bias voltage, and the difference between those two peaks was used for correcting the C*1s* spectrum on the binding-energy scale.

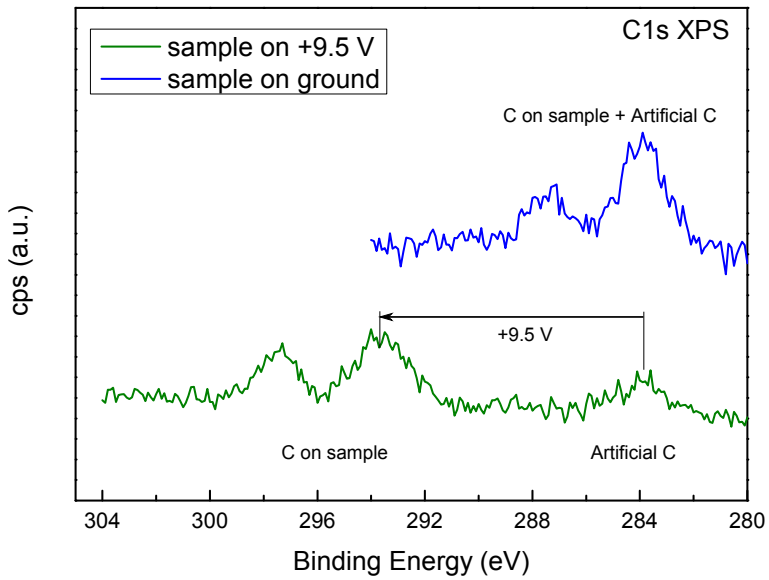

Figure 2.7 | Artificial carbon signal from the analyzer revealed by biasing the sample. C *1s* XPS spectra of $Fe_3O_4(001)$ sample, measured with electrically grounded sample (blue curve) and sample biased by 9.5 V (green curve).

LEED

The chamber is equipped with rear-view LEED optics (SPECTALEED from Omicron) with a LaB_6 filament of the electron source. The control unit (NGL 10), which operates the LEED has an analog (0-10 V) input to control the energy of the electron beam. A three-pin DIN socket on the control unit also supplies 10 V reference output voltage. A simple remote energy control was built, which consists of a ten-turn potentiometer to reduce the reference voltage to the required input value. The remote control allows the user to change the beam energy while watching the LEED screen. Also, a permanently attached monochrome CMOS camera (DMK 33GX174e from The Imaging Source) was mounted in front of the LEED screen flange and placed inside a dark box (designed with Martin Leichtfried). This simplifies the acquisition of LEED data without external light disturbances. In a typical LEED measurement, a dark frame (image at zero screen voltage) and a flat field (image of a polycrystalline sample holder at the same beam energies as LEED images of the sample) were acquired and used for correcting the LEED images for inhomogeneous illumination, screen and camera artifacts. The analog input of the LEED control unit could be easily used for automation of LEED data acquisition. This can be realized with a basic acquisition card with analog voltage output (*e.g.*, NI USB 6008 from National

Instruments), controlled with a LabVIEW program. The user would set an array of required energies, and the program would sequentially adjust the output voltage and synchronize with camera recording. The dark & flat correction could be implemented in the program. This automation would be beneficial when recording a larger set of data (*e.g.*, frames with small energy steps) or when comparing different sample preparations at the same set of beam energies.

LEIS

In LEIS measurements, He^+ ions were generated using the same SPECS IQE 12/28 ion source as for Ar^+ sputtering. He^+ ions were typically accelerated to an energy of 1225 eV for direct comparability with older experiments. A pressure of He measured in the main chamber was 5×10^{-8} mbar. The ionization efficiency of He is ca. 6.25× lower than that of nitrogen,[53] thus the actual pressure of He was higher. The sample current induced by incident He^+ beam was typically 10-20 nA. Similar as in sputtering, the amplified sample current was fed to the oscilloscope to optimize the position of the ion beam. Typically, the sample would be placed in a focal point of the analyzer known from XPS, assuming that the focal point for ions does not differ significantly. The ion beam would be then rastered and deflected to obtain an image of the sample on the oscilloscope. The scanned area was then adjusted close to the sample boundaries to minimize possible beam damage but to avoid the signal from foreign elements of the sample plate. The geometry of the chamber yields a scattering angle of 137° between the forward direction of the ion beam and the analyzer.

The same hemispherical analyzer (Phoibos 100) was used to measure the kinetic energy of scattered ion as for photoemitted electrons in XPS. The analyzer polarity was automatically switched via the operating software. Ions were retarded to a pass energy of 110 eV and the largest (6×20 mm) analyzer entrance slit was used.

Transfer system

The transfer chamber (see Fig. 2.3) was previously used mainly as a load lock for inserting samples. It is separated from the main UHV chamber by a manually actuated gate valve (VAT) and separately pumped with a turbomolecular pump (Varian V250, 250 l/s for N_2) backed with a rotary vane pump (Pfeiffer Duo 5 M) via a zeolite trap. The pressure in the transfer chamber is measured with an ionization gauge

(Granville-Phillips, Series 355 Micro-Ion) operated by an IGC100 controller from SRS. Samples are transported into the main chamber with a sample rack mounted on a magnetically-coupled transfer rod (MT-12 from MDC). For loading samples into the chamber, the whole transfer chamber was originally vented with N_2, fed into the exhaust port of the turbomolecular pump. After venting to atmospheric pressure, a flange was opened to air, and a sample was inserted. After closing the flange, the transfer chamber was first evacuated with a rotary vane pump, and afterwards, the turbomolecular pump was started. The whole process required several hours, and a bakeout of the transfer chamber was usually necessary before the sample could be transferred into the main chamber. Both processes, venting through the turbomolecular pump and roughing with the oil-containing mechanical pump, were likely to contaminate the sample inside the transfer chamber. In order to couple an electrochemical cell or the water drop chamber (chapter 3) to the transfer chamber, a clean and fast transfer of samples was essential. The following paragraphs describe the modifications of the transfer system performed within the thesis.

Venting and pumping procedure

A venting valve (DN16CF, from VAT) was added directly to the transfer chamber. The turbomolecular pump was separated from the transfer chamber by a gate valve (DN40CF, VAT). Additionally, an LN_2-cooled cryo-sorption pump (Ultek, Perkin Elmer) was mounted to the transfer chamber via all-metal angle valve (DN40CF, VAT). This modification allows venting the transfer chamber while the turbomolecular pump is still running behind the gate valve. After venting, the transfer chamber is first evacuated with the cryo-sorption pump, reaching the order 10^{-3} mbar in a few minutes. Cryogenic sorption is a highly-efficient and clean way of rough pumping. The residual gas after pumping is composed mainly of low-boiling point gases such as He and Ne (5 ppm, 18 ppm in air, respectively).[83] The evacuated transfer chamber is then opened to the turbomolecular pump running at full speed (56000 rpm) and quickly reaches the low 10^{-6} mbar range. Provided a high-purity venting gas is used, the whole sample transfer can be performed within five minutes.

Pure argon distribution

Venting the transfer chamber with a high-purity gas proved to be a requisite for clean sample transfer. Fig. 2.8 shows a schematic of the transfer chamber including the distribution system of pure argon built within the thesis.

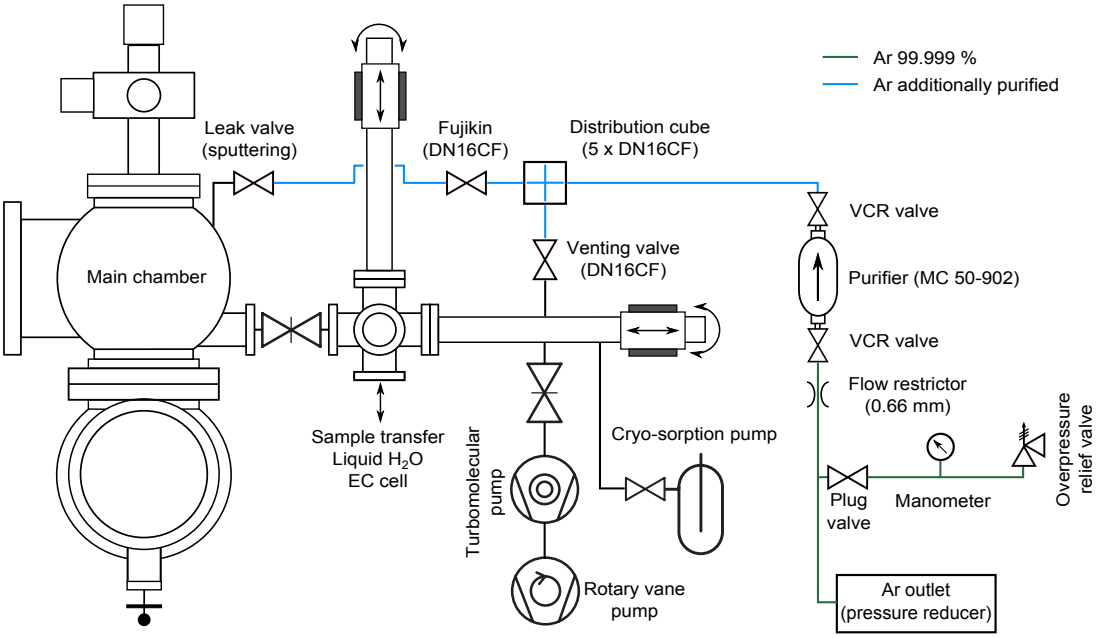

Figure 2.8 | Schematic of the transfer system with pure Ar distribution.

Argon is distributed from a gas bottle (99.999% purity from Air Liquide) in a storage room to a laboratory pressure-reducer outlet via metal tubing. From here, a gas line is connected directly to the chamber using a stainless steel (316 L) tube (1/4" outer diameter) and connectors from Swagelok. Before entering the venting valve to the transfer chamber, argon passes through an in-line sorption filter (MC50-902 FV from SAES) including a particle filter (0.003 μm). According to the manufacturer specifications, the nominal flow of the purifier is 1.5 standard liters/min for optimum performance, and a maximum flow of 10 slpm should not be exceeded. In order to limit the flow through the purifier, a flow restrictor (0.66 mm diameter, VCR from Swagelok) was mounted at the entrance of the purifier. The flow is then controlled by the pressure at the inlet, which in turn is regulated with an adjustable overpressure relief valve (D7 Inox from NGI) and monitored on a manometer (Swagelok). At the same time, the overpressure valve serves as a safety feature to avoid internal pressure on parts of the transfer chamber such as valves, viewports, and bellows. The diameter of the flow restrictor was chosen so that the flow can never exceed the maximum

specified value while it still allows for relatively fast venting of the transfer chamber. The relief pressure of the overpressure valve is adjustable up to 1.7 bar. Although only a slight overpressure (ca. 1.05 bar) is typically used during the venting, the restrictor keeps the flow rate below the specified limit also at the maximum overpressure. Flow rates of both these cases are summarized in Tab. 2.1. All values are calculated for the initial pressure difference when the transfer chamber is still evacuated (0 bar). During the venting, the pressure difference and the flow rate will both decrease.

Inlet pressure	Outlet pressure	Flow (0.66 mm)	Flow (0.432 mm)	Flow (0.254 mm)
1.05 bar	0 bar	3.3 slpm	1.5 slpm	0.5 slpm
1.7 bar	0 bar	5.4 slpm	2.3 slpm	0.8 slpm

Table 2.1 | Flow rates through orifices of different diameters. The rates were calculated using the Gas Flow Calculator[84] for argon gas (molecular weight 39.948) at 21°C.

Other components of the gas line, such as the slowly-opened venting valve, additionally limit the gas flow. As venting of the transfer chamber with the current orifice (0.66 mm) is still relatively fast (a few minutes), further reducing the orifice diameter may be considered. By replacing the flow restrictor with a smaller available size (0.432 mm or 0.254 mm), the specified nominal flow rate of the purifier would be achieved (see Tab. 2.1). All connections on the purified side (light-blue in Fig. 2.8) are UHV-compatible (VCR or CF flanges). From the outlet of the purifier, argon enters a custom-made distribution cube with five DNCF16 flanges interconnected with drilled holes (4 mm internal diameter to match the size of the gas tubes). Only three of the flanges are currently in use; the inlet from the purifier, the outlet to the venting valve and a separate line, which is directly connected to the leak valve mounted on the ion source of the main chamber. This enables to use the purified argon also for sputtering and allows to check the purity by analyzing the gas with the mass spectrometer in the main chamber. The remaining two flanges can be used for connecting more parts to ultrapure argon or for filling the distribution system with a different gas. The sputtering line (8 mm outer diameter) is typically filled with a higher pressure of argon (3 bar). The overpressure valve needs to be disabled when pressurizing the line by closing the plug valve next to the manometer (see Fig. 2.8). Before use, the purifier was conditioned to meet specified purity levels using a procedure recommended by the manufacturer. The conditioning consisted of passing argon flow of 0.2 slpm while pumping the outlet with the turbomolecular pump for two hours. The comparison of mass spectra (Fig. 2.9) of argon directly from the gas bottle (purity 99.999%) and addi-

tionally purified argon show a substantial decrease of several impurity components, mainly CO, CO_2, and N_2.

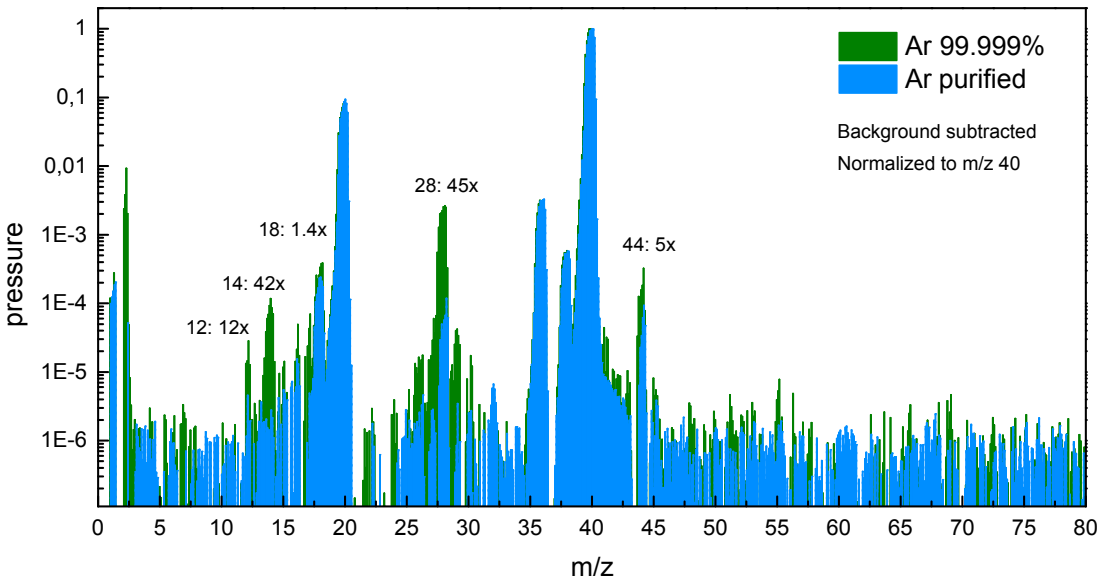

Figure 2.9 | Mass spectra of Ar from the bottle and additionally purified. Both spectra were normalized to m/z 40 (to equalize argon pressures) after background correction (subtracting the mass spectra of residual vacuum before dosing Ar). Numbers at individual peaks are the reduction factors due to the purifier.

Individual modifications of the transfer system were iteratively tested by characterization (mainly XPS, LEED and STM) of the magnetite $Fe_3O_4(001)$ surface, which proved to be a sensitive probe to impurities.[85] Fig. 2.10 shows XPS spectra of $Fe_3O_4(001)$ exposed to atmospheric pressure of venting gas using the original transfer system, where the transfer chamber was vented with N_2 through the turbomolecular pump and roughed with a rotary pump, and compares it with the current setup, where the transfer chamber is vented with purified Ar and roughed with a cryo-sorption pump.

While the original transfer system contaminated samples considerably (red curves in Fig. 2.10), exposure to atmospheric pressure of argon using the current transfer leaves the samples clean (see the overlap of green and black curves). Fig. 2.10 also shows the effect of the liquid H_2O droplet (blue curves) put on the surface of $Fe_3O_4(001)$ sample using a pipette in the vented transfer chamber. While the higher-binding-energy shoulder of the O*1s* peak is a signature of surface hydroxylation, the C*1s* spectrum shows no increase. The transfer system can, therefore, be used in experiments with clean exposure of UHV-prepared samples to liquid H_2O (as in the experiments on $TiO_2(011)$ described in chapter 5). In case of the dirty transfer sys-

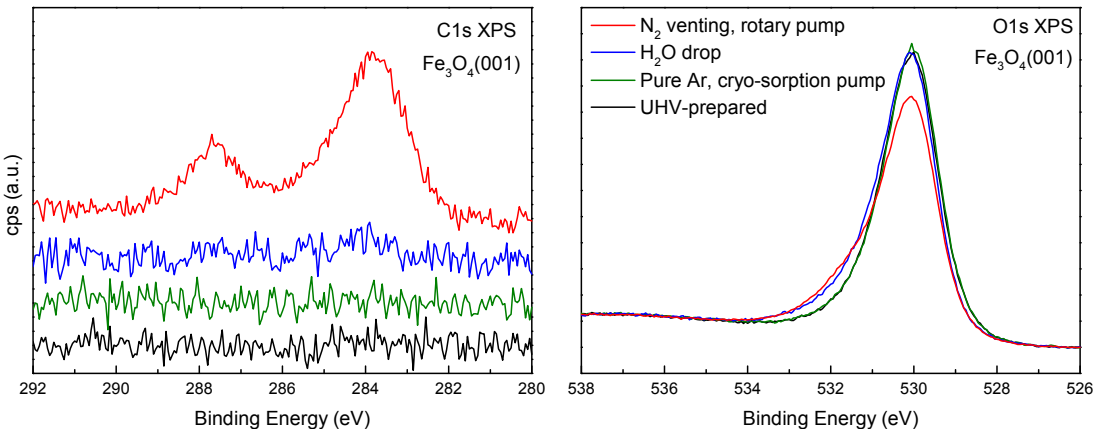

Figure 2.10 | XPS spectra of Fe3O4(001) exposed to atmospheric pressure of venting gas. All spectra shown here were acquired with 20 eV pass energy at normal emission. Individual C *1s* spectra are vertically offset for clarity.

tem, a somewhat similar shoulder of the O *1s* peak was observed (red curve in Fig. 2.10). While this shoulder could be mistakenly attributed to hydroxyl groups due to the residual humidity of the venting gas, it is likely due to adsorption of carboxylic acids (a discussed in chapter 4), which is also evidenced by the peak at 288 eV in the C *1s* spectrum. Later, a dedicated setup for dosing liquid water was developed, which avoids the use of venting gas and further improves the purity of experiments with liquid water (as described in the following chapter 3). It should be noted that the XPS sensitivity in later experiments (*e.g.*, in the spectra in Fig. 3.13 in chapter 3) was higher than here (Fig. 2.10), mainly due to acquisition at grazing emission and higher pass energy (40 eV).

Sample transfer

In addition to transporting samples between the main chamber and the transfer chamber (in vertical position), a perpendicular sample transfer with horizontally-oriented samples was required. In such orientation (facing up or down), samples are inserted into the electrochemical cell and the water drop chamber. A magnetically coupled transfer rod (MLRV203 from VG) was added to the transfer chamber (see Fig. 2.8) and a custom sample carrier (designed with Zdeněk Jakub and Jiří Pavelec) was build. The carrier (Fig. 2.11a) consists of an outer sleeve attached to the end of the transfer rod and a rotatable insert, both made out of stainless steel. The ear of the sample plate is inserted into the slit and locked in place by rotating the outer sleeve

by 90° against the insert (Fig. 2.11b). For easy rotation, the insert and the sleeve are separated by a ball bearing made out of a copper cage and four pairs of stainless-steel balls. The pressing force is provided by five pairs of magnets mounted in repulsion to the rotatable insert and the fixed base of the carrier. The square symmetry of the magnets ensures that the carrier finds itself either in open or locked position. Details about the design and assembly can be found in ref. [86].

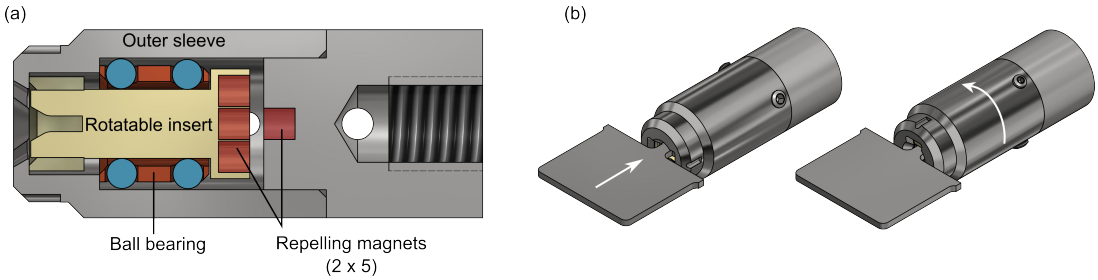

Figure 2.11 | Sample carrier for transfer in horizontal orientation. (a) section view of individual components, **(b)** procedure of inserting and locking a sample plate in the carrier. Adapted and reprinted from ref. [86]

2.2.2 LT-STM chamber

The LT-STM chamber was used in the experiments with low-temperature H_2O adsorption on TiO_2(011), described in chapter 5. The system consists of two adjacent UHV chambers and a load lock. The first chamber is pumped with an ion pump and a TSP to achieve a base pressure of 5×10^{-12} mbar without mechanical pumps. This chamber is used only for analysis with the low-temperature STM (Omicron), which can be operated at 78 K or 6 K (by filling the cryostat with LN_2 or with LHe, respectively). Without cooling, the STM can also be operated at room temperature. The second chamber (base pressure 5×10^{-11} mbar) is used for sample preparation and is equipped with instrumentation for analysis by XPS, AES, LEIS, and LEED. Samples are prepared by Ar^+ sputtering and annealing using electron-beam heating in a separate heating stage. Unlike the system described above (section 2.2.1), the low-temperature STM system allows cooling the sample in the manipulator by LN_2 or LHe or counter-heat to the desired temperature. The second chamber is pumped with an ion pump, TSP, and a turbomolecular pump. Samples are inserted through a load lock using the same sample carrier mechanism as described in above (Fig. 2.11).

Chapter 3

Apparatus for dosing liquid water in ultrahigh vacuum

Part of the experiments reported in the thesis (*e.g.*, liquid H_2O on TiO_2(011), chapter 5) were carried out using a rather simple experimental setup. The sample, prepared and characterized in the main UHV chamber, was transported to the transfer chamber (both described in chapter 2), which was then vented to atmospheric pressure of an inert gas, and liquid water was deposited on the surface using a pipette or a glass syringe. A considerable effort was placed on the purity of the venting and pumping process. Although we markedly reduced the contamination level, we were not able to fully eliminate the adsorption of carboxylic acids present in the air. These were found to readily adsorb and form an ordered overlayer on TiO_2(110), as described in chapter 4. In order to dose liquid H_2O without impurities from the ambient air, we constructed a closed system that allows us to bring a sample in contact with ultrapure liquid water without exposure to air and does not involve backfilling with a venting gas. In this process, a sample is transferred under UHV into a separate, small chamber and placed below a volume of ultrapure water ice, whose vapor pressure is reduced to the UHV range by cooling to cryogenic temperatures. Upon warming, the ice melts and forms a liquid droplet, which is deposited onto the sample. Optionally, gasses can be added in a controlled way to the background.

The design and some of the data included here were reported in ref. [87]. This chapter, however, contains more detailed information about the development, construction, and assembly of the apparatus, and also suggests possible improvements of the current setup.

3.1 Vapor pressure of H_2O

The key physical concept of the apparatus is the temperature-dependent vapor pressure of water. Water does not exist as a liquid at partial pressures below 6 mbar.[88] In an ultrahigh vacuum, water is only stable as a vapor or a solid, depending on its temperature. Liquid water placed in a vacuum would evaporate instantly, and larger volumes would freeze as a result of the sudden heat loss due to evaporation. If not actively cooled, ice would then sublime into the vapor phase.

When liquid water is placed in a closed container, water vapor soon fills the volume above the liquid. Some molecules near the surface of the liquid have sufficient kinetic energy to overcome attractive forces and escape from a liquid into the vapor. At the same time, other molecules are re-entering liquid from the gas phase. A dynamic equilibrium is established when water molecules are leaving the liquid at the same rate as gas molecules re-enter the liquid. On average, the amount of both, liquid and vapor-phase water remains constant. The same kind of dynamic equilibrium is established in case of solid ice in a closed container. Evaporation occurs at all temperatures above 0 K, and the rate increases as the temperature rises. The vapor pressure represents the density of water molecules in the gas phase above liquid water or solid ice. In a gas mixture, *e.g.*, in air, the water vapor pressure is the partial pressure of water vapor in thermodynamic equilibrium with its condensed state (solid or liquid water). Fig. 3.1 shows the temperature dependence of water vapor pressure. The marked values are relevant for the design of the apparatus described in this chapter: at normal melting point (0°C), the vapor pressure is 6 mbar, and below 130 K the vapor pressure is under 1×10^{-10} mbar.

The following sections describe in detail the experimental setup for dosing liquid water, and explain how the vapor pressure of water is controlled in practice.

3.2 Experimental setup

Experiments with liquid water were performed in a custom-built chamber that was attached via a separately-pumped transfer chamber to the existing UHV system (see chapter 2). This so-called water drop chamber and associated parts are described separately below. All custom components were designed together with Jiří Pavelec and Mojmír Komora and produced by Rainer Gärtner and Herbert Schmidt in the

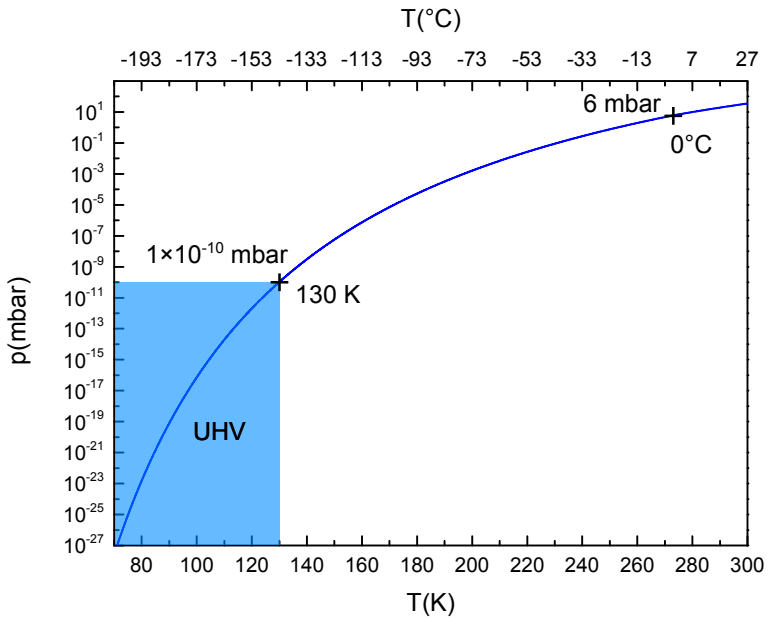

Figure 3.1 | Vapor pressure of H_2O as a function of temperature. The vapor pressure of water cooled under 130 K is below 1×10^{-10} mbar (highlighted blue as UHV range). The data of the curve were generated with online calculator[89] based on a fit to ITS-90 table[90,91].

mechanical workshop at IAP TU Wien.

3.2.1 Water drop chamber

The design of the chamber was directed by two main guidelines: limiting the types of materials exposed to water and minimizing the surface area exposed to water vapor. These requirements reduce the complexity and pump-down time. A hexagonal shape of the drop chamber (Fig. 3.2) was chosen so that the chamber could be mounted directly onto a gate valve (DN40CF, VAT) of the transfer chamber without a connecting part. This geometry reduces the internal volume and surface area, and accommodates up to six DN16CF radial ports. The first version of the chamber was machined out of stainless steel (SAE 304) and used three radial ports. The top port was recessed by 5 mm and used for the so-called cold finger, described in detail in section 3.2.2. The two bottom ports were used as an inlet for H_2O vapor and as an outlet to the cryo-sorption pump, respectively. While the inlet H_2O vapor is guided by a tilted hole to obtain an almost direct line of sight to the cold finger, the pumping hole intersects with the volume of the gate valve to achieve better conductance (flow indicated in Fig. 3.2b). Located on the front face of the chamber is a DN16CF

viewport for observing samples and the cold finger during the transfer and experiment. The drop chamber houses a receptacle for samples mounted on Omicron-type sample plates. The receptacle consist of two symmetric rails mounted to the inner wall of the chamber that guide the sample plate during insertion. A spring-loaded metal sheet keeps the sample plate in place. The rails are machined with a tight fit to the height of the central slit of the chamber to prevent their rotation. Once inserted, the sample rests on a 0.5 mm thin stainless steel wall. A copper rod is pressed to the bottom of the thin wall and allows for sample heating or cooling during the experiment. (Sample heating or cooling was not actively used in most of the experiments described in the thesis.)

Later, a second version of the water drop chamber was produced (shown in Fig. 3.2). The second version corrects for a design flaw of the first version, where the central slit was 5 mm too deep, and a spacer had to be used to position the sample directly under the tip of the cold finger. Moreover, the second chamber was machined out of better stainless steel grade (SAE 316LN ESR from Vacom) providing higher chemical resistance, and it has two additional ports. One is used as optional gas inlet and the other one as a viewport for sample illumination. Both versions have the same geometry of the water vapor inlet and outlet holes.

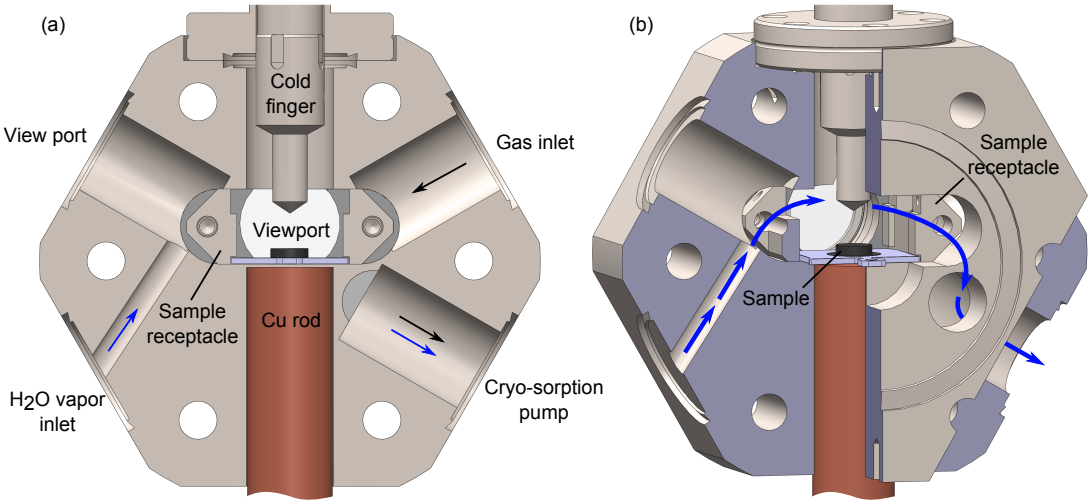

Figure 3.2 | Water drop chamber (2^{nd} design) viewed from the direction of the transfer chamber. (a) section-view with a description of ports, **(b)** perspective partial section-view, blue arrows indicate the diverted flow of H_2O vapor from the supply to the cryo-sorption pump. The DN40CF flange connecting to the gate valve is at the front.

The internal volumes and surface areas of the two version are compared in Tab. 3.1.

The columns ”Chamber volume” and ”Chamber surface area” take in account only the chamber itself, *i.e.*, when covered by blank flanges but excluding the area of the blanks. Other components connected or inserted into the chamber, *e.g.*, the cold finger, sample receiver, valves, viewports, etc., increase the surface area significantly and alter the internal volume. All these surfaces are exposed to water in experiments and are considered in columns ”Total volume” and ”Total surface area”.

	Chamber volume	Total volume	Chamber surface area	Total surface area
1^{st} chamber	0.018 l	0.042 l	57 cm^2	177 cm^2
2^{nd} chamber	0.025 l	0.051 l	81 cm^2	207 cm^2

Table 3.1 | Internal volumes and surface areas of the first and second water drop chamber. Only the chamber itself is taken into account in columns 2 and 4. Other components attached to the chamber are included in columns 3 and 5.

Integration of the water drop chamber with the UHV system

The water drop chamber is attached to the UHV chamber via a transfer chamber (base pressure 1×10^{-9} mbar, separately pumped with a turbomolecular pump). The transfer chamber is separated by gate valves from the drop chamber and the main UHV chamber. In the experiments, the sample is typically prepared in the main chamber by cycles of sputtering and annealing and can be characterized by various techniques (STM, XPS, LEIS, and LEED). Afterwards, the sample is transferred into the drop chamber where exposure to water takes place. The pressures in the main chamber and the transfer chamber are maintained in the UHV range during the whole experiment. A typical pressure in the transfer chamber during the sample transfer under the icicle is in low 10^{-8} mbar range.

Located at the entrance to the transfer chamber is a cryo-panel, made out of an oxygen-free Cu sheet, rolled into a tube and cooled by LN_2. This cryo-panel prevents residual water vapor (and other gases condensable at liquid nitrogen temperature) from entering the transfer chamber. In addition, it improves the pressure in the transfer chamber. The tubular shape (32 mm diameter, 176 mm long) allows passage of the magnetic transfer rod that carries the sample. Fig. 3.3 shows a schematic of the UHV system with the water drop chamber connected.

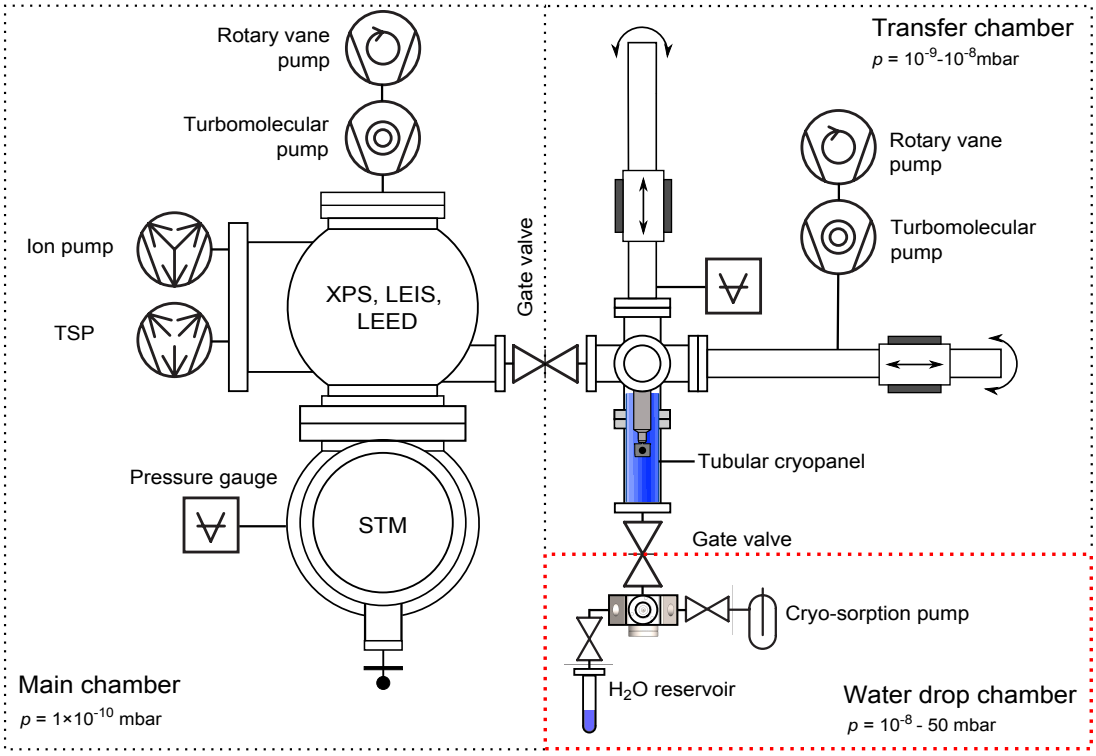

Figure 3.3 | Schematic of the UHV system including setup for dosing liquid H_2O (red, dashed rectangle). Individual parts of the UHV system are simplified and not drawn to scale.

3.2.2 Cold finger

The cold finger (Fig. 3.4) is a small flow-cryostat mounted to the top port of the water drop chamber. Its primary function is to create a localized cold spot. When water vapor is introduced into the chamber, it will freeze on the cold tip while condensation on other surfaces is avoided. The ice at the tip has to be cooled below 130 K to maintain water vapor pressure below 1×10^{-10} mbar (see Fig. 3.1), which is desirable for sample transfer between UHV and the water drop chamber.

Working principle and construction

Individual parts of the cold finger assembly as referred to in the further text are labeled in Fig. 3.4. The coolant (here LN_2) is guided by a stainless steel capillary (inner diameter 0.5 mm) from the inlet at the top all the way down to the tip. At the tip, LN_2 enters a copper heat exchanger pressed onto the inner surface of the tip. It expands and returns through a concentric exhaust tube. At the inlet, there is a particle filter to prevent small (ice) particles from entering the capillary. Circulation of LN_2 is achieved by pumping the exhaust with a roughing pump as well as by the hydrostatic pressure of an LN_2 reservoir on top of the inlet. To localize the cold spot at the tip, the wider part above the tip is counter-heated (typically to 40°C) by pressing a resistively heated copper tube to the inner stainless steel surface. Heat transfer by conduction between cold and warm areas is minimized by separating them by a thin-wall (0.3 mm) stainless steel tube. The thermal conductivity of stainless steel (14 W/m K at 20°C) is notably lower than that of copper (400 W/m K at 20°C). To avoid heat transfer by convection, the inner volume of the cold finger is evacuated with a roughing pump. This enables the tip of the cold finger to be locally cooled to cryogenic temperatures while the upper parts are kept above room temperature. The temperatures of both, the cold and warm parts, are measured with K-type thermocouples mounted on the inner surfaces (thermocouples A, B in Fig. 3.4). Good thermal contact and a rough vacuum seal between the N_2 and the insulation are achieved by pressing the copper parts against the stainless steel surfaces. A defined force is provided by compression springs. At the top side, the exhaust LN_2 is isolated from the rough vacuum by Viton O-rings placed in precision-machined grooves. The specifications of the springs and O-rings are listed in the assembly section 3.2.2. All parts that reach into the UHV were machined out of stainless steel (SAE 304), while

the inner parts are made of stainless steel and copper.

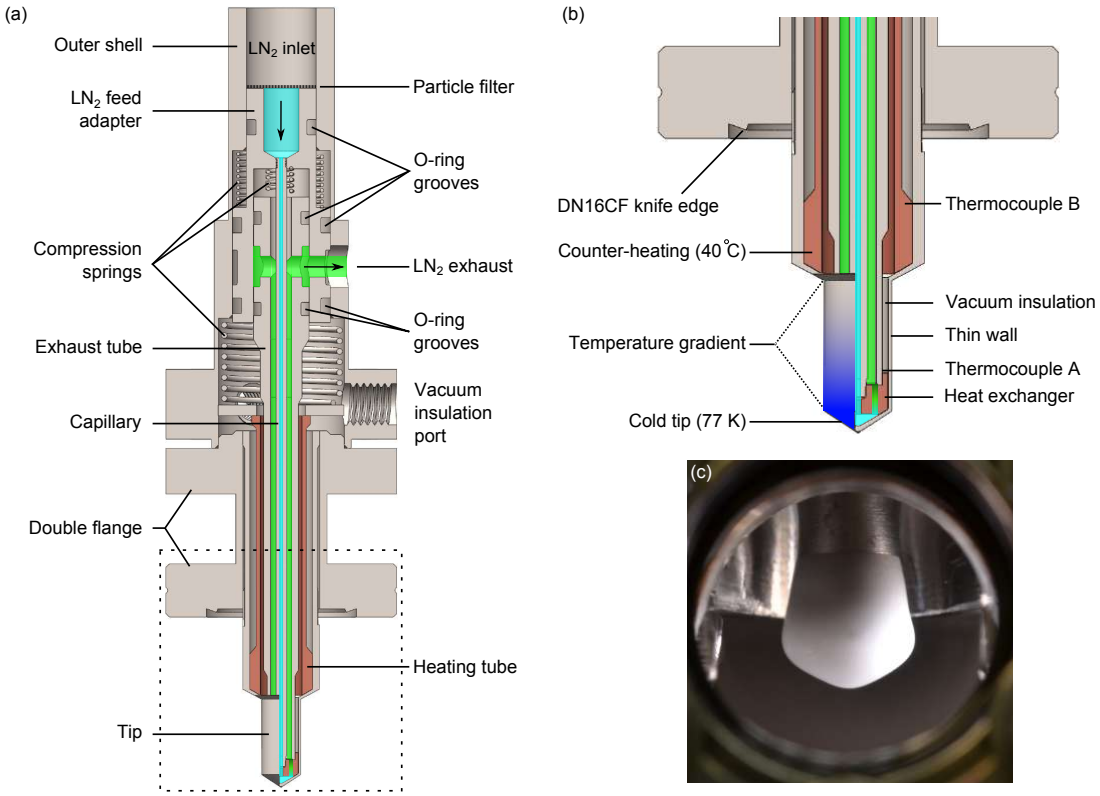

Figure 3.4 | Section-view of the cold finger. The LN_2 flowing from the supply to the cold tip is marked in light blue and the exhaust LN_2 after passing through the heat exchanger is marked in light green. Parts made of copper and stainless steel are indicated in orange and grey, respectively. The section within the dashed rectangle in **(a)** is magnified in **(b)**. The blue shading indicates the temperature gradient between the cold tip and the counter-heated, upper part. The photograph in **(c)** shows that ice forms locally on the lower cold part of the tip.

Cold finger assembly

Prior to assembly, all parts were degreased with several sonication cycles in acetone and isopropanol. The tip and the double flange were then welded and cleaned again. The assembly started with parts that do not reach into UHV and are only exposed to rough vacuum. UHV-incompatible materials such as grease and heat-shrink tubes could be used here. First, Viton O-rings were put to the grooves of the LN_2 feed adapter and the exhaust tube. The O-rings and grooves were lubricated with vacuum grease (Krytox) for better sealing and easier assembly. The O-rings were made of FKM 80, a fluorinated elastomer with low gas permeability and therefore suitable for

vacuum applications. The dimensions of the used O-rings are listed in Tab. 3.2, and their positions are indicated in Fig. 3.5.

O-ring	Item No.	d_i [mm]	d_s [mm]
A	67194130	7.0	1.8
B	67012548	10.8	1.78
C	67194629	5.5	1.5
D	67013235	20.0	1.5

Table 3.2 | Dimensions of the used O-rings. The internal diameter is denoted d_i, and d_s is the diameter of the circular cross-section (thickness). All O-rings were from Dichtomatik and made out of FKM 80. Item numbers are included for easy identification.

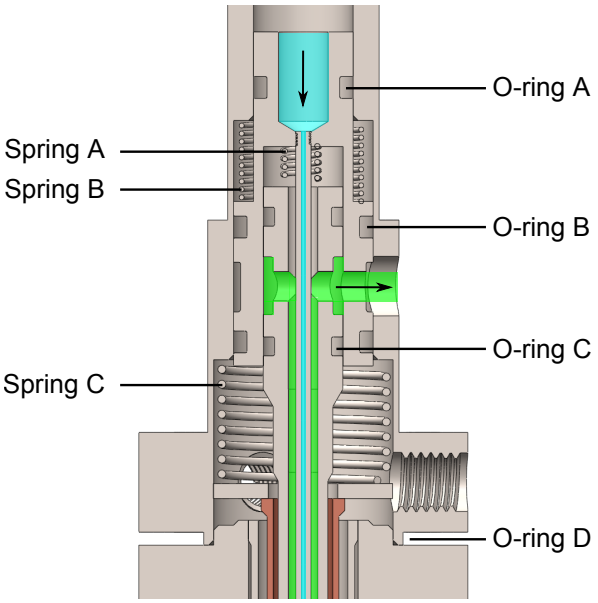

Figure 3.5 | Positions of compression springs and O-rings. Specifications are listed in Tab. 3.2 and Tab. 3.3. There are two O-rings B and C (only one of each is labeled).

The LN_2 feed adapter was then screwed onto the capillary, and the thread was sealed with Teflon tape. Spring A and the exhaust tube were then put on the capillary and pushed into the LN_2 feed adapter (see Fig. 3.6a). Spring B was then put on the outside of the LN_2 feed adapter and the whole assembly was inserted into the outer shell. To keep the internal parts in their working position during the rest of the assembly, the springs were pre-loaded and secured in place with an assembly tool inserted into the exhaust port. The springs used are listed in Tab. 3.3 and their positions are indicated in Fig. 3.5.

The copper heat exchanger (Fig. 3.4b) was machined with an interference fit to the outer diameters of the capillary and the exhaust tube. It was mounted by pressing

Spring	Item No.	L_0 [mm]	R [N/mm]	L [mm]	F [N]
A	36/5/1	8.7	0.43	4.0	2.0
B	56/45/1	26.5	1.41	8.1	25.9
C	57/6/3	63.6	0.36	12.4	18.4

Table 3.3 | Parameters of the compression springs used. L_0 is the natural length of the spring, L is the working (compressed) length, R is the spring stiffness and F is the force applied by the spring. All springs are from Hennlich and are made out of stainless steel (SAE 304). Item numbers are included for easy identification.

the heat exchanger simultaneously against the capillary and the exhaust tube while they were held in their working positions and supported by an assembly tool. As the next step, a K-type thermocouple (Thermocouple A on Fig. 3.4b) was spot-welded to the exhaust tube near the heat exchanger (see magnified inset in Fig. 3.6b). Wires were secured in place with a Teflon tape.

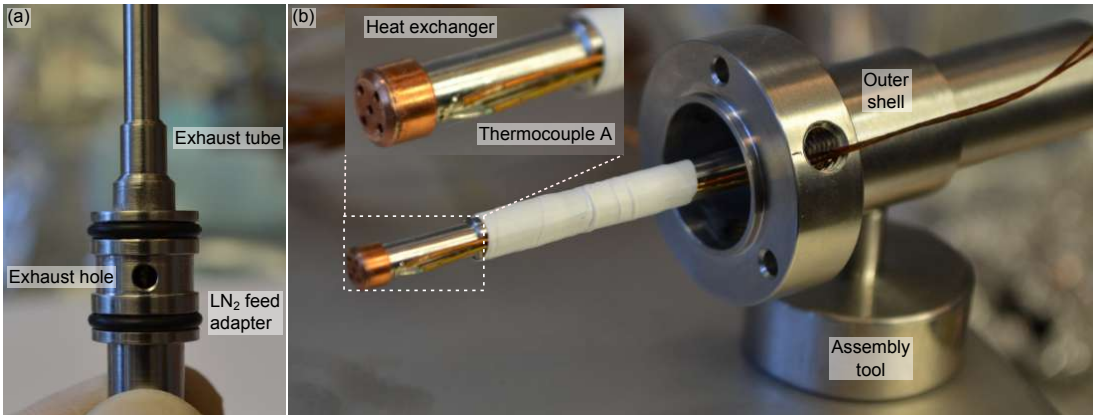

Figure 3.6 | Cold finger assembly. (a) Exhaust tube inserted into the LN_2 feed adapter (both parts with O-rings in place), capillary and spring A are not visible (inside). **(b)** Thermocouple A mounted next to the heat exchanger, assembly resting on the assembly tool mounted to the exhaust port.

Spring C and the washer that transmits the force from spring C to the heating tube were then inserted into the outer shell. The forces applied to the individual components (summarized in Tab. 3.4) can be obtained by vector addition of the forces applied by the springs.

The second K-type thermocouple (Thermocouple B in Fig. 3.4b) was pressed onto the bottom of the heating copper tube, fastened with Teflon tape, and secured with a heating wire wrapped around the tube. For heating, a resistively heated Chromel wire (0.25 mm in diameter, total resistance 40 Ω) was used, coated with heat-resistant electrical insulation (Kapton). The bottom part of the heating tube is widened to guide

$F_{\text{capillary}}$	$F_B - F_A$	23.9 N
$F_{\text{exhaust tube}}$	F_A	2.0 N
$F_{\text{heat exchanger}}$	F_B	23.9 N
$F_{\text{heating tube}}$	F_C	18.4 N

Table 3.4 | Forces applied to the individual components. All forces are applied along the vertical axis of the cold finger. Forces F_A, F_B, and F_C refer to the forces applied by individual springs A, B, and C listed in Tab. 3.3.

the heating tube during insertion into the double flange. Both thermocouple pairs and the heating wires were guided to the outside through a vacuum insulation port (see Fig. 3.4a). All six wires were spot-welded to the pins of a triple-thermocouple DN16KF feedthrough and secured using heat-shrink tubes. Located on the outer shell are three symmetric vacuum insulation ports for better flexibility during mounting on the UHV system. In the current setup, the same port was used for rough pumping and for the electrical wiring. Here, a custom-made M6-DN16KF adapter was sealed with Teflon tape, screwed in and locked against rotation using a counter-nut. The unused pumping ports were blanked with Teflon tape-sealed bolts. Finally, the last O-ring was put in position D (Fig. 3.5), providing a face seal, and the whole assembly was inserted into the tip. The outer shell was secured with three M3 bolts to the double flange, and then the assembly tool could be released. After assembly, the outer surface of the tip (reaching into UHV) was boiled and sonicated in pure hot MilliQ water as the last step before mounting the cold finger to the water drop chamber. The whole setup (see Fig. 3.8) was then mounted to the transfer chamber as indicated in Fig. 3.3.

The second version of the cold finger

In the first version of the cold finger, the tip and the double flange were machined separately and then welded. The weld was done on the rough-vacuum side (see Fig. 3.7a), which may potentially cause a virtual leak on the UHV side. For better pumping of the tight space between the tip and the double flange, four additional pumping grooves were milled to the side of the tip. The angle of the tip apex was chosen to be 118°, as this is the angle of a standard drill. This way, the inner and outer angles of the tip are the same, and the wall thickness is uniform. The second version of the cold finger (Fig. 3.7b) was designed to further improve the first version and have two working setups. The outer weld between the tip and double flange was avoided by

machining the two parts in one piece. It was produced out of better grade stainless steel (SAE 316LN ESR from Vacom). The sharper angle of the tip apex (30°) allows to dose smaller droplets. In addition, the outer surface of the tip reaching into UHV was polished (1000 grit). Also, the inner surface of the tip was polished for better contact with the heat exchanger. By circumventing the welded construction, the surface area exposed to UHV (and H_2O vapor) was reduced from 25.3 cm^2 (1^{st} version) to 5.8 cm^2 (2^{nd} version). Inner parts of the cold finger (not reaching into UHV) were made out of the same materials as the first version (stainless steel SAE 304 and copper). The design of the inner parts did not change significantly, except for simple length corrections. All parts of the second version were produced and are yet to be assembled and tested.

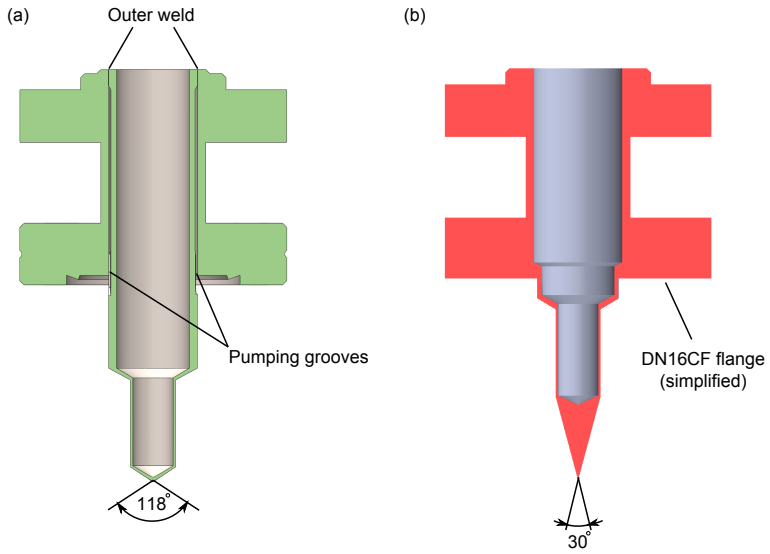

Figure 3.7 | Comparison of (a) first and (b) second version of the cold finger. Both versions are displayed in section view. The inner parts are not displayed as they did not differ significantly between the two versions.

3.3 Experimental procedure

The apparatus (Fig. 3.8) was typically used in the following way. The water drop chamber open to the transfer chamber was evacuated with a turbo molecular pump, and the tubular cryopanel at the entrance was cooled down by LN_2. A typical pressure in the transfer chamber was 3×10^{-8} mbar without a bakeout between experiments. Additional bakeout with heating tapes reduces the pressure to low 10^{-9} mbar range. The inner volume of the cold finger and the exhaust were evacuated with

roughing pumps to remove residual humidity. Counter heating of the upper parts of the tip was set to 40°C and the heating power was regulated by a PID controller. A typical heating power was 10 W (20 V, 0.5 A). The tip of the cold finger was then cooled down, the water drop chamber was separated from the transfer chamber by a gate valve, and H_2O vapor was introduced via an ON-OFF valve (Fujikin). Due to the localized cooling of the cold finger, water froze at the tip where it formed an icicle (see Fig. 3.4c). The thickness of the ice film, *i.e.*, the volume of the droplet, was determined by the time the valve was opened and by the vapor pressure, which, in turn, was controlled by adjusting the temperature of the liquid H_2O reservoir. The growth of icicles is discussed in more detail in section 3.3.3.

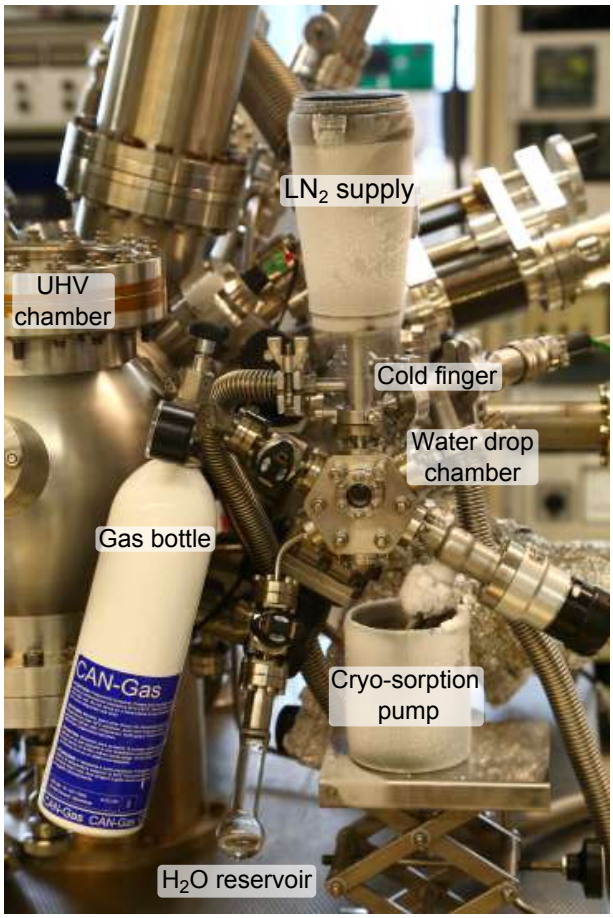

Figure 3.8 | Photo of the experimental setup. H_2O is introduced from the reservoir to the water drop chamber where it freezes on the cold finger cooled by LN_2 from the supply at the top. A gas can be optionally dosed through the inlet at top-left side of the drop chamber. After the experiment, liquid water is pumped from the sample with the LN_2-cooled cryo-sorption pump.

While the icicle was kept at a cryogenic temperature, a sample was transferred

from the analysis chamber of the UHV system, and placed into the water drop chamber directly under the tip of the cold finger. The drop chamber was then closed off from the transfer chamber, and the cold finger was allowed to warm up by closing the inlet of the LN_2 supply. As the tip warmed up, the sample was exposed to the increasing pressure of water vapor evolving from the icicle. Eventually, the icicle melted, and a droplet of liquid water fell on the sample surface. Optionally, additional gas can be introduced to the chamber during this procedure. After appropriate exposure, the water drop chamber was pumped with a cryo-sorption pump (stainless steel container, ~80 cm^2) immersed in an LN_2 bath, and after evacuation, the sample was transferred to the UHV chamber for analysis. Fig. 3.9 shows individual steps of the procedure described above. The following sections discuss practical aspects of the experimental procedure in more detail.

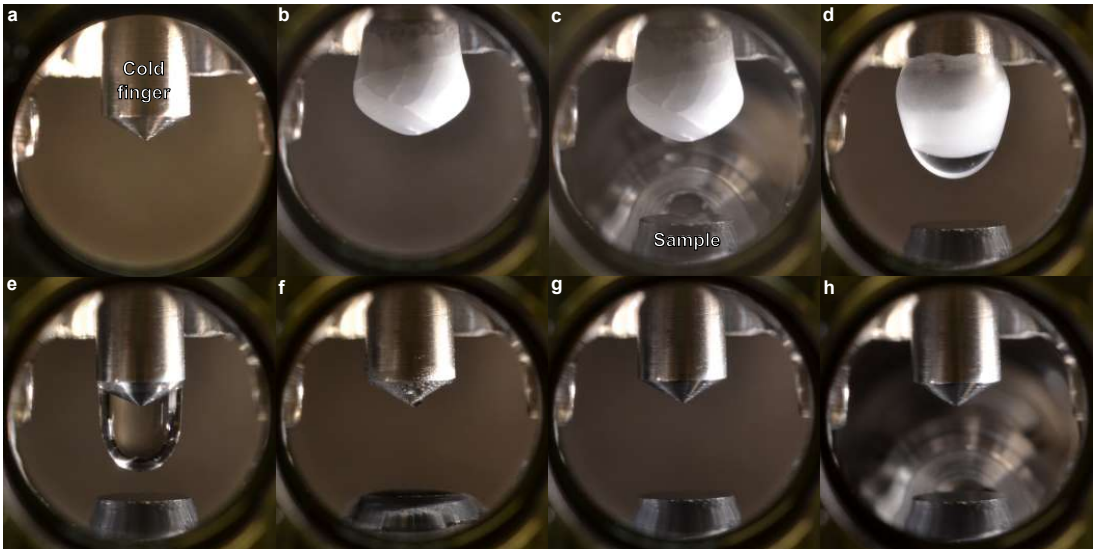

Figure 3.9 | Experimental procedure of dosing liquid H_2O. (a) The cold finger in evacuated drop chamber is cooled with LN_2. **(b)** H_2O vapor is introduced to the chamber, leading to the growth of ice at LN_2 temperature. **(c)** A sample is transferred under UHV and inserted. **(d)** Upon warming up, the ice melts and **(e)** forms a liquid H_2O droplet, which is **(f)** deposited onto the sample. After exposure, **(g)** liquid water is pumped out, and **(h)** the sample is transferred under UHV to the main chamber for analysis.

3.3.1 Cleaning of the H_2O supply

Ultrapure milliQ H_2O (18.2 MΩ cm, ≤3 ppb total organic carbon) was used as a water supply. A closed-end glass-to-metal adapter from Lewvac was modified by

expanding the bottom into a spherical shape to obtain a larger volume and higher mechanical strength. This glass vial was cleaned in boiling H_2O and rinsed extensively with ultrapure H_2O. Afterwards, the vial was filled with fresh milliQ H_2O and mounted to the water drop chamber via a valve (Fujikin). It is important to note that the filling level should not exceed half of the sphere to avoid cracking of the glass due to water expansion upon freezing.

After mounting to the chamber, the water has been exposed to the atmospheric pressure of air for several minutes and already contains dissolved gasses. First, the volume of air above the liquid water is removed by carefully pumping on it with a turbomolecular pump. A negligibly small amount of water is pumped along.

Freeze-pump-thaw cycles are a commonly used method of removing dissolved gases from liquids. This method takes advantage of the pressure-dependent gas solubility in liquid. As stated in Henry's law, the amount of a gas dissolved in a liquid (c_{aq}) is directly proportional to its partial pressure in the gas phase (p_g) above the liquid.

$$c_{aq} = Hp_g \tag{3.1}$$

The proportionality factor H (Henry's law constant) differs for different gases and solvents. Real-life experience of Henry's law is opening a bottle of sparkling water. While closed, the space in the bottle above water is filled with carbon dioxide (CO_2) above atmospheric pressure. As the bottle is opened, the gas escapes and dissolved CO_2 comes out of the solution.

In practice, the volume of water is first cooled down with LN_2 to freeze. After freezing, the headspace above the frozen liquid is evacuated with a turbomolecular pump. Pumping decreases the partial pressure of gases above the liquid, thus lowering their equilibrium concentration in the liquid in the next step. The flask is then sealed, and water is allowed to thaw (thawing can be accelerated by sinking the flask into cold water). As the water is now supersaturated, dissolved gases are released into the headspace upon thawing. The whole cycle is then repeated as many times as necessary.

The first indication that dissolved gases were removed is that the evolution of gas bubbles is no longer observed as the liquid thaws. One should, however, continue with the cycles until no initial pressure increase is detected on the vacuum gauge when pumping above the frozen water.

The primary effect of the freeze-pump-thaw cycles described above removes non-condensable impurities whose vapor pressure at LN_2 temperature is sufficiently high to be pumped out. Apart from that, freeze-pump-thaw cycles can also remove some condensable impurities, albeit at much lower rate. Formic acid as an example has the melting point of 8.4°C, and its vapor pressure is practically zero at LN_2 temperatures. However, it undergoes a spontaneous decomposition into carbon monoxide (CO) and water.[92] CO, as a reaction product, is then removed in every cycle, yielding repeated decomposition of formic acid to re-establish the equilibrium. This way, a sequential dilution leads to the depletion of a condensable impurity from liquid water. As the decomposition rate is temperature-dependent, higher cleaning efficiency might be achieved by warming the liquid water between thawing and re-freezing.

3.3.2 ”Steam-washing” of the drop chamber

In the early experiments with the experimental setup, we found that a UHV-prepared TiO_2(110) sample remained clean after it was left in the water drop chamber for 15 mins without pumping. However, when water vapor (22 mbar at 19°C reservoir temperature) was introduced, carbon contamination could be detected afterwards. Fig. 3.10 shows XPS data for these two cases. We hypothesize that water vapor causes desorption of weakly-bound impurities from the chamber walls by displacing them. To take advantage of this fact, we employed a cleaning procedure, where the water drop chamber was exposed to water vapor at 56 mbar (estimated from temperature-dependence of H_2O vapor pressure) evolving from the reservoir at 35°C for 1 min. Afterwards, the drop chamber was evacuated with the cryo-sorption pump for 30 seconds and then pumped with the turbomolecular pump for ca. 1 min until the base pressure in the transfer chamber was reached. This cleaning cycle was then repeated several times. As demonstrated by the XPS data in Fig. 3.10, the chamber-washing resulted in a cleaner experiment with H_2O vapor.

Alternatively, one can wash the chamber by blank-dosing of a few liquid water droplets (*i.e.*, into the chamber without any sample). The pump-down time is longer, as the volume of water is significantly higher. To expose the sample to freshly-prepared water in a clean chamber, a typical procedure consists of several freeze-pump-thaw cycles, a few ”steam-washing” cycles of the chamber, and a few more freeze-pump-thaw cycles of the H_2O supply just before the experiment.

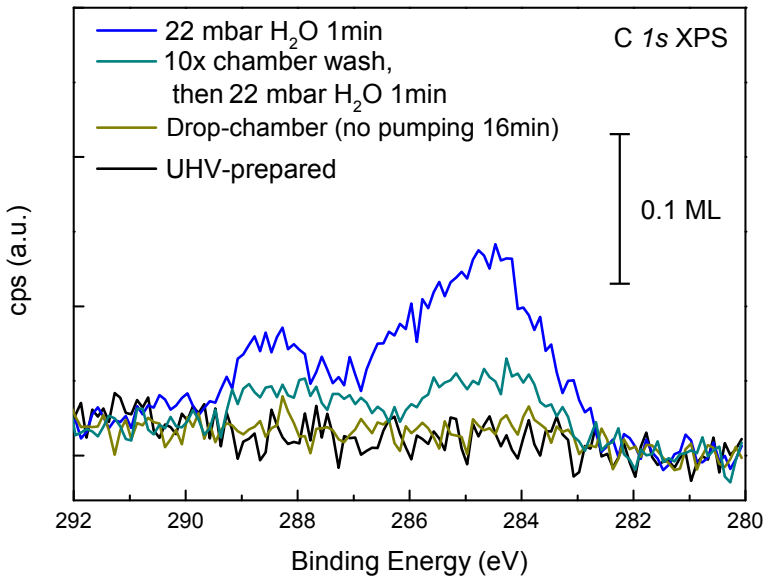

Figure 3.10 | Effect of washing the water drop chamber with H_2O vapor. C*1s* XPS spectra show that a TiO_2(110) sample left in the water drop chamber without pumping remains clean (dark-yellow curve) but gets contaminated in the presence of H_2O vapor (blue curve). Washing of the chamber with H_2O vapor prior to the experiment improves the purity as shown by the light-blue curve. The vertical calibration bar was obtained from the saturation coverage of formic acid (0.5 ML, *i.e.*, one formate per two surface Ti atoms). All XPS data were acquired using Mg Kα X-rays and a SPECS Phoibos 100 analyzer with a pass energy of 40 eV at grazing emission (70° from the surface normal). All spectra were normalized to the low-binding-energy background. The reference spectrum of saturation coverage of formate (not shown) was measured using the same experimental configuration.

3.3.3 Growth of icicles

The most practical conditions for ice growth were found when the water supply was still partially frozen. During the melting process, the ice present in the liquid reservoir stabilizes its temperature at 0°C and vapor pressure at $p_{H_2O}(0\,^\circ\mathrm{C}) = 6\,\mathrm{mbar}$ during the experiment. At this vapor pressure, the optimal time of growth was found to be 40-50 seconds. It is important to note that the cold tip acts as a pump, and unless the reservoir is big enough, its temperature can decrease upon pumping, which further reduces the vapor pressure. A typical volume of the water droplet after the icicle melts is 60 μl using the first version of the cold finger. Smaller droplets are not deposited on the sample as they stay hanging on the tip held by surface tension. Bigger droplets are not desirable, as they come into contact with the sample holder and other parts of the chamber, and can possibly distribute impurities. Also, the pump-down time is longer. Growing an icicle from a warmer (*e.g.*, room-temperature) bath is faster, but difficult to control. At higher vapor pressures $p_{H_2O}(24\,^\circ\mathrm{C}) = 30\,\mathrm{mbar}$, the tip is covered with a thin layer of ice within the first few seconds. Then, more H_2O quickly condenses at the tip. However, the heat transfer through the ice film is not fast enough and a liquid droplet forms. The thermal conductivity of ice is ca. 3.5 W/m K (at −100°C), *i.e.*, almost one order of magnitude lower than that of stainless steel (14 W/m K). It was observed that the liquid droplet suddenly froze, which often lead to cracks in the icicle and pieces of ice frequently falling into the chamber (see pictures of both cases in Fig. 3.11).

Another alternative to reduce the vapor pressure during the growth of the icicle is to pump the water drop chamber with a cryo-sorption pump during the growth. This way a flow from the reservoir to the pump is achieved, and the cold finger is located in the middle of the path (see Fig. 3.2b). This option was tested but not investigated systematically.

3.3.4 Liquid H_2O dosing

The cooling of the cryostat was stopped by inserting a plug into the LN_2 inlet. Interruption of the cooling power is indicated by an immediate temperature increase on thermocouple A. As the tip is warming a liquid droplet forms (typically when the thermocouple A reads around 20°C). Melting of the icicle into a liquid droplet typically takes 5 minutes. During this process, heat is transferred from the counter-

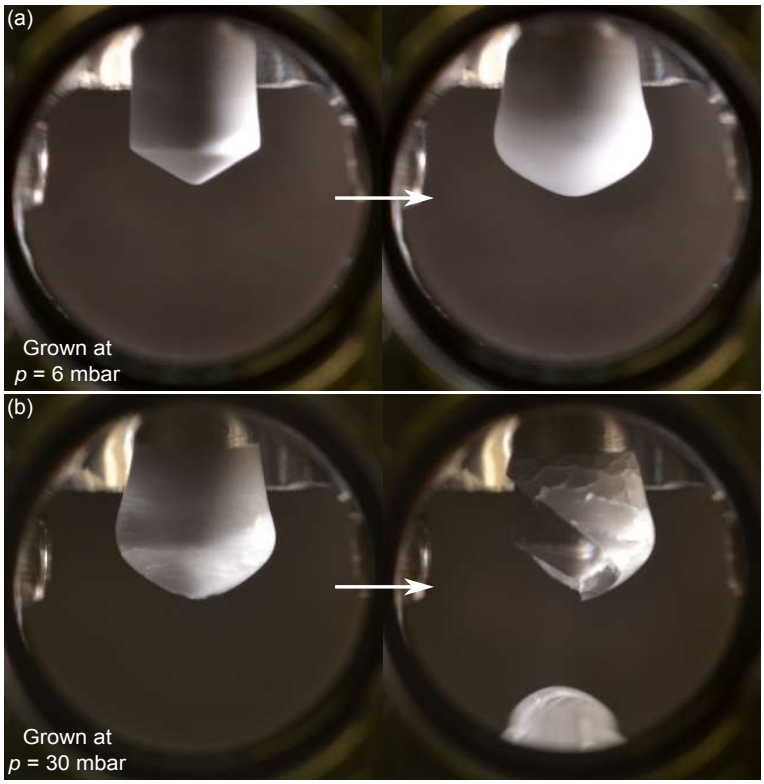

Figure 3.11 | Icicle growth on the LN_2-cooled tip at different vapor pressures of H_2O. (a) Uniform layer as a result of ice deposition at 6 mbar vapor pressure (reservoir at 0 °C, partially frozen), **(b)** Cracked ice with missing pieces created by condensation of liquid water at 30 mbar (reservoir at 24 °C) followed by freezing.

heated upper part to the tip by conduction through a low-conductance thin wall. Faster warming of the tip can be achieved by increasing the counter-heating temperature. Alternatively, dry N_2 gas can be introduced into the exhaust. A flow of (warm) N_2 in reverse direction leads to faster warming of the tip due to additional heat transfer by convection. Both of these options were tested, but they were not used in most of the experiments.

3.3.5 Pumping out

Cryo-sorption is a highly efficient and clean way of pumping water vapor. As water is typically the main gas component in the water drop chamber, a cryo-sorption pump can generate a pressure sufficiently low for transferring the sample back to UHV. In our experience, no pressure increase in the transfer chamber was observed when opening the gate valve between the drop chamber and the transfer chamber after a few minutes of evacuation with the cryo-sorption pump.

We found that additional, highly efficient pumping can be achieved by cooling the tip of the cold finger, which is favorably located in the center of the water drop chamber across from the sample. Pumping with the cold finger was also used in some experiments as a second pump after evacuation with the cryo-sorption pump with the valve to the cryo-sorption pump closed.

When an H_2O droplet is pumped from the sample, a high pumping speed is not always desirable. In response to a sudden pressure drop, the droplet freezes and the resulting block of ice then slowly sublimes from the sample. A more time-efficient way of pumping is to limit the pumping speed to avoid freezing and to pump the droplet from its liquid state. An optimum pumping speed can be achieved by fine-tuning the opening position of the valve to the cryopump. Alternatively, a different cooling bath of the cryo-sorption pump can be used instead of LN_2. Another option would be to adjust and gradually decrease the temperature of the cold finger during pumping, although this is not easily reproducible with the current on-off regulation of the cooling power.

3.3.6 Repeated use of the cold finger

During the early tests of the cold finger, the flow of LN_2 through the cryostat could not always be established or maintained for a longer time. This was attributed to ice

particles from the LN_2 supply which entered the capillary and blocked the flow. After the cold finger was allowed to warm up and evacuated, the flow of the coolant was usually re-established. The particle filter inserted on top of the LN_2 feed adapter (see Fig. 3.4a) solved this issue to a major extent.

However, a similar problem occurred when the cold finger was repeatedly used even with the particle filter present. The first cooling usually proceeded without problems, but after warming during the melting of the icicle, the flow of LN_2 could not be reliably restarted.

This behavior is likely a consequence of inappropriate design of the LN_2 inlet. The inlet adapter (marked yellow in Fig. 3.12) made out of PEEK connects the LN_2 supply to the cold finger. It is mounted to the LN_2 supply and inserted into the outer shell of the cold finger. The outer surface of the inlet adapter and the inner surface of the outer shell were machined with H-class tolerance and designed to be sealed with an O-ring placed in a grove, similar as other components of the cold finger. In practice, the LN_2 supply is removed from the cold finger for drying of the condensed water after each experimental run. As frequent assembly would be impractical, a smaller O-ring was inserted in the groove, which allows for easier assembly before each experiment but may not provide sufficient sealing. We assume that, when the LN_2 inlet is closed during melting of the icicle, and the exhaust is pumped, ambient humidity can enter the inlet volume and freeze on the inner surfaces that are still cold.

In order to use the cold finger repeatedly, humidity should be removed by heating the outer shell (typically with a flow of warm air) after each cooling. After the removal of visible frost by heating with a heat gun was added to the experimental protocol, cooling of the cold finger could be established repeatedly. The second version of the cold finger addressed this issue by sealing the LN_2 inlet with a DN16KF flange between the outer shell and the inlet adapter, providing a face seal with a simple assembly.

3.4 Purity evaluation

The purity of water drops dosed on $TiO_2(110)$ using this apparatus was evaluated and compared with the previously used experimental procedure. XPS data of the C *1s* transition are shown here (Fig. 3.13) to compare the two procedures. In the first

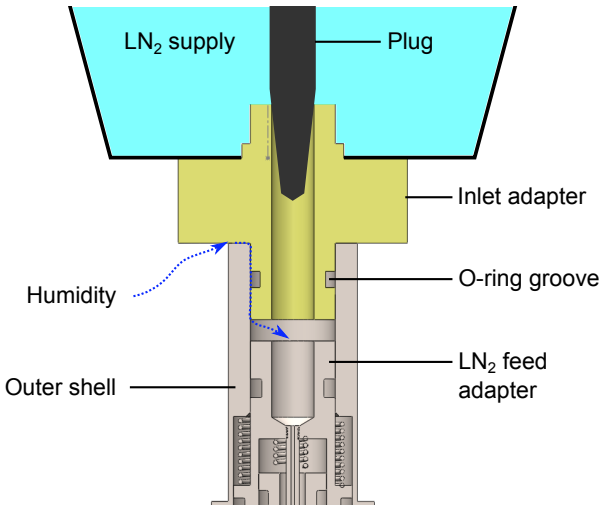

Figure 3.12 | The inlet of LN_2 into the cold finger. Insufficient sealing of the inlet adapter allows ambient humidity to enter and possibly freeze in the capillary. The flow of (humid) air from the environment is indicated with blue dashed arrows.

experiment (green curve in Fig. 3.13), we put a liquid H_2O droplet on a pre-cleaned TiO_2(110) sample inside the transfer chamber after it was vented with high-purity Ar (purity 99.999%, Air Liquide, additionally purified with an inline sorption filter MC50-902 FV from SAES; see section 2.2.1). Outward overpressure flow of argon was maintained during the experiment. Fresh ultrapure H_2O (MilliQ) was deposited onto the sample using a pipette (Eppendorf). The transfer chamber was then evacuated with an LN_2-cooled sorption pump (Ultek, Perkin Elmer) for ca 3 minutes before opening the transfer chamber to a turbomolecular pump running at full speed behind a gate valve. The experiment yielded 0.20 ML of carbon evenly distributed between adventitious C (284.3 eV) and carboxylate C (288.3 eV). In the second experiment (blue curve in Fig. 3.13) a liquid H_2O droplet was deposited on a pre-cleaned sample using the apparatus described here. The latter procedure leads to a visibly cleaner result. After subtraction of the nominally clean UHV-prepared spectrum (black curve in Fig. 3.13), the remaining carbon coverage is 0.04 ML, almost entirely in the form of adventitious carbon. Moreover, adventitious C is not expected to be homogeneously spread on the surface but rather exists in the form of aggregates. All carbon coverages are calibrated using a spectrum of saturation coverage (0.5 ML) of formate ($HCOO^-$) on TiO_2(110) (red curve in Fig. 3.13). This calibration spectrum was produced by dosing excess (10 L = 1×10^{-5} Torr s) of formic acid (HCOOH, Sigma Aldrich, purity 98%) in the main UHV chamber. Upon dissociative adsorption of HCOOH, a dense layer of

formate forms at a saturation coverage of 0.5 C atom per surface unit cell.[93]

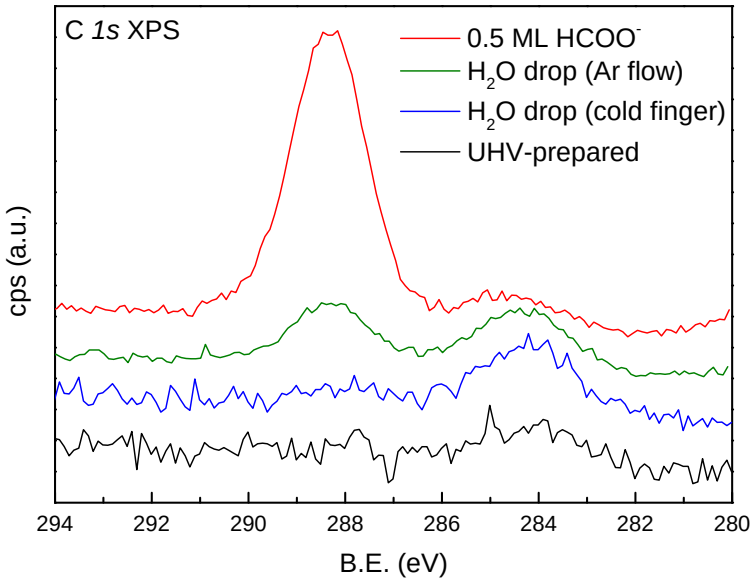

Figure 3.13 | Purity evaluation. C *1s* XPS spectra comparing a liquid H_2O drop deposited on the TiO_2(110) surface with a pipette in purified Ar flow (carbonaceous contamination 0.20 ML) and ultrapure liquid H_2O dosed with the system described here (carbonaceous contamination 0.04 ML). The saturation coverage of formate (0.5 ML) gives a quantitative reference. All XPS data were acquired using Mg Kα X-rays and a SPECS Phoibos 100 analyzer with a pass energy of 40 eV at grazing emission (70°) from the surface normal. All spectra were normalized to the low-binding-energy background and vertically offset for clarity.

The experimental setup described here enabled us to study liquid water on a TiO_2(110) surface without carbonaceous impurities from the air, as reported in ref. [94] and described in detail in chapter 4. Other impurities (*e.g.*, due to leaching of metals from the stainless steel tip) were not observed.

3.5 Limits and potential improvements

Although we managed to carry out experiments clean enough to separate effects of water from those of impurities from the air, we were still able to detect a small (0.04 ML) amount of adventitious carbonaceous contamination. In this pressure range, even trace concentrations of impurities reach a sufficiently high impingement rate for contaminating a sample (if the sticking probability is high enough). Based on experience with the current setup, a number of possible improvements are proposed that could lead to an even higher purity and better overall performance of the setup.

Sharper tip

A typical droplet volume in the current setup is ca. 60 μl. When such a droplet is deposited on a sample, it typically spreads across the edge and also wets the sample holder. Impurities from the sample plate could potentially distribute within the liquid film and contaminate the sample. With the current setup, we were not able to dose smaller droplets as they stayed on the tip held by surface tension. This was already addressed in the second version of the cold finger with a sharper tip apex. It should be capable of dosing smaller droplets, which would also decrease the pump-down time.

Avoid welds

The second version of cold finger also removes the outer weld between the tip and double flange greatly reducing the surface area of the tip. In addition to a potential virtual leak, welds constitute ill-defined surfaces where water can adsorb and displace impurities. Other welds still included in the system should be better avoided (*e.g.*, the welded connecting tube to the H_2O container).

Use stronger springs

When assembling the second cold finger, stronger springs should be used. A leak in low 10^{-1} mbar range in the rough vacuum was attributed to an insufficient force (mainly due to weak spring A) applied to the exhaust tube that is further pressing the heat exchanger into the tip. Recommended springs A, B for the next assembly are 52/2/1 and 57/45/1 providing pressing forces of 16.4 N and 32.2 N, respectively. Spring C is currently almost fully compressed (0.5 mm from the maximum compression) in the working position. It should be replaced with 58/5/1 (41.8 N). Stronger springs will also improve the thermal contact.

Control cooling power

The cooling power could be controlled better by regulating the inlet flow of LN_2. This would be a rather simple modification that would enable a reproducible regulation of the ice temperature. The pumping of the droplet from a sample with the cold finger could also be optimized. We observed that fast pumping with a cryo-sorption

pump or by cooling the cold finger at full cooling power is not a time-efficient procedure. The liquid droplet on the sample usually freezes in response to the sudden pressure drop, and ice then slowly sublimes. An efficient way of pumping would be to keep the cold finger slightly below 0°C. This causes the water to accumulate at the cold tip but does not strongly reduce the vapor pressure and does not lead to freezing. Once all the water from the sample has condensed on the cold tip, the cooling power should be set to maximum to reduce the vapor pressure and enable sample transfer. With a regulation of the cooling power, this procedure can be optimized.

Au-plating

Optionally, the internal surfaces could be plated with Au by sputter deposition to obtain cleaner and better-defined surfaces interacting with water. However, this also involves several uncertainties which should be considered. An interlayer needs to be used as gold does not adhere to stainless steel. The interlayer can introduce additional complexity in case the coating is not compact. Some surfaces cannot be Au-plated (*e.g.*, viewports, valves, the sample plate, etc.) but are still exposed to water during the experiment.

High-pressure cell approach

Currently, the surface area exposed to water vapor is more than 100× larger than that of the sample (see Tab. 3.1). This ratio could be significantly reduced by utilizing a different approach. The sample itself could be cooled down and only its surface exposed to water vapor while maintaining the vacuum in the background. With a sufficient dose, liquid water would condense on the cold surface of the sample. Such a setup would not require the cold finger as a mediator for H_2O transfer.

3.6 Other possible applications

The apparatus was designed to dose liquid H_2O on UHV-prepared samples, and it prioritizes purity from versatility. It offers, however a number of other applications. **Clean dosing of other liquids:** the system could equally be used for dosing other liquids whose vapor pressure is sufficiently low at LN_2 temperatures. Alternatively, more expensive liquid He could be used as a cooling agent.

Dosing isotopically labeled liquids: as example dosing liquid isotopically labeled $H_2^{18}O$ on the oxide surface. Then, the ^{16}O (from the crystal lattice) and ^{18}O (from water) can be distinguished with low-energy ion scattering or by a mass spectrometer upon desorption.

Mixing liquids: Dosing two or more liquids either sequentially or simultaneously, by adding multiple reservoirs. Their vapor pressures would be set by controlling temperatures of baths.

Preparing a solution *in-situ*: besides dosing evaporable liquids, a solution of a solid substance could be prepared directly on a sample. A certain amount of salt would be transferred on the surface, and then diluted with a droplet of pure H_2O. Provided that the sample is electrically insulated from the chamber and contacts for other electrodes are included, such a setup could work as a simple electrochemical cell in a droplet.

Contact angle measurements: The viewports on the chamber provide good visual access to the sample surface. Contact angles of liquids wetting well-defined samples in a well-defined environment could be measured similar as in ref. [95].

Experiments with UV light: if UV-grade viewports are used, this setup presents a controlled environment for UV-illumination of samples in contact with liquids and a variety of gases. Focused UV-light (or using an aperture to crop the beam) is preferred in order to illuminate the sample surface only and prevent UV-induced desorption from the chamber walls. In the current geometry, the front viewport allows an incidence angle of 69° from the surface normal and the side viewport 62° from the sample normal. The viewport in the front is preferred, as it is closer to the sample and the view from the side is partially blocked by the sample receptacle.

Localized cooling: a similar setup could be used as a miniature cryostat to locally cool a sample or a part inside a UHV chamber, *e.g.*, to avoid undesirable condensation of gases on other surfaces. Because the cold finger is mounted on DN16CF flange (1.33 in. outer diameter), it offers a compact alternative to commercially available cryostats.

Study of ice growth: condensation or ice growth of various well-defined substances can be studied in different temperature/pressure regimes and optionally in the background of a variety of gasses. The shape and roughness of the cold surface where condensation occurs can be adapted for that purpose.

Chapter 4

Interaction of TiO_2 rutile (110) with liquid H_2O and air

This chapter is based on an article, ref. [94]. The chapter, however, contains additional data and information.

4.1 Introduction

Recently the solid-liquid interface at the predominant (110) face of TiO_2 rutile has been a subject of considerable interest. Most of these studies have been motivated by the need to understand the interfacial structure of this photocatalytic material under operation conditions, where TiO_2 is often in contact with an aqueous electrolyte solution. Upon exposure to liquid water or humid air, the formation of a molecularly ordered overlayer with a two-fold periodicity along the Ti rows was reported by several groups.[96–99] However, the interpretation of the chemical origin of this overlayer has been controversially discussed in these publications. Hussain et al.[96] attributed the (2×1) overlayer to an ordered array of hydroxyl groups (OH) with ordered molecular water in the second layer. This interpretation was supported by a previously observed two-fold periodicity on the TiO_2(110) surface characterized by STM in liquid water.[97] In another STM study of TiO_2(110) exposed a humid environment, Sasahara, et al.[98] observed two kinds of oxygen-containing species terminating the surface Ti atoms with different apparent heights. Based on XPS, the ordered array was assigned to be composed of hydroxyl groups (OH) and hydroperoxyl groups (OOH) formed from O_2 and H_2O. All the publications discussed above implied mo-

lecular ordering of interfacial water at the surface. None of them, however, presented convincing spectroscopic data, that would exclude the presence of impurities. The results presented in ref. [99] show XPS data of TiO_2(110) surface exposed to liquid water and air with a relatively strong signal in the C*1s* region. Here, the observed overlayer was attributed to bicarbonate (HCO_3^-) formed by reaction of atmospheric CO_2 with H_2O, while the bridging bidentate adsorption geometry of bicarbonate results in the (2×1) symmetry.

Our early experiments were performed by depositing a droplet of liquid water with a pipette in the vented transfer chamber, as described in chapter 2, section 2.2.1. The surface structure observed after such exposure agreed with the previously published results. However, the observed (2×1) overlayer was always accompanied by a perceptible (~0.3 ML) XPS signal in the C*1s* region. The ability to perform clean experiments and discriminate the effect of water from impurities was the primary motivation for constructing the apparatus for dosing pure liquid water in UHV-compatible conditions (as described in detail in chapter 3). The results obtained with this apparatus show that the previously observed molecularly ordered structure indeed was an experimental artifact due to carbonaceous impurities. The TiO_2(110) surface was shown to retain its UHV-like (1×1) surface structure upon exposure to liquid water. Moreover, by controlled dosing of gases into the water drop chamber and several reference experiments we were able to exclude the formation of a self-assembled bicarbonate monolayer from atmospheric CO_2. Instead, the ordered overlayer was identified to originate from adsorption of atmospheric carboxylic acids. These, although present at relatively low concentrations in air, adsorb with high affinity, effectively displacing other adsorbates as discussed in the following.

4.2 Results

4.2.1 Clean liquid H_2O

A TiO_2(110) sample (SurfaceNet, top-hat shape, $\phi = 6\,\text{mm}$, $h = 2\,\text{mm}$, top polished) was prepared in the main UHV chamber by cycles of Ar^+ sputtering (1 kV, 0.6 μA/cm^2, 15 min) and annealing (750°C, 15 min). Every 5-10 cycles, the sample was annealed in O_2 (1×10^{-6} mbar, 600°C, 20 min) instead of UHV, to replenish oxygen vacancies and avoid an overly reduced surface. After the preparation, the surface

was regularly characterized with XPS, and occasionally also with other techniques. Afterwards, the UHV-prepared sample was transferred into the drop chamber, and a droplet of liquid water was dosed on the surface according to the procedure described in chapter 3, section 3.3. After evacuation, the sample was reintroduced to the main chamber and analyzed. STM characterization was always performed first to avoid possible beam damage by other techniques. Fig. 4.1 shows a set of STM images of TiO_2(110) surface. The image of the clean, UHV-prepared surface is in Fig. 4.1a. The five-fold coordinated surface titanium atoms are imaged as bright rows. The bright protrusions within the dark rows are oxygen vacancies induced by preparation in UHV.[56] The image after exposure to pure liquid H_2O using the newly-constructed apparatus (Fig. 4.1b) clearly shows the retention of the (1×1) surface structure. The vacancies are converted into hydroxyls upon dissociative adsorption of molecular water on such defects.[100] For comparison, an STM image of the surface after water was deposited using a pipette in the vented transfer chamber is shown in Fig. 4.1c. Here, the formation of an ordered overlayer was observed with two-fold (ca. 6 Å) spacing between the protrusions along the rows.

4.2.2 Identification of impurities

While a structural difference is obvious between STM images in Fig. 4.1b and Fig. 4.1c, spectroscopic information is essential to identify the chemical origin of the ordered overlayer. Fig. 4.2 shows the XPS spectra corresponding to the individual STM images in Fig. 4.1. After liquid water was deposited using the newly-constructed apparatus (cold finger, blue curves in Fig. 4.2), only a minor increase in the C *1s* region was observed at 284.3 eV. The peak corresponds to so-called adventitious carbon and is likely observed in the STM image (Fig. 4.1b) in the form of aggregates (white blobs) on top of the (1×1) surface. Molecular water adsorption was not detected as is demonstrated by the absence of a peak in the O *1s* spectrum at the expected 534.2 eV (~ 3.5 eV higher binding energy than lattice O).[35] The small deviation from the UHV-prepared surface (black curves) on the high-binding-energy side of the O *1s* peak is attributed to dissociative adsorption of water on oxygen vacancies. From the presented data we conclude that water by itself does not form an ordered overlayer, that persists in vacuum at room temperature.

When liquid water was deposited with a pipette (Fig. 4.1c), the sample was exposed

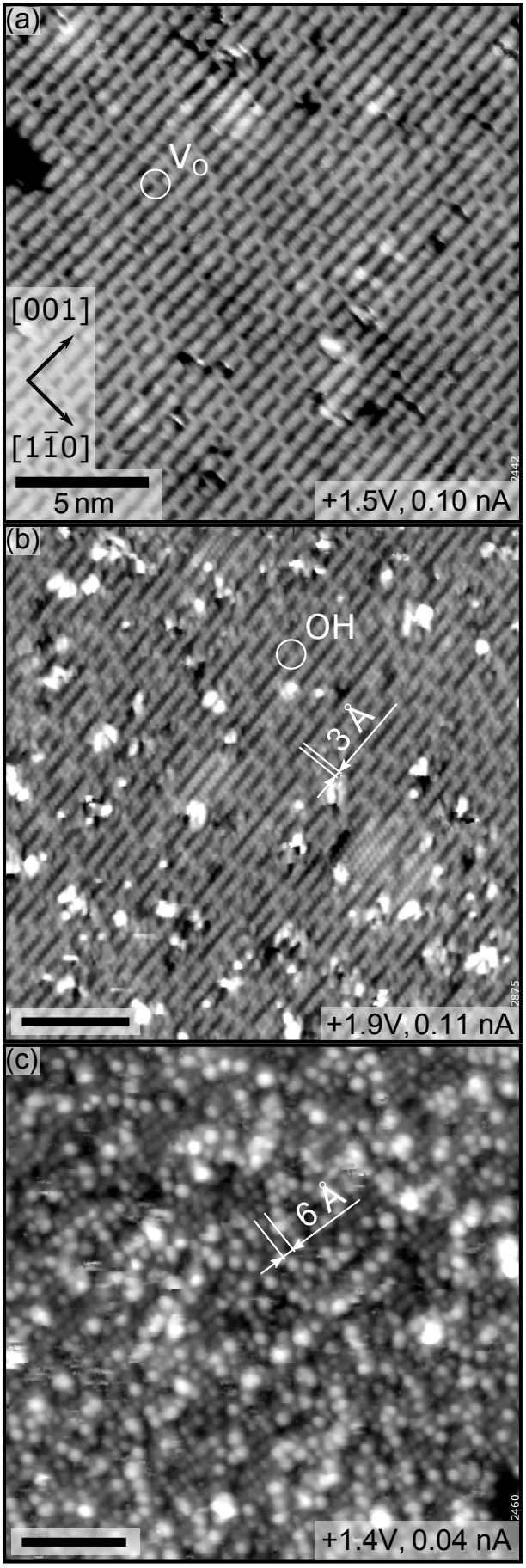

Figure 4.1 | STM images of TiO_2 rutile (110) (a) UHV-prepared surface, **(b)** surface after exposure to liquid water using the newly-constructed apparatus, **(c)** liquid water deposited with a pipette in the vented transfer chamber. Crystallographic directions and the size of the scale bar are the same in all three images.

to air for a few seconds, although a flow of ultrapure argon was maintained around the sample. After such an exposure, a significant increase in the C*1s* region was detected (dark-yellow curve). Two peaks were observed, the adventitious carbon and a second smaller peak at 288.3 eV (~ 4.0 eV higher in binding energy). The graphs in Fig. 4.2 contain also reference XPS data of a saturation coverage of formate ($HCOO^-$, red curves), discussed below. The spectra summarized here were acquired over an extended period of time and varied in intensity primarily due to geometry adjustments and detector calibration between the experiments. To correct for the different experimental sensitivities, the substrate transitions (Ti*2p* and O*1s*) were normalized to their peak values, and the same normalization factors were applied to the C*1s* spectra. A Shirley background was subtracted from each spectrum. The dark-yellow C*1s* spectrum (H_2O dosed with a pipette) also contains the analyzer-induced carbon signal (early experiment), although its contribution is insignificant here. The remaining C*1s* spectra were obtained with the biased sample to remove the artificial carbon and corrected for the shift in energy.

Apart from carbon, no other impurities were detected by XPS for H_2O dosed with a pipette under Ar flow as shown in the overview spectra in Fig. 4.3. Here, a spectrum acquired at normal emission is compared to the spectrum recorded at grazing emission for higher surface sensitivity. The figure also demonstrates that overview spectra are not suitable for assessing surface cleanliness, in particular for elements with low sensitivity factor such as carbon.[101,102] Although a notable carbon peak was well resolved in the detailed C*1s* spectrum (Fig. 4.2), it appears insignificant in the overview spectrum (Fig. 4.3, dark-yellow line), which is dominated by intense Ti and O bulk transitions. In normal emission (Fig. 4.3, green line), the carbon peak is barely visible. In contrast, argon implanted into the bulk by sputtering[103] is detected only in normal emission.

Formic acid on TiO_2(110)

Formic acid (HCOOH) provides a quantitative reference for the level of carbonaceous impurities on TiO_2(110). Upon gas-phase dosing into UHV at room temperature, HCOOH adsorbs dissociatively in bridging bidentate geometry, where each formate ion ($HCOO^-$) is bound to two neighboring surface Ti atoms.[22,93] The dissociated proton (H^+) binds to bridging oxygen forming a hydroxyl group (OH_b). The

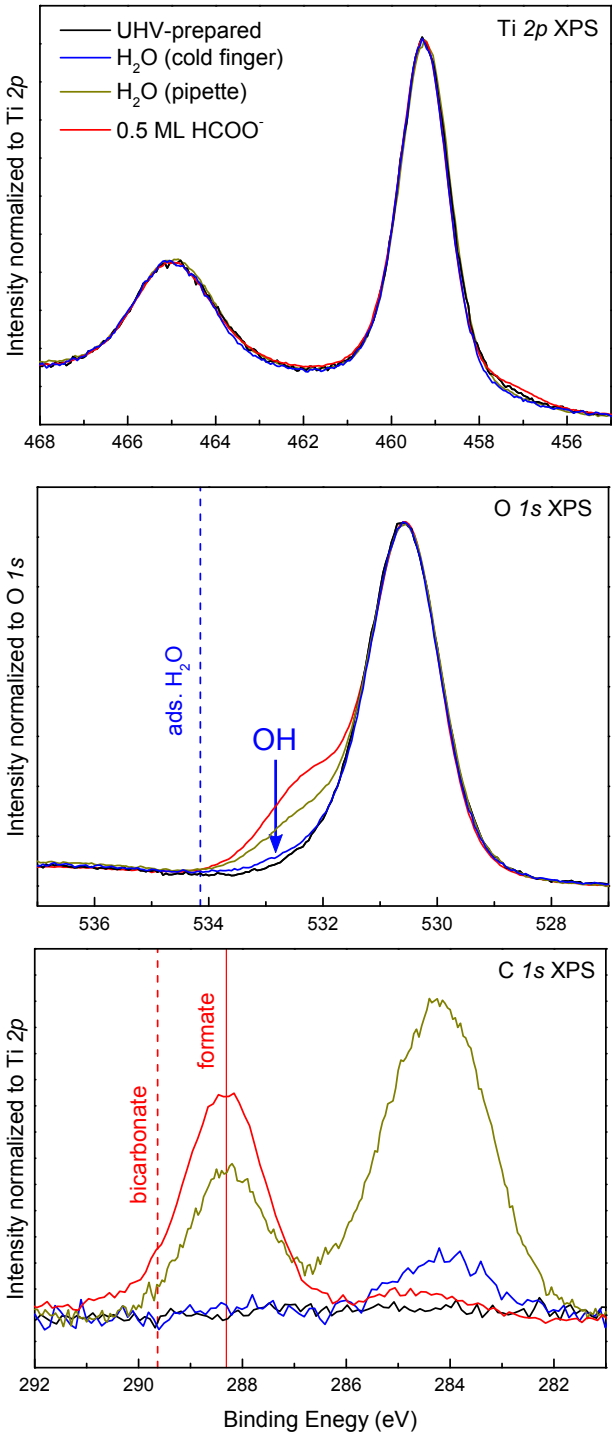

Figure 4.2 | Detailed XPS spectra (Ti*2p*, O*1s*, C*1s*) after exposure of TiO_2(110) to liquid H_2O. The black curves were measured after preparation in UHV. The blue curves show the sample after exposure to pure H_2O in the water drop chamber. Dark-yellow curves correspond to liquid water deposited with a pipette in the transfer chamber vented with argon. A reference spectrum of the saturation coverage of formate (here defined as 0.5 ML) is shown in red. The (unobserved) transitions of molecular water (at 534.2 eV in O*1s*) and bicarbonate (at 289.6 eV in C*1s*) are marked with vertical lines at their expected positions. O*1s* and Ti*2p* spectra were taken with 20 eV pass energy, C*1s* with 40 eV. All spectra were acquired at grazing emission (70° or 80°) from the sample normal.

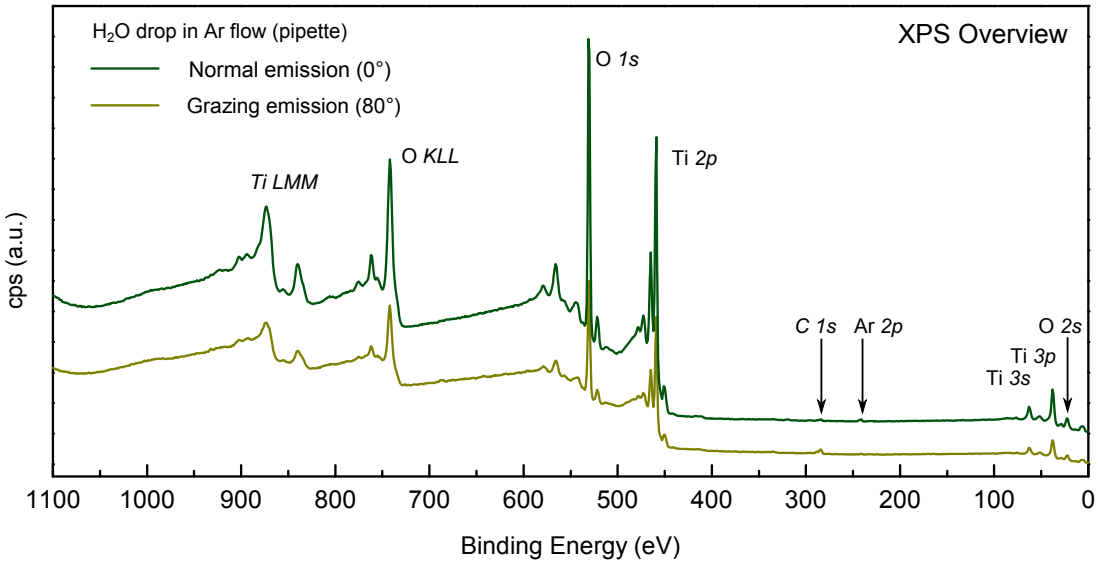

Figure 4.3 | Overview XPS spectra of H_2O deposited in Ar flow. Both curves (normal and grazing emission) correspond to the STM image in Fig. 4.1c and the dark-yellow detailed XPS spectra in Fig. 4.2. Both spectra were obtained with Mg Kα X-rays at 60 eV pass energy. Spectra are plotted without processing, vertically offset for clarity.

adsorption is self-limited at a saturation coverage of 0.5 ML (one formate per two surface unit cells). Saturation coverage can be thus produced by dosing excess of HCOOH, here by dosing 10 L = 1×10^{-5} Torr s into the main UHV chamber. The XPS spectra of formate shown as red curves in Fig. 4.2 also provide a chemical reference to the identity the unknown ordered overlayer in Fig. 4.1c.

As apparent from the C*1s* spectra in Fig. 4.2, the peak position of formate (red curve, peak at 288.3 eV) is identical with the higher-binding-energy peak after liquid water was deposited in air (dark-yellow curve, peak at 288.3 eV). The previously-proposed bicarbonate[99] would also adsorb in bidentate geometry, but the binding energy of the C*1s* transition would differ. In contrast to formate (C oxidation state +2), in bicarbonate, C is formally in oxidation state +4, which is estimated to yield a shift by $\sim$ 1.32 eV towards higher binding energy.[94] A peak corresponding to bicarbonate was not observed in any of the C*1s* spectra. The oxygen atom within the formate group, together with the OH_b formed by dissociation of HCOOH are responsible for the distinct shoulder at the high-binding-energy side of the O*1s* peak (Fig. 4.2, red curve). A similar, although less pronounced shoulder was observed in the O*1s* spectrum of the air-exposed sample (Fig. 4.2, dark-yellow curve). An STM image of saturation coverage of formate on TiO_2(110) is shown in Fig. 4.4a. The

bridging bidentate adsorption geometry results in the two-fold periodicity (ca. 6 Å) along the [001] direction (surface Ti rows). A similarly ordered formate monolayer was obtained by deposition of HCOOH from solution, see ref. [94]. The same bidentate geometry would also occur in case of other carboxylates[104] with longer chains (*e.g.*, acetate[105,106] or benzoate[106–108]). A schematic model of the binding geometry of carboxylates $RCOO^-$ is displayed in Fig. 4.4b.

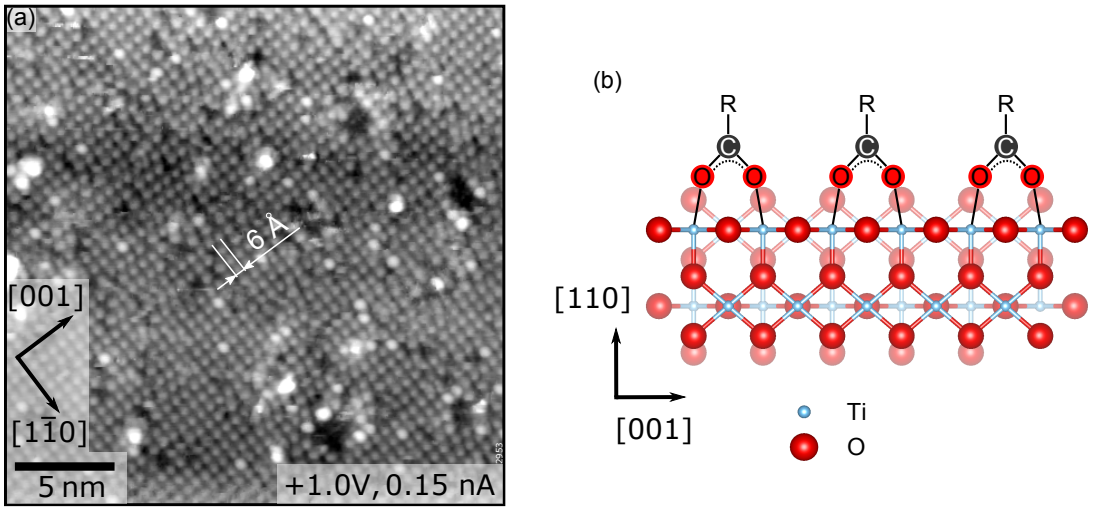

Figure 4.4 | Bidentate adsorption of carboxylates on TiO_2(110) (a) STM image of a saturation coverage (0.5 ML) of formate from adsorption of formic acid in UHV (corresponding to the XPS data in Fig. 4.2, red curves). **(b)** Schematic model of the bridging bidentate adsorption geometry of carboxylates on TiO_2(110).

The bidentate adsorption geometry and primarily the identical peak position of C *1s* XPS provide evidence that the ordered overlayer on TiO_2(110) exposed to air is composed of carboxylates. The kind of carboxylate, however, cannot be directly identified with STM and XPS as longer carboxylates (*e.g.*, acetate or propionate) would adsorb in the same bidentate geometry. The carbon atom within the carboxylate group would have very similar binding energy[109], and the longer aliphatic chain would only contribute to the adventitious contamination signal at 284.3 eV.

Analysis of the STM images

As apparent from the STM image in Fig. 4.1c, the apparent heights of the ordered protrusions are not uniform, unlike in the STM image of the formate saturation coverage in Fig. 4.4a. A histogram obtained by analyzing the apparent height distribution of individual maxima of the STM image in Fig. 4.1c is shown in Fig. 4.5a. The

distribution can be fitted with a sum of two equal-width Gaussian functions with relative spacing of 0.72 Å and 77:23 ratio in favor of the shorter species. To compare the experimental height distribution with possible combinations of carboxylates, STM images of monolayers consisting of two different carboxylates on TiO_2(110) were simulated by DFT.[94] The smallest height difference of 0.63 Å was obtained for mixed formate/acetate monolayer (Fig. 4.5b,c) in good agreement with the experimental value (0.72 Å). A somewhat larger height difference of 0.95 Å was found in simulated STM of mixed acetate/propionate monolayer, see ref. [94] for details. Any longer carboxylates in the form $CH_3(CH_2)_nCOO^-$ and $CH_3(CH_2)_{n+1}COO^-$, where n >1, would have a height difference of 0.95 Å due to the additional $-(CH_2)-$ unit in the aliphatic chain. The STM simulations and height analysis were performed by Melissa Hines.

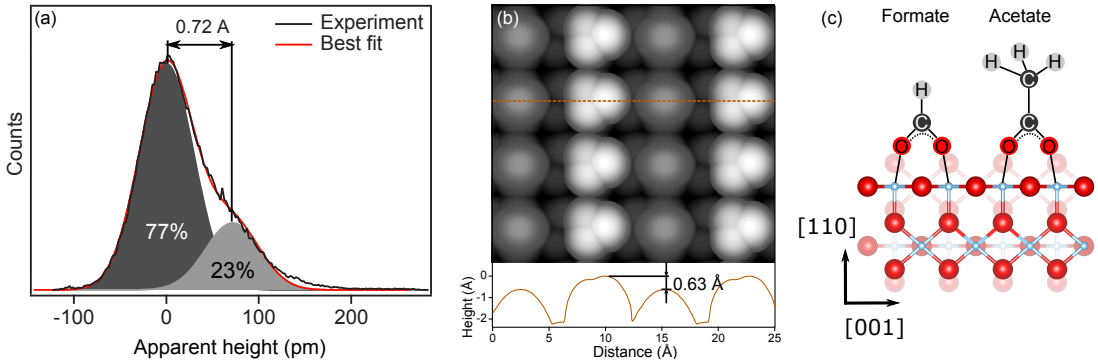

Figure 4.5 | STM height analysis and STM simulation of mixed carboxylate monolayer on TiO_2(110) (a) Apparent height distribution of STM image (Fig. 4.1c) after an H_2O drop was deposited in air, **(b)** simulated STM image of mixed formate/acetate layer on TiO_2(110) including a line profile along the dashed, orange line **(c)** schematic model of adsorbed formate and acetate.

The experimental height distribution of Fig. 4.1c is consistent with the simulated mixed formate/acetate monolayer. A very similar height distribution with the same height difference was obtained by analyzing STM images of a TiO_2(110) sample exposed to air in a distant location, at Cornell University in Ithaca, NY. The fit of the apparent height distribution yielded 0.72 Å height difference between the two species with 84:16 ratio.[94] The binding energy of the C *1s* transition of the sample exposed to air in Ithaca agreed with those of solution or vapor-deposited formic acid.

Conclusive evidence of the adsorbate identity was provided by polarized infrared absorption spectroscopy of air-exposed TiO_2(110) sample. Formate is the only carboxylate terminated by a single C–H bond oriented normal to the surface (see Fig. 4.5c); the

structure thus leads to a characteristic signature in the infrared spectra. A distinctive pair of C−H stretch resonances polarized perpendicular to the surface was detected on the air-exposed sample as well as on intentionally deposited formate monolayer (see ref. [94] for the IR data and detailed discussion). The experiments at Cornell University, Ithaca, were performed by William DeBenedetti and Melissa Hines.

Identifying that a mixture of formate and acetate terminates the TiO_2(110) surface exposed to air naturally raises a question about the possible origin of these adsorbates. We first explore the option that these carboxylates are produced by a chemical reaction of an atmospheric gas with liquid water occurring at the surface.

4.2.3 Reactions of gases with liquid H_2O

The co-exposure experiments of gases with liquid water were conducted in the following way. A droplet of pure water was deposited on the UHV-prepared sample according to the procedure described in Chapter 3, Section 3.3. The drop chamber was then backfilled with a chosen gas typically at a pressure of ∼ 1 bar. In practice, a small evacuated volume attached to the drop chamber was valved off and filled with a gas from a bottle to a pressure of ∼ 8 bar. The bottle was then separated by another valve, and the pressurized gas was released into the drop chamber. The resulting pressure in the drop chamber was determined by the ratio of the volumes of the two chambers. The experiment was performed with a variety of gases: CO_2, CO, Ar, and O_2. In all experiments, the pressure of the gas in the drop chamber exceeded the partial pressure in the air by several orders of magnitude. The gas was allowed to react with the water drop on the sample for 10 minutes, and after that exposure, the drop chamber was evacuated with a cryo-sorption pump to trap the H_2O and thereafter with a turbomolecular pumping station (TSH 071 E from Pfeiffer) to pump the non-condesable gas. After evacuation, the sample was transferred to the main UHV chamber for analysis. Carbon dioxide (CO_2) dissolves in liquid water [CO_2(aq)] and undergoes hydrolysis into carbonic acid (H_2CO_3). The acid then dissociates a proton forming a bicarbonate ion, as described by the equilibrium:[110]

$$CO_2(aq) + H_2O(l) \leftrightarrow H2CO_3(aq) \leftrightarrow H^+ + HCO_3^- \tag{4.1}$$

At atmospheric conditions (partial CO_2 pressure 0.4 mbar), the equilibrium con-

centration of carbonic acid is estimated to be 10^{-8} mol l^{-1}.[94] As previously proposed,[99] bicarbonate is expected to adsorb on the $TiO_2(110)$ surface in the bridged bidentate configuration forming a (2×1) layer. Fig. 4.6a,b show the O*1s* and C*1s* spectra after such a reaction with 1 bar of CO_2 (purity 99.998% from Messer CANGas). Although during the experiment the pressure of CO_2 and thus the concertation of carbonic acid was several orders of magnitude higher than in the ambient atmosphere, no bicarbonate was observed in the C*1s* spectrum (Fig. 4.6b). Instead, a peak corresponding to formate was detected at the same binding energy as the peak on the air-exposed sample. The vertical bar in Fig. 4.6b indicates the position and intensity of half-saturation coverage (0.25 ML) of formate. After the reaction of 1 bar of CO_2 with liquid water, the measured formate coverage is approximately one-quarter of the saturation.

Similarly, carbon monoxide (CO) dissolves in water and undergoes hydrolysis into formic acid (HCOOH):

$$CO(aq) + H_2O(l) \leftrightarrow HCOOH(aq) \leftrightarrow H^+ + HCOO^- \tag{4.2}$$

Although CO is present in the atmosphere at much lower concentrations (partial pressure 10^{-4} mbar), the estimated equilibrium concentration of formic acid in water is 10^{-7} mol l^{-1}, somewhat higher than the concentration of carbonic acid.[94] Thermochemical calculations to estimate the concentrations of carbonic and formic acids formed by hydrolysis of CO_2 and CO, respectively (equations 4.1 and 4.2), were performed by Melissa Hines and are described in detail in ref. [94]. The XPS spectra after reaction of 1 bar of CO (Messer, purity 99.998%) shown in Fig. 4.6b,c display again a peak at formate position in the C*1s* region. The peak intensity corresponds to less than half the saturation coverage, similar as in the previous experiment with CO_2.

As no production of bicarbonate and formate was observed upon reactions with CO_2 and CO with liquid water, control experiments were conducted with other gases, argon, and oxygen. Exposure to liquid H_2O in argon (Air Liquide, 99.999%, additionally purified with an in-line sorption filter as described in chapter 2, section 2.2.1) resulted in the lowest intensity increase in the C*1s* region (see Fig. 4.6e,f), whereas after the reaction of O_2 (Messer CANGas, 99.999%) with liquid H_2O (see Fig. 4.6 g,h), the carbon signal was even higher than that of CO and CO_2. In all experiments,

the binding energy of the C*1s* peaks agreed with a carboxylate (at 288.3 eV, dashed vertical line) and adventitious carbon at 284.3 eV.

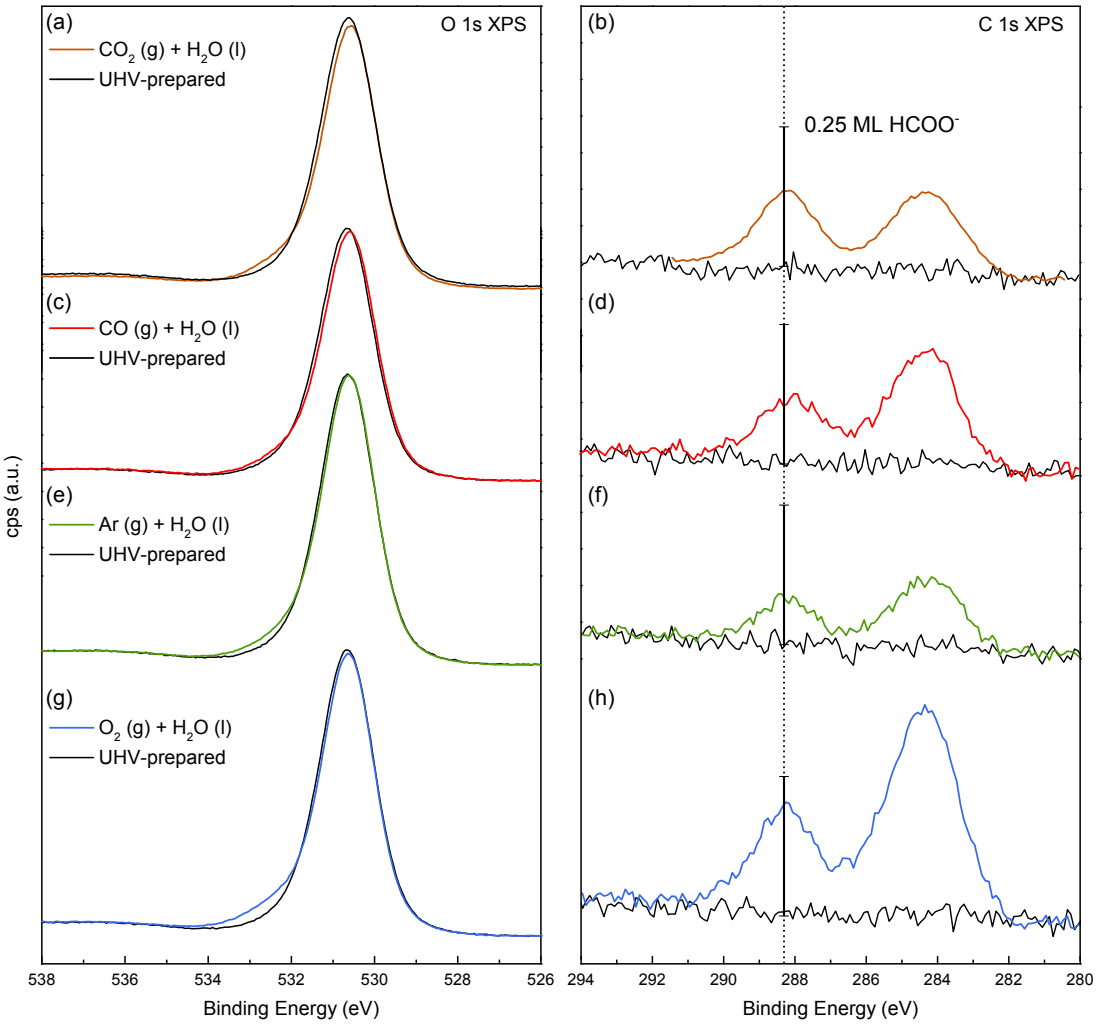

Figure 4.6 | XPS spectra of TiO_2(110) after simultaneous exposure to liquid H_2O and ~ 1 bar of gas (CO_2, CO, Ar, O_2). The vertical bar in all C*1s* spectra represents half the saturation coverage (0.25 ML) of formate at its binding energy. All data were collected at grazing (70°) emission from the surface normal and normalized to the low-binding-energy background. All spectra were measured with the sample biased and corrected for the resulting energy shift. Thus none of them contains the artificial carbon signal from the analyzer.

The surface structure observed by STM after exposure to liquid H_2O in the background of gases (Fig. 4.7) is visually similar to the structure of an air-exposed sample (Fig. 4.1c). The density of adsorbates is consistent with the fractional monolayer coverage in agreement with the XPS results (Fig. 4.6). Images of the surface after exposure to liquid H_2O in CO_2 background (Fig. 4.7a) and liquid H_2O in O_2 background

(Fig. 4.7b) are shown below. In areas of higher adsorbate density, the two-fold periodicity along the [001] direction is observed.

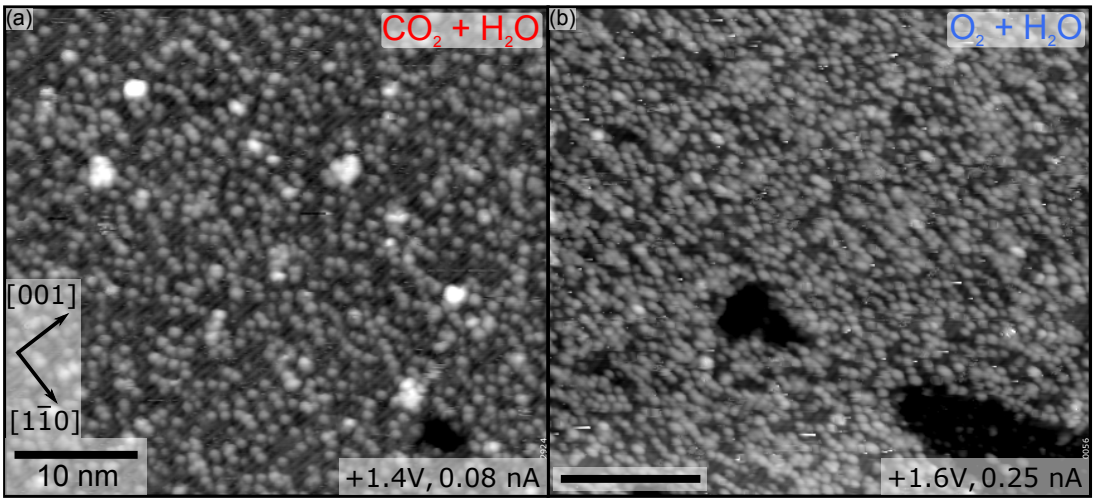

Figure 4.7 | STM images of TiO_2(110) after simultaneous exposure to liquid H_2O and ~ 1 bar CO_2 and O_2. Image **(a)** corresponds to the XPS spectra in Fig. 4.6a,b; image **(b)** corresponds to Fig. 4.6g,h. Crystallographic directions and the size of the scale bar are the same in both images.

4.3 Discussion

The co-dosing experiments exclude the formation of substantial amounts of carboxylic or carbonic acids on air-exposed TiO_2(110) surface by a chemical reaction of atmospheric CO or CO_2. The calculated concentration of formic acid resulting from 1 bar of CO in equilibrium with liquid H_2O is 0.36 mol l^{-1}, sufficient to saturate the surface. For comparison, dense formate monolayers were deposited from a solution of 0.1 mol l^{-1} HCOOH.[94] Only a fraction of monolayer was detected upon exposure to H_2O and CO, which we attribute to the slow kinetics of CO hydrolysis (eq. 4.1).[92] No reaction between CO_2 and liquid H_2O was observed, although a 6×10^{-5} mol l^{-1} solution of carbonic acid is expected at these conditions.[94] The absence of adsorbed bicarbonate during the XPS analysis is attributed to the fast decomposition of carbonic acid to CO_2 in the presence of trace H_2O.[111] The presence of the same spectroscopic features (see Fig. 4.6) upon exposure to other gases (Ar, O_2) indicates a common impurity in the gases or contamination displaced from the chamber walls by gas at high pressure. The experiments were very sensitive to even trace concentra-

tions of strongly adsorbing impurities due to the extremely high doses (10^{12} L, where 1L = 10^{-6} Torr s) of gases.

Alternatively, we consider the adsorption of carboxylic acids directly from the atmosphere to explain the formation of carboxylate layer on air-exposed samples. Formic and acetic acids are the main sources of atmospheric acidity with typical partial pressures of 10^{-6}-10^{-7} mbar of each acid, depending on the geographic location.[112] The dominant sources of formic and acetic acids are biogenic, in particular, the oxidation of isoprene from trees and bushes. Carboxylic acids with longer chains have a much lower concentration in the atmosphere.[112] Both formic and acetic acid are rapidly and efficiently adsorbed by liquid water from their gas phase. In an ambient environment, the concentrations of formic and acetic acids in liquid H_2O is $\sim 10^{-5}\,\mathrm{mol\,l^{-1}}$, orders of magnitude larger than the concentrations of formic and carbonic acids produced by hydrolysis of atmospheric CO and CO_2 (eq. 4.2 and 4.1). A similar concentration is also expected at surfaces of air-exposed samples due to the spontaneously-formed an H_2O film,[27] where the facile trapping of gaseous carboxylic acids can occur. The concentrations of formic and acetic acids in liquid water in equilibrium with their gaseous phases were estimated by Melissa Hines from Henry's law coefficients of the acids[113], see ref. [94] for details.

Gaseous carboxylic acids are relatively minor components of the atmosphere, compared to other small molecules, such as alcohols (the atmospheric partial pressure of methanol is 10^{-2}-10^{-3} mbar).[114] However, species with monodentate binding (such as alcohols[115] and amines[116]) are significantly less stable and usually desorb already near room temperature. Carboxylates, in contrast, are bound in bidentate configuration to the surface, which leads to a substantial enhancement of their stability and the desorption occurs at significantly higher temperatures.[117] The bidentate bonding geometry of carboxylic acids, therefore, leads to a high adsorption affinity, effectively displacing other species present at much higher concentrations in the atmosphere.

Adsorption of atmospheric carboxylic acids explains the (2×1) ordered overlayer formed on the TiO_2(110) surface upon exposure to air as observed here (Fig. 4.1c) and by several groups[96–99] in different locations. The coverage of carboxylates was shown to self-limit at saturation coverage (0.5 ML) upon ~ 30 min exposure to air.[94]

4.4 Conclusion

Our finding might elucidate a part of the complex phenomenon of photoswitching of TiO_2, utilized in self-cleaning and anti-fogging coatings.[118] The TiO_2 surface is known to turn hydrophilic upon irradiation with UV light in the ambient environment, while in the dark, the surface slowly returns to its hydrophobic state. The UV-induced hydrophilicity was later explained as the removal of hydrophobic hydrocarbons from the surface by photooxidation.[119] The previously unexplained reverse dark reaction can be rationalized by the adsorption of atmospheric carboxylic acids as shown above.

Depending on the actual concentration of carboxylic acids at the current location, the surface of $TiO_2(110)$ is fully covered within a few minutes of exposure to air. The adsorbed carboxylates then bind to the undercoordinated surface Ti atoms blocking the sites usually considered as active in photocatalysis.[19]

In summary, we have shown that ultrapure liquid water without atmospheric impurities does not alter the structure of UHV-prepared $TiO_2(110)$-(1×1) surface except for hydroxylation at oxide vacancies. In contrast, exposure to liquid water in the presence of air results in the formation of an ordered (2×1) overlayer. Chemical analysis of the overlayer by XPS revealed adsorbed carboxylate, which was identified by infrared absorption spectroscopy and by analysis of STM images as a mixture of formate and acetate. To confirm the results described above, a sample was exposed to air and analyzed with XPS and STM in a distant location, Ithaca NY, USA. The data obtained there show the same spectroscopic signatures and very similar distribution of heights in the STM images of the (2×1) overlayer. The mixed formate/acetate overlayer is proposed to form by dissociative adsorption of atmospheric formic and acetic acids. These acids are present in the atmosphere in most parts of the World, which explains the observation of the same ordered overlayer by different groups.

Chapter 5

Interaction of TiO_2 rutile (011) with H_2O

This chapter is based on a publication, ref. [120]. The chapter, however, contains more experimental results and further information.

5.1 Introduction

The (011) surface is the second-lowest-energy termination of TiO_2 rutile. Together with the predominant (110) face it comprises a major fraction of the surface of equilibrium-shaped nanoparticles.[21] A distinct photocatalytic activity of the (011) surface has been reported, where the (011) face of rutile nanoparticles acted as an effective oxidation site, while the reduction occurred at the (110) face.[121]

When the (011) surface is prepared by sputtering and annealing in UHV, it forms a (2×1) reconstruction. The "brookite (001)-like" model of the (2×1) reconstructed surface was formulated on the basis of combined STM, surface X-ray diffraction (SXRD) experiments, and DFT calculations.[23,122] The bulk-truncated (1×1) surface of TiO_2(011) was not experimentally observed in UHV. However, an inversion of stability between the (1×1) and (2×1) terminations was predicted in a liquid water environment. According to DFT calculations,[123] the (2×1) reconstruction is not stable in liquid water, and the bulk-terminated (1×1) surface should be observed. Structure models of both, the (1×1) and (2×1) surfaces are shown in Fig. 5.1.

The restructuring between the (1×1) and (2×1) is achieved by rearranging the atoms, without long-distance mass transport (the reconstruction pathway was cal-

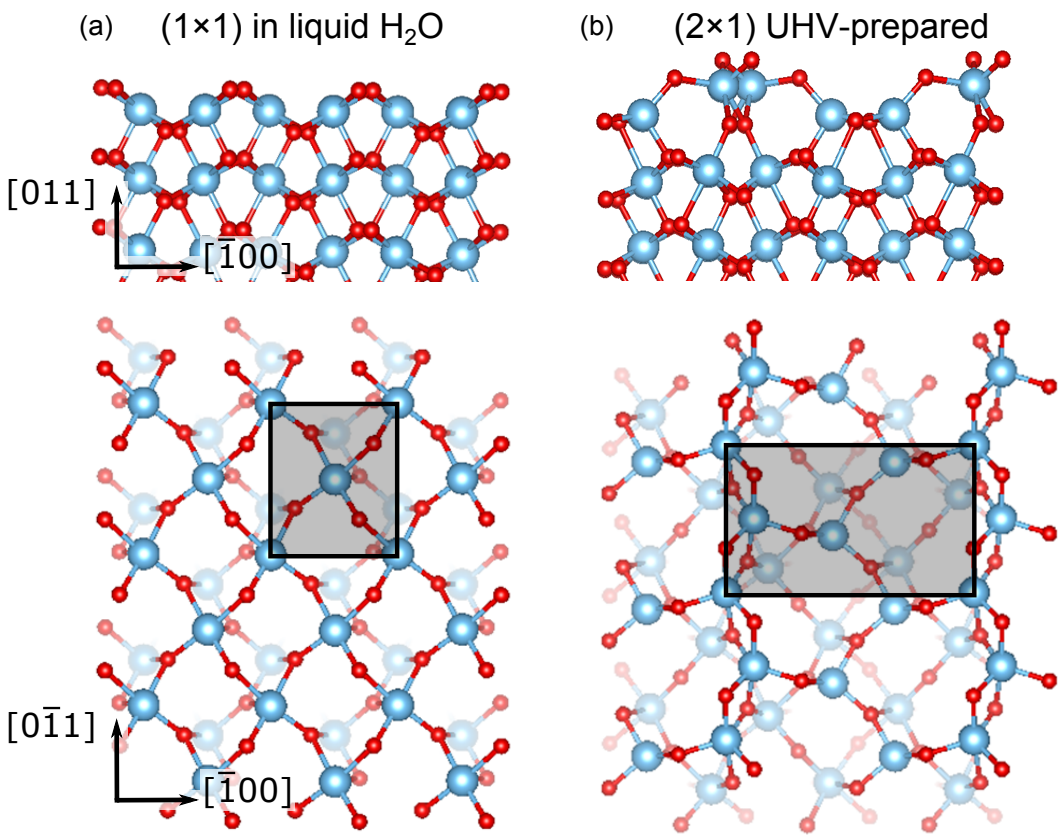

Figure 5.1 | Structural models of rutile TiO_2(011). (a) Bulk-terminated (1×1) surface, **(b)** (2×1) reconstruction (section and top views). Oxygen atoms are red, titanium blue. The (1×1) and (2×1) surface unit cells are indicated by black rectangles in the top-views. Atomic coordinates were provided by Ulrich Aschauer.

culated in ref. [123]). The predicted lifting of the (2×1) reconstruction induced by liquid water has not been reported upon dosing gas-phase H_2O in UHV.[124,125] At room temperature, gas-phase water was shown to adsorb dissociatively only at oxygen vacancies. Cooling of the sample to cryogenic temperatures resulted in the one-dimensional growth of water chains along the rows of the reconstructed surface. However, the surface itself was not affected by adsorbed water and retained its (2×1) reconstruction.

Here, we addressed this apparent pressure gap by dosing clean liquid water on a TiO_2(011)-(2×1) surface prepared in UHV. Chronologically, these experiments were done in the transfer chamber vented with purified argon before the water drop apparatus was designed. As described in the following, we experimentally confirmed the deconstruction of the (2×1) surface in liquid water as predicted by DFT calculations.[123] Additionally, we found that dissociated water binds to the unreconstructed

(1×1) surface, forming a (2×1) overlayer with two dissociated water molecules per (2×1) unit cell persistent in UHV at room temperature.

5.2 Experimental results - liquid H_2O

A TiO_2 rutile (011) sample (MTI Corp., top polished) was mounted on a molybdenum sample plate and prepared in the main UHV chamber by cycles of Ar^+ sputtering (1 kV, 0.6 μA/cm^2, 20 min) and annealing (680°C, 20 min). An STM image of the (2×1) reconstructed surface after such a preparation is shown in Fig. 5.2a. The alternating bright and dark rows running along the $[01\bar{1}]$ direction correspond to the ridges and valleys of the (2×1) reconstruction, respectively (see Fig. 5.1b). The bright features on the ridges are attributed to hydroxyl groups formed by dissociation of residual water in the UHV chamber at oxygen vacancies induced by the sample preparation. The STM image in Fig. 5.2a was recorded ca. 7 h after preparation, thus a relatively high density of the adsorbed OH was observed. In the experiment with liquid H_2O exposure (described below), the characterization of the clean surface with STM was performed only briefly, to save time and to minimize the exposure of the sample to the residual vacuum. The contrast in STM of the TiO_2(011)-(2×1) surface was found to strongly depend on the tunneling conditions.[122,126] The high-resolution inset in Fig. 5.2a displays the undulating rows and the appearance is well reproduced in the simulated STM image overlaid on top of the structure model in Fig. 5.2d. (The STM simulation was performed by Ulrich Aschauer.) The symmetry in reciprocal space is shown in the fast Fourier transform (FFT) in Fig. 5.1b and the LEED pattern in Fig. 5.1c. The expected (2×1) reciprocal pattern was observed in both, FFT and LEED. The $(0, 2n-1)$ spots where n is an integer are missing due to the glide plane symmetry of the lattice. Fourier transforms were obtained from distortion-corrected[127] STM images. The UVH-prepared surface was also characterized by XPS and LEIS before the exposure to liquid water (both shown below).

5.2.1 Structure after liquid H_2O exposure

The UHV prepared (2×1) surface was exposed to liquid water according to the procedure described in chapter 2, section 2.2.1. After evacuation with a cryo-sorption pump and a turbomolecular pump, the sample was transferred back to the main UHV

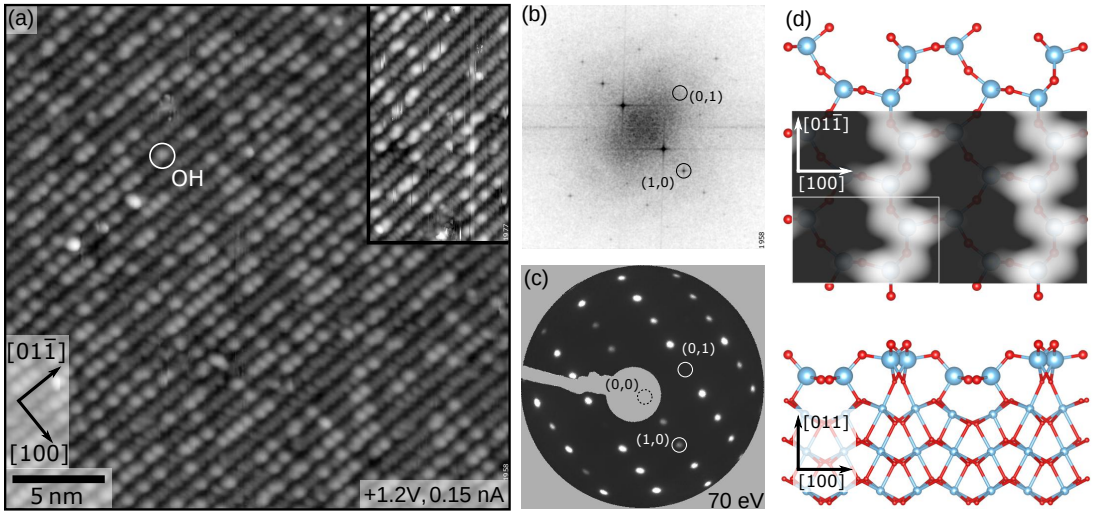

Figure 5.2 | UHV-prepared TiO_2(011)-(2×1) surface. **(a)** STM image with a higher resolution inset, **(b)** FFT of the STM image and **(c)** LEED. **(d)** Simulated STM image of the (2×1) reconstruction shown together with the computed structure (top and section views). The $(0, 2n-1)$ spots are missing in the FFT and LEED due to the glide-plane symmetry of the reconstructed surface.

chamber and analyzed with STM, XPS, LEIS, and LEED, in this order to minimize possible damage by electron or ion beams. The STM image in Fig. 5.3a clearly shows a change of the structure upon exposure to liquid water. Instead of the original (2×1) reconstruction, an ordered structure with an apparent "c(2×1)" symmetry with respect to the bulk-terminated (1×1) was observed. This quasi-hexagonal arrangement can be seen as rows of the periodic protrusion in the (1×1) symmetry, but the neighboring rows are shifted by half the unit cell along the row in the [01$\bar{1}$] direction. The pattern in the FFT of the STM image (Fig. 5.3b) shows such a "c(2×1)" reciprocal lattice. To facilitate the analysis of the structure, individual protrusions in the STM image in Fig. 5.3a were localized using a feature recognition procedure. The positions of the protrusions were then plotted as a 2D image. This way, an artificial image was created with the same structure as the STM image in Fig. 5.3a. The enhanced reciprocal pattern is shown in the FFT of the positions of the protrusions in Fig. 5.3c. Here, half of the (2×1) reciprocal spots are extinct. The extinctions occur at spots with indices (h,k), that satisfy the condition:

$$h + \frac{1}{2}k = n + \frac{1}{2}, \tag{5.1}$$

where n is an integer. Equation 5.1 describes extinctions alternatingly at integral

and fractional order spots as observed in FFT.

Interestingly, the symmetry observed in LEED is different than in the FFT of the STM image. The LEED pattern (Fig. 5.3d.) shows all spots of the (2×1) pattern with some of them split into two. Here, the sample was not well-aligned with the LEED screen due to the mechanical constraints of the manipulator. Therefore the (0,0) spot is not in the center of the pattern. As a result of the non-perpendicular incidence of the electron beam, the glide-plane symmetry is broken and weak (0,2n−1) spots are visible. The elongation and splitting of the fractional order spots in FFT and LEED are due to the presence of translational antiphase domains as observed with STM. Two neighboring domains are shifted with respect to each other by half the unit cell along the domain boundary. Domain boundaries, imaged as bright rows, are marked with yellow lines in Fig. 5.3a. Some of the half-order spots, *e.g.*, the (1/2, 1) spot, do not show a clear splitting in LEED (Fig. 5.3d) at the particular electron beam energy of 70 eV. At different energies, however, the same spot is visibly split, as shown at 50 eV in Fig. 5.3d. The structure of TiO_2(011) after exposure to liquid water is further discussed in section 5.4.

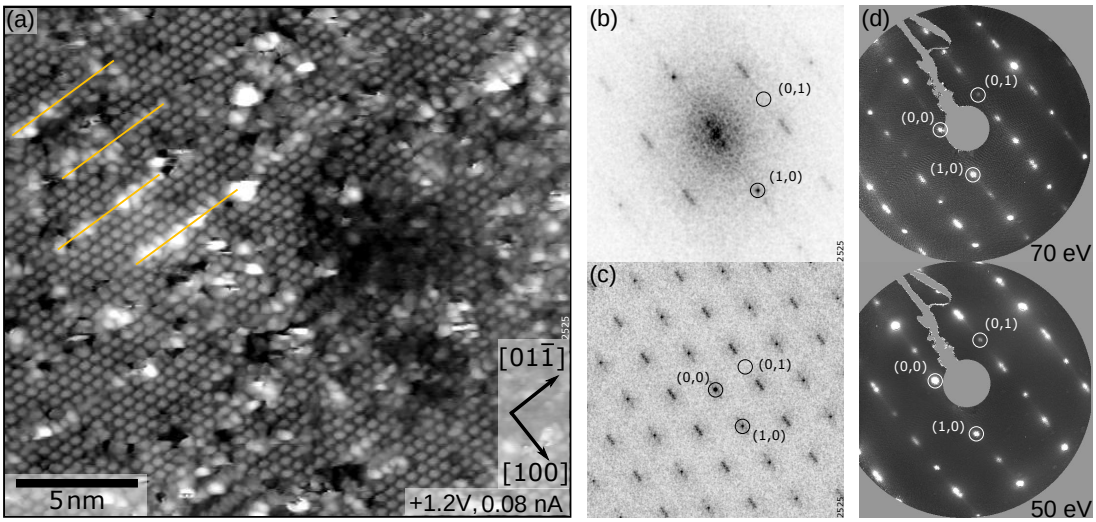

Figure 5.3 | TiO_2(011) surface after exposure to liquid H_2O. (a) STM image with antiphase domain boundaries highlighted with yellow lines. **(b)** FFT of the STM image and **(c)** FFT of the positions of protrusions in the STM image. **(d)** LEED patterns at two different electron beam energies. Splitting of fractional-order spots in FFT and LEED is due to antiphase domains on the surface.

The (2×1) reconstruction was retained in small areas of the surface even after exposure to liquid H_2O. Such areas enable to analyze the connection of the original

(2×1) reconstruction to the new "c(2×1)" structure. As apparent from the STM image in Fig. 5.4, the rows of the "c(2×1)" structure are aligned with the ridges and valleys of the (2×1) reconstruction. The dark depression between the rows of the "c(2×1)" structure are in line with the shoulders of the (2×1) reconstruction.

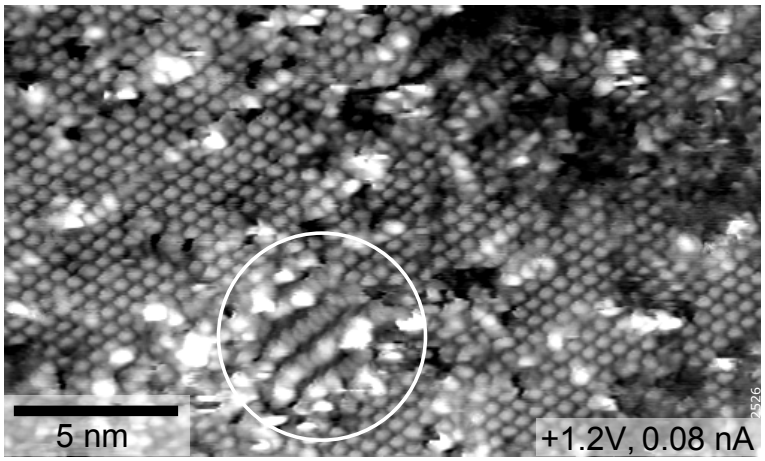

Figure 5.4 | Small area of (2×1) reconstruction preserved after exposure to liquid H_2O. The ridges and valleys of the original (2×1) reconstruction are aligned with the rows of the "c(2×1)" restructured surface. The (2×1) reconstructed area is marked with a circle.

5.2.2 Surface spectroscopy

The crystal was analyzed with XPS and LEIS before and after the exposure to liquid water to confirm that the observed restructuring is not due to impurities. Detailed XPS spectra of Ti*2p*, O*1s* and C*1s* transitions are shown in Fig. 5.5. The Ti*2p* spectrum (Fig. 5.5a) after water exposure is almost identical to that of the UHV-prepared surface, except for a small deviation at ~ 457 eV. The decrease after contact with liquid water is attributed to oxidation of a Ti^{x+}, $x < 4$, defect species induced by UHV preparation, to Ti^{4+}. A high-binding-energy shoulder was observed in the O*1s* spectrum (Fig. 5.5b) due to a peak of dissociated water (OH) at 532.1 eV. The OH signal, as well as the attenuation of the lattice oxygen peak, is more prominent in grazing emission (60°), which confirms that hydroxyl groups are located at the surface. Only a minor increase of the adventitious carbon signal at 284.3 eV was observed in the C*1s* region in grazing emission (Fig. 5.5d). The smaller peak at 288.3 eV is attributed to carboxylate (see chapter 4). Essentially no carbonaceous contamination was detected in normal emission (Fig. 5.5c). Both C*1s* spectra contain reference data of saturation

coverage (0.5 ML) of formate ($HCOO^-$) deposited on TiO_2(110). The C*1s* spectra in Fig. 5.5c, d were obtained without biasing the sample and therefore contain the artificial carbon signal from the analyzer (see chapter 2, Fig. 2.7). The small increase of adventitious and carboxylic carbon is attributed to atmospheric adsorption due to backstreaming of air in an the argon flow. By comparison to the C*1s* spectrum of formate on TiO_2(110), the overall carbonaceous contamination was estimated below 0.1 ML. No other impurities were detected by XPS as shown in the overview spectrum in Fig. 5.6.

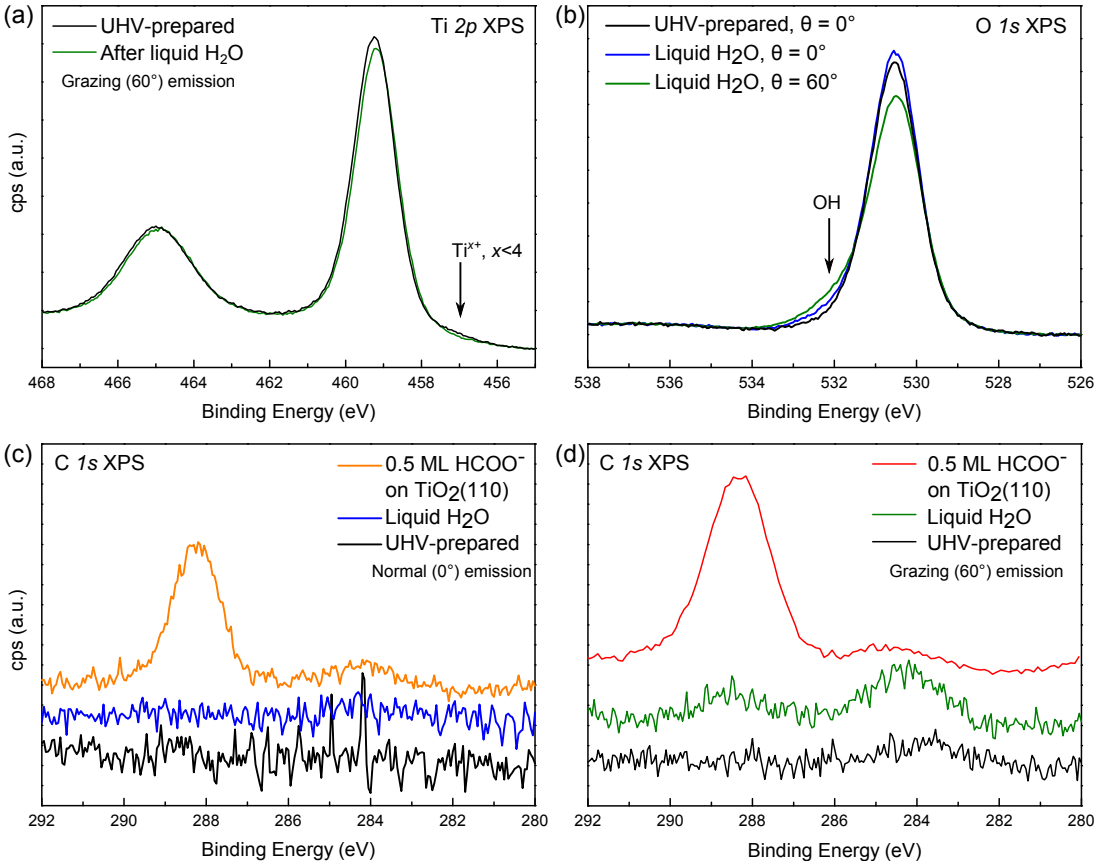

Figure 5.5 | Detailed XPS of UHV-prepared TiO_2(011) and after contact with liquid H_2O. Dissociated water on the surface is observed as the high-binding-energy shoulder of the O*1s* peak in **(b)**. The lower panels **(c,d)** contain reference data of a saturation coverage (here defined as 0.5 ML) of formate on TiO_2(110) at the corresponding emission angles. A quantitative comparison yields less than 0.1 ML of total carbonaceous contamination following the exposure to liquid H_2O. All XPS data were acquired with Mg Kα X-ray radiation at emission angles indicated in the legends. All spectra were normalized to the low-binding-energy background, and the C*1s* spectra in **(c)** and **(d)** are vertically offset for clarity.

A pseudo-hexagonal structure, somewhat similar to the one observed in Fig. 5.3a

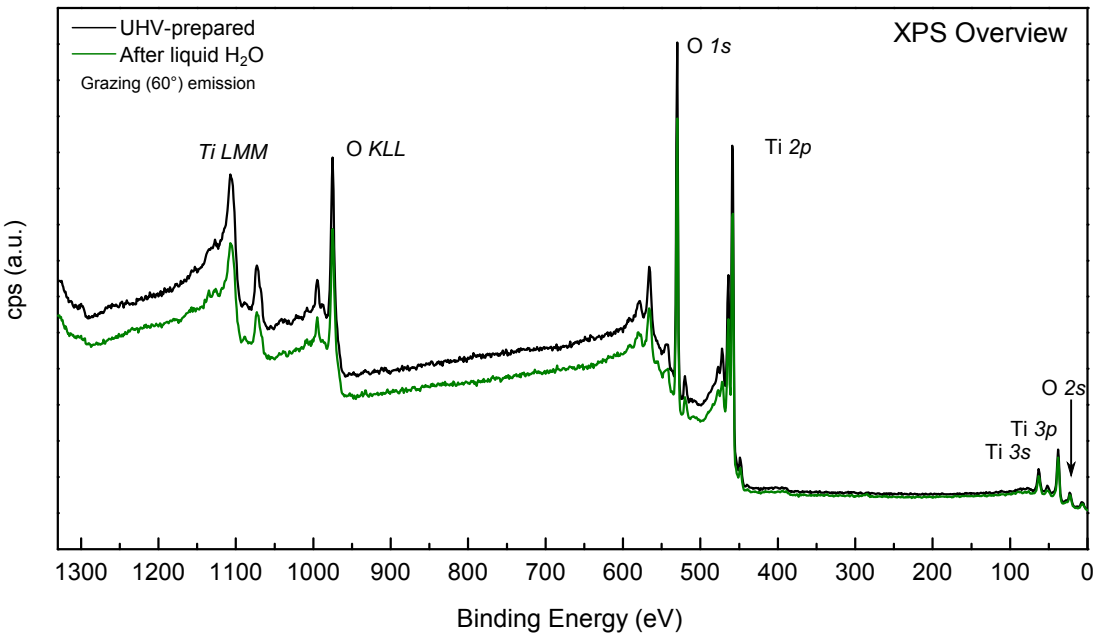

Figure 5.6 | Overview XPS of UHV-prepared TiO_2(011) and after contact with liquid H_2O. No change in the spectra was observed except for those shown in detail in Fig. 5.5, and an overall decrease in the background signal caused by the hydroxyl overlayer. Both spectra were acquired with Al Kα X-ray radiation, and photoelectrons were collected at grazing emission (60°from the surface normal).

has been previously observed on the TiO_2(011) surface and has been reported in refs. [24, 75, 128–131]. The structure was attributed to the segregation of bulk impurities (Ca in ref. [24]) to the surface, or an intentionally-prepared mixed-oxide monolayer by deposition of metals (Fe, Cr, Ni, V and later also Cr and Cu) in oxidizing atmosphere.[129,131] In order to exclude the presence of such impurities, we have analyzed the surface composition with LEIS and XPS (spectra shown in Fig. 5.7 and 5.6, respectively). Only oxygen (mass 16) and titanium (mass 48) were detected on the UHV-prepared surface. No foreign elements emerged in the LEIS spectra upon the liquid H_2O exposure. In experiments with a different TiO_2(011) crystal we observed segregation of magnesium from the bulk to the surface. In this case, the impurity was reliably detected with both, LEIS and XPS. The observed formation of a mixed oxide due to Mg segregation is discussed in more detail in section 5.6.

As no impurities were detected with both spectroscopic methods, the "c(2×1)" layer observed in STM is assigned to dissociated water (OH) on the TiO_2(011) surface.

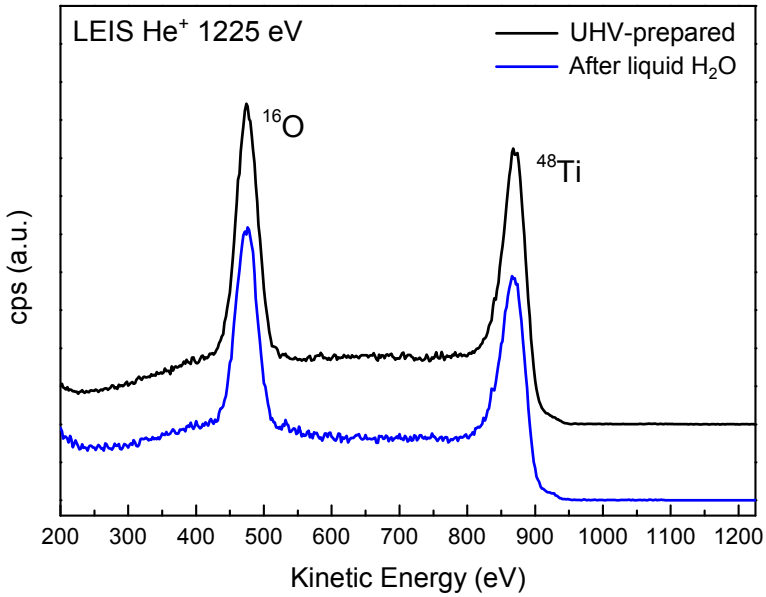

Figure 5.7 | LEIS of UHV-prepared TiO_2(011) and after contact with liquid H_2O. No impurities were detected on the UHV-prepared surface as well as after exposure to liquid water. The spectra are vertically offset for clarity.

5.3 Computational results - dissociated water on TiO_2(011)

Having established that the observed overlayer is composed of dissociated water, calculations of various arrangements of OH groups on the surface were performed. Initially, we (incorrectly) interpreted the STM and LEED data (Fig. 5.3) as the retention of the (2×1) reconstruction (due to the observed 2×1 symmetry in LEED), and a "c(2×1)" overlayer formed on top (as observed with STM). Based on this assumption, a number of different arrangements of two dissociated water molecules per (2×1) unit cell of the reconstructed surface were tested computationally. However, none of these matched the structure and symmetry experimentally observed with STM. Later, we realized, that the (2×1) reconstruction with its alternating ridges and valleys does not provide a sufficiently high density of equivalent adsorption sites to accommodate two dissociated water molecules per (2×1) unit cell. In contrast, the right adsorption symmetry and density can be obtained on the unreconstructed (1×1) surface. The neighboring rows of the "c(2×1)" structure in Fig. 5.3a are imaged as equivalent, as demonstrated by the extinctions in the FFT of the STM image (Fig. 5.3b). Therefore, the adsorbates have to reside at symmetrically equivalent sites. A total of 18 config-

urations of two dissociated water molecules per (2×1) unit cell were computationally tested on the unreconstructed surface. Fig. 5.8a shows the surface sites considered for adsorption of OH (orange labels) and H (white labels). See, ref. [120] for the table of relative total energies of different combinations of adsorption sites. The two lowest-energy configurations are shown in Fig. 5.8b, c. The structure in Fig. 5.8c is 0.05 eV per (2×1) unit cell lower in energy than the structure in Fig. 5.8b, due to the additional hydrogen bond per hydroxyl group in structure (c). However, the lack of this additional H bond in structure (b) increases its degrees of freedom and thus the structure in Fig. 5.8b is expected to be entropically more favorable at room temperature. Dissociative adsorption is favored over molecular adsorption by 0.11 eV per water molecule. All calculations and STM simulations were performed by Ulrich Aschauer and Annabella Selloni. Computational details are described in ref. [120].

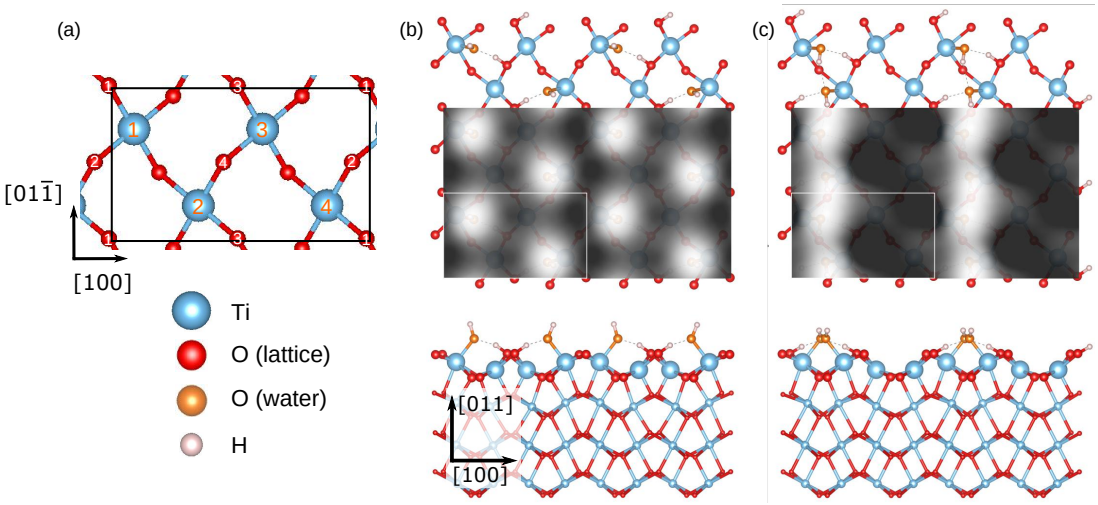

Figure 5.8 | Calculated structures of hydroxylated TiO_2(011). (a) Surface sites considered for dissociative adsorption of two water molecules; OH sites (orange labels), H sites (white labels). Top views, section views and simulated STM images of the two lowest-energy configurations: **(b)** two water molecules dissociatively adsorbed in neighboring trenches of the (1×1) surface, and **(c)** two water molecules dissociatively adsorbed in the same trench of the (1×1) surface. The black and white rectangles show the (2×1) unit cell.

5.4 Discussion - liquid H_2O

The structure observed by STM after exposure to liquid water (Fig. 5.3a) resembles the simulated STM image in Fig. 5.8b. Here, the hydroxyl groups are bound to five-

fold coordinated Ti atoms on neighboring trenches of the unreconstructed surface. The OH overlayer has a (2×1) symmetry and a glide reflection along the [01$\bar{1}$] direction. According to 2D symmetry groups, the superstructure can be classified as *pg*.[132]

Different symmetry in STM and LEED

While STM probes only the topmost atomic layer, a LEED pattern is formed by interference from the first few layers. According to the calculated structure (Fig. 5.8b), dissociated water forms a (2×1) overlayer on top of the unreconstructed (1×1) TiO_2(011) surface. The expected reciprocal pattern should, therefore, exhibit a (2×1) symmetry, in agreement with the experimental LEED observation in Fig. 5.3d.

The rows of the OH groups along the [01$\bar{1}$] direction in the calculated model in Fig. 5.8b are not exactly equidistant, thus the structure exhibits (2×1) symmetry. However, the rows appear almost equidistant in the simulated STM image in Fig. 5.8b. Although the OH groups in neighboring trenches are pointing in different directions, they are at the same height and therefore not distinguished by STM (Fig. 5.3a). The (2×1) structure is therefore imaged with an apparent "c(2×1)" symmetry. This apparent higher symmetry is demonstrated by the extinctions of half of the FFT spots in Fig. 5.3b, c and by a smaller, diamond-shape unit cell.

Splitting of spots in LEED and FFT

Translational antiphase domains were observed with STM within the OH overlayer in Fig. 5.3a. The domains are separated by boundaries, imaged as brighter rows along the [01$\bar{1}$] direction. The calculated low-energy structure in Fig. 5.8c might be the local structure at the domain boundary. Together with the predominant pseudo-hexagonal structure (Fig. 5.8b), these could coexist on the surface. Given that the domain boundaries have the anticipated structure (Fig. 5.8c), they could be classified as heavy domain walls,[5,133] as the local density of adsorbates (here OH) is higher than their density within the domains. Smaller domains result in a higher density of domain boundaries and increase the overall coverage of hydroxyls. We observed a slight variation of the domain size in our experiments, typically five to seven rows in width.

In Fig. 5.3a, the typical domain size is ∼ 23 Å (5 rows), well below the coherence

length of the electron beam (typically ~ 100 Å).[134] Individual domains then diffract coherently, and as the neighboring domains are out of phase, characteristic effects, such as splitting of some beams can be observed in the diffraction pattern.[135] Here, the splitting of LEED spots occurs perpendicular to the boundaries due to the parallel orientation and regular spacing of the antiphase boundaries on the surface.

Qualitatively, the splitting of the spots can be explained by the example of two subdomains with identical dimensions.[135] The interference function of such configuration is modulated by a function, which is determined by the phase shift between electrons diffracted by the neighboring domains. The relation between translational antiphase domains can be described by a vector connecting the two domains across the domain boundary. The connecting vector **d** can be expressed as a linear combination of lattice base vectors $\mathbf{a_1}$, $\mathbf{a_2}$ of the (1×1) surface:

$$\mathbf{d} = d_1\mathbf{a_1} + d_2\mathbf{a_2}\,, \tag{5.2}$$

where d_1, d_2 are base components of the vector **d**. Splitting of a diffraction beam occurs, when the minimum of the modulation function coincides with a maximum (bright spot) of the perfect surface. The condition is fulfilled when:[135]

$$hd_1 + kd_2 = \frac{1}{2}(2n + 1)\,, \tag{5.3}$$

where h, k are indices of diffracted beams and n is an integer. A model of the two translational antiphase domains of the (2×1) OH overlayer on the unreconstructed (1×1) surface is shown in Fig. 5.9. The domains consist of the calculated structure in Fig. 5.8b and are separated by a domain boundary (structure in Fig. 5.8c). The true (2×1) unit cells on each side of the domain boundary are indicated by a black rectangles in Fig. 5.9a. The unit cells across the domain boundary (highlighted with a yellow stripe) are connected with a vector $\mathbf{d} = 3\mathbf{a_1}$. Substitution to eq. 5.3 yields $6h = 2n + 1$, which is satisfied only for fractional values of index h (half-order spots). In accord with experimentally observed LEED pattern (Fig. 5.3d), the fractional-order spots are split, while the integral spots are single. This result further disproves our early hypothesis, that "c(2×1)" OH overlayer formed on top of the (2×1) reconstructed surface. On the (2×1) reconstructed surface, domain boundaries were observed only rarely, therefore no splitting would be detected at half-order spots.

The two dissociated water molecules within (2×1) unit cell (Fig. 5.8b) are not dis-

criminated by STM, although they are oriented differently. This apparent "c(2×1)" structure leads to a different connecting vector between the diamond-shaped unit cells (Fig. 5.9b). The connecting vector between two nearest "c(2×1)" unit cells across the boundary can be expressed as $\mathbf{d'}=2\mathbf{a_1} + 1/2\mathbf{a_2}$. Substitution to Eq. 5.3 yields $4h + k = 2n + 1$, therefore only spots with an odd value of index k are split, in agreement with the experimentally observed splitting of FFT spots in Fig. 5.3b, c. In fact, all FFT spots with odd k-index are the spots with a fractional h-index. Both descriptions thus identify splitting of fractional-order spots due to antiphase domains within the OH overlayer.

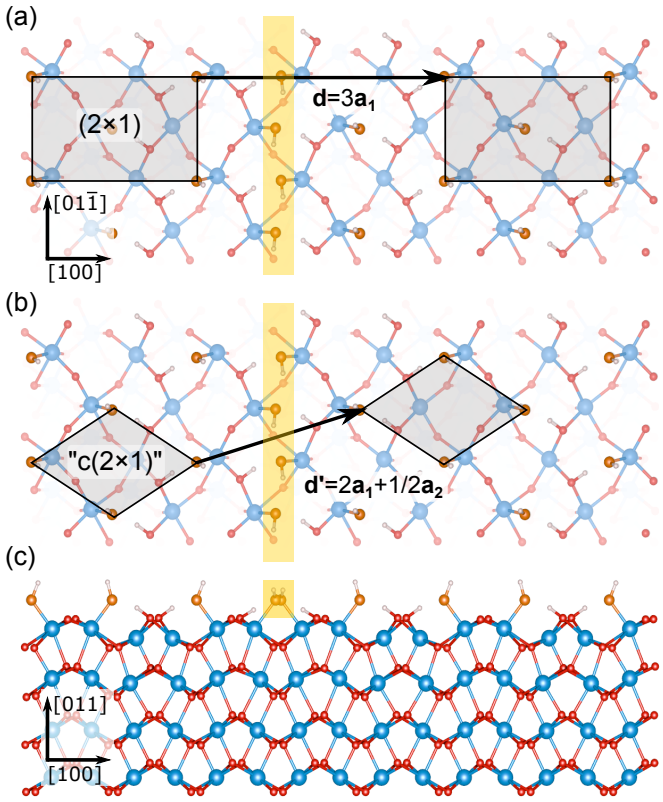

Figure 5.9|Model of antiphase domains within OH overlayer on TiO_2(011)-(1×1). **(a)** Real (2×1) unit cells are highlighted, connected by vector **d** across the domain boundary. **(b)** Apparent "c(2×1)" unit cells highlighted, as seen by STM, are connected by a different vector **d'** **(c)** section view.

LEED patterns can be qualitatively simulated by diffraction of laser light on a grating with holes imitating the expected structure. Diffraction of (2×1) translational antiphase domains optically simulated in ref. [136] matches the LEED pattern observed in Fig. 5.3d.

5.5 Low-temperature adsorption of H_2O

To search for possible similarities in the adsorption structure of water, we dosed gas-phase H_2O in the UHV chamber while the sample was at low temperature. The experiments were conducted in the LT-STM chamber (described in chapter 2, section 2.2.2) because that system provides cooling of the manipulator with liquid nitrogen. After the clean (2×1) reconstructed surface was prepared by cycles of sputtering and annealing, the sample was cooled to 110 K, and 10 L of H_2O dosed into the chamber. Such a high dose leads to the growth of ice multilayers as confirmed by an O *1s* peak of molecular H_2O observed by XPS (Fig. 5.10). As expected, heating of the sample to 170 K, above the desorption temperature of ice multilayers, resulted in the hydroxylated surface. The O *1s* spectrum taken at 170 K shows the absence of a molecular H_2O peak but exhibits a high-binding-energy shoulder due to OH at the surface. The Ti *2p* transition remains unaffected, except for an attenuation due to ice multilayers (blue curve). A barely visible deviation from a straight line was observed in the C *1s* region upon dosing water at 110 K. No carbon was detected after desorption of multilayers (at 170 K). An overview XPS spectrum (not shown) did not reveal any foreign elements.

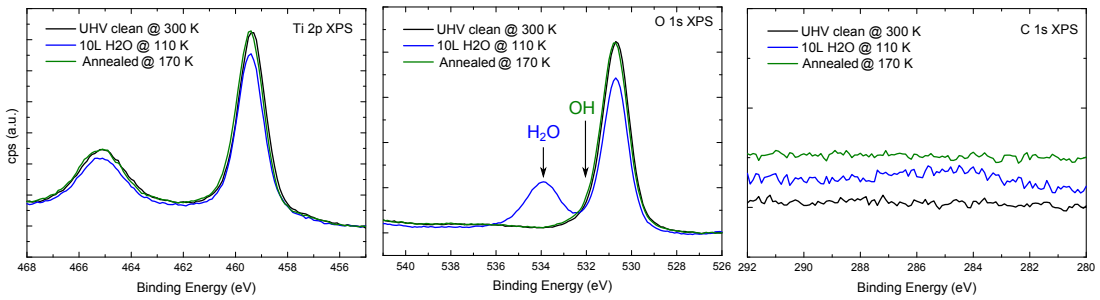

Figure 5.10 | XPS of adsorbed H_2O on TiO_2(011)-(2×1) at low temperature. The spectra were acquired with Mg Kα X-rays, at normal emission with a pass energy of 20 eV. All spectra were normalized to the low-binding-energy background, and the C *1s* spectra are vertically offset for clarity.

The surface was characterized with STM after dosing 10 L of H_2O at 110 K. Steps of the TiO_2(011) surface were observed with only a weak (2×1) periodicity within the terraces, likely due to amorphous ice multilayers (images not shown). After desorption of ice multilayers by heating to 170 K, STM shows the rows of the (2×1) reconstruction with a high density of OH adsorbates on top of the (2×1) ridges, see Fig. 5.11a. The detailed STM image in Fig. 5.11b contains areas that expose the un-

derlying (2×1) reconstruction, where the OH was locally removed by the STM tip. The FFT of the STM image (Fig. 5.11c) confirms the (2×1) symmetry.

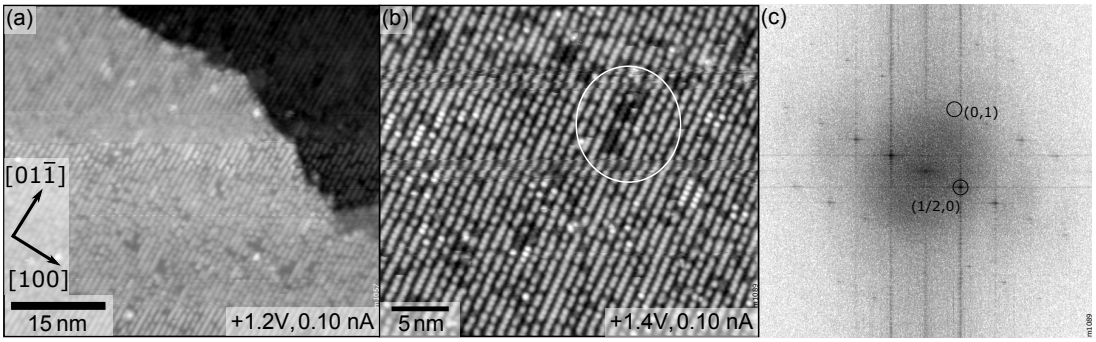

Figure 5.11 | STM of H_2O adsorbed on TiO_2(011)-(2×1) at low temperature. STM images were taken at 78 K after heating the sample to 170 K to desorb ice multilayers. Exposed parts of the surface, such as the one within the white circle, show the (2×1) reconstruction.

On the UHV-prepared surface, the expected (2×1) LEED pattern was detected, the same as in Fig. 5.2c. After dosing H_2O at 110 K, the same LEED pattern was observed, although substantially attenuated by the (amorphous) ice multilayers on the surface (see Fig. 5.12). After heating to 170 K, bright spots with the (2×1) symmetry were detected again. The broadening of LEED spots is attributed to an experimental problem, perhaps defocused electron beam.

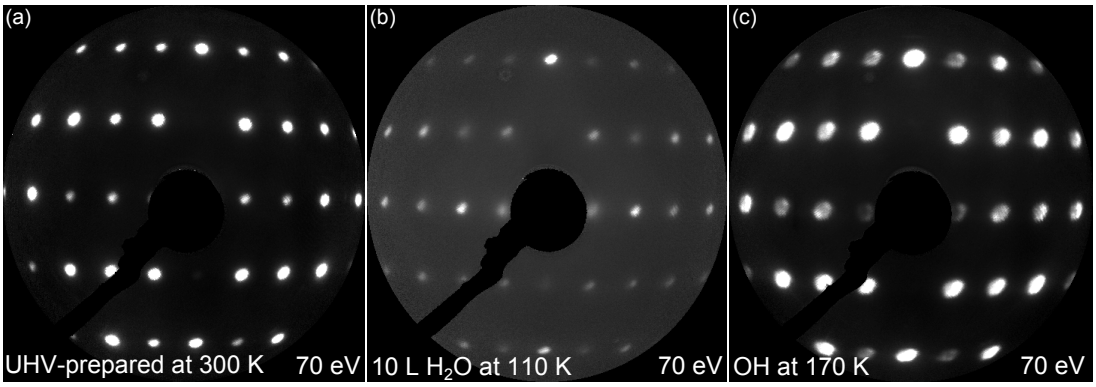

Figure 5.12 | LEED of adsorbed H_2O on TiO_2(011)-(2×1) at low temperature. (a) The UHV prepared surface exhibits (2×1) symmetry. **(b)** The same pattern with reduced intensity due to ice multilayers after dosing H_2O at 110 K. **(c)** (2×1) pattern with after desorption of multilayers at 170 K. The spot broadening in **(c)** is probably due to an experimental problem.

The adsorption of gas-phase H_2O at low temperature did not affect the (2×1) reconstruction, unlike the exposure to liquid water. We rationalize that at low temper-

ature, compact layers of H_2O can be formed, but thermal activation energy is needed to change the reconstruction, dissociate the water molecules, and create an ordered structure.

5.6 Segregation of impurities on rutile TiO_2(011)

A quasi-hexagonal structure has been observed on another TiO_2(011) crystal after sample preparation by sputtering and annealing in UHV. These results are included in this chapter, due to a similarity of the quasi-hexagonal structure (STM in Fig. 5.13) to the apparent "c(2×1)" structure after exposure to liquid water. Based on LEIS and XPS measurements (see below), the quasi-hexagonal structure was associated with the segregation of magnesium impurities from the crystal bulk. A similar structure was observed on TiO_2(011) in refs. [24, 75, 128–131], where such a structure formed by segregation of impurities or was purposely prepared by deposition of foreign metals in an oxidizing atmosphere. We thus assign the observed quasi-hexagonal structure as a mixed titanium-magnesium oxide monolayer, formed by segregation of Mg impurities from the bulk to the surface at elevated temperatures during annealing. The quasi-hexagonal mixed phase was shown to co-exist with the (2×1) reconstruction. The mixed oxide formed compact terraces with a fractional step-height on the (2×1) reconstructed surface. The atomic rows along the $[01\bar{1}]$ direction within the mixed phase are twice as dense as the ridges of the (2×1) reconstruction (Fig. 5.13a). However, the rows within the quasi-hexagonal phase are not exactly equidistant, resulting in a (2×1) symmetry as observed in FFT (Fig. 5.13c) and LEED (Fig. 5.14).

The LEED pattern in Fig. 5.14 was acquired on a (2×1) reconstructed surface, containing regions of mixed oxide. As the symmetry of both phases is (2×1), the LEED pattern cannot be distinguished from the pattern of solely (2×1) reconstructed surface (Fig. 5.2c). The formation of domains was not observed within the Mg impurity-induced quasi-hexagonal structure. Therefore, no spot splitting was observed, unlike in the LEED pattern of the (2×1) OH overlayer on (1×1) unreconstructed surface (Fig. 5.3d). The magnesium impurities were detected by spectroscopic techniques. The segregation of Mg to the surface was directly observed with temperature-dependent LEIS and XPS measurements. Fig. 5.15 shows a LEIS spectrum of a sputtered sample at room temperature (black curve). Here, no elements apart from titanium (mass 48) and oxygen (mass 16) were detected. The sputtered surface is depleted from

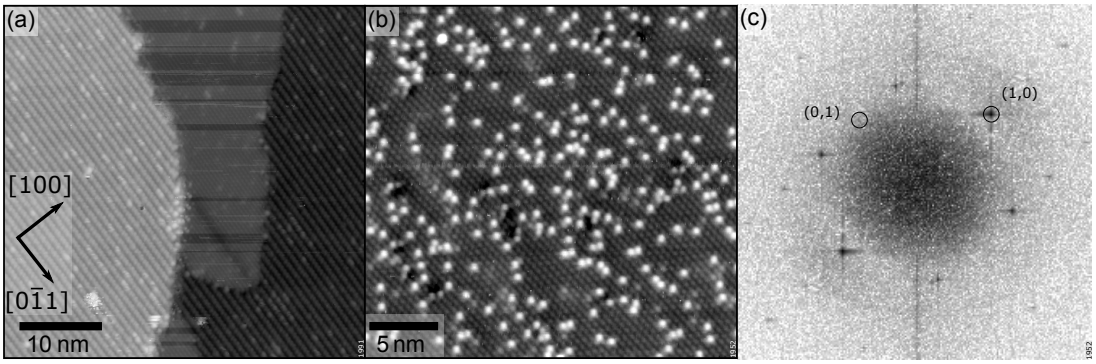

Figure 5.13 | STM of TiO_2(011)-(2×1) containing fractions of a mixed Ti-Mg oxide. (a) Larger-area STM image containing both the (2×1) reconstructed surface and the quasi-hexagonal mixed phased on the middle terrace. **(b)** High-resolution STM image of the quasi-hexagonal mixed phase, brighter spots are attributed to hydroxyl groups from the residual water in the UHV chamber. **(c)** FFT of the STM image in **(b)** demonstrates a (2×1) symmetry of the quasi-hexagonal structure, *e.g.*, due to the presence of (1/2, 1) spots.

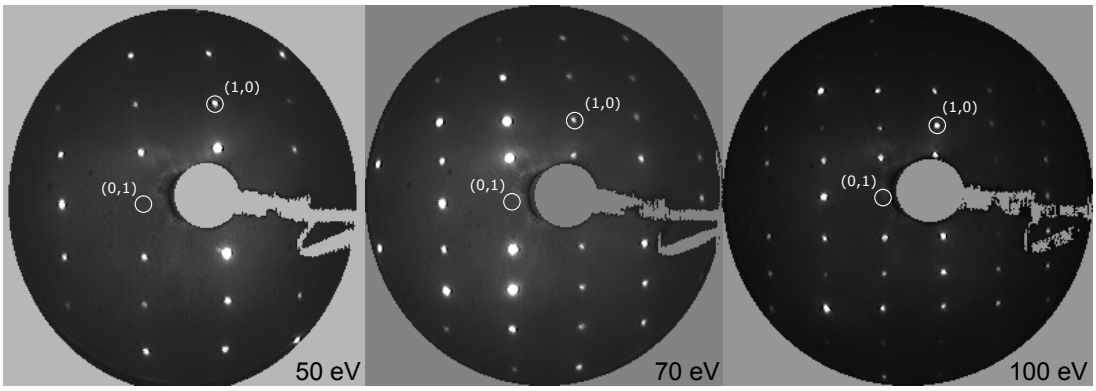

Figure 5.14 | LEED of rutile TiO_2(011)-(2×1) containing fractions of Mg mixed oxide. The (0, 2*n*-1) spots are extinct due to glide-plane symmetry. Splitting of the spots was not detected at any energies, consistent with STM measurements, where no domains were observed. Electron beam energies are indicated.

oxygen due to preferential sputtering. The sample was then slowly annealed while acquiring the LEIS spectra at increasing temperatures. At around 350°C, the O:Ti ratio increased and another peak corresponding to magnesium (mass 24) appeared (red curve in Fig. 5.15). Upon further annealing, the Mg peak vanished at ~ 500°C as Mg dissolved in bulk (dark-yellow curve in Fig. 5.15). No further changes were observed at higher temperatures (measured up to 700°C). During the cooling, the Mg segregated again at ~ 400°C and stayed on the surface during cooling to room temperature.

The segregation of magnesium observed by LEIS was confirmed by temperature-

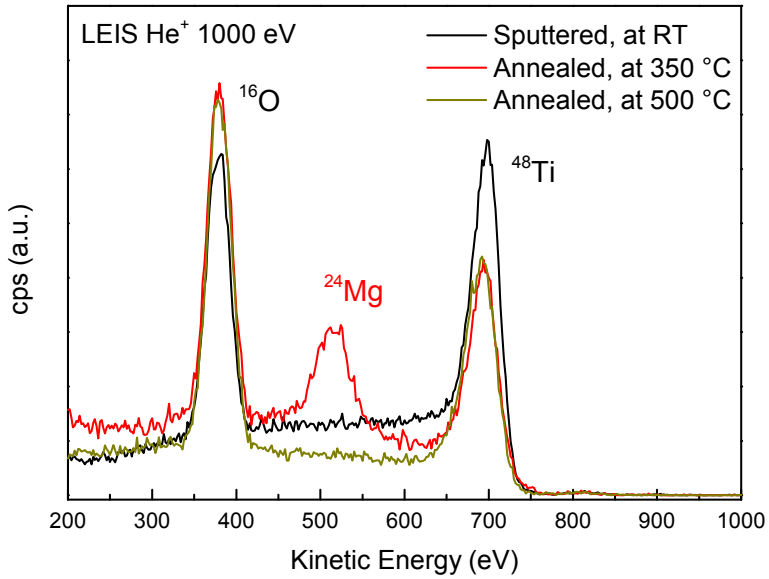

Figure 5.15 | Temperature-dependent LEIS measurement of Mg-contaminated TiO_2(011) sample. The stoichiometry of the sputtered surface is shifted towards titanium due to preferential sputtering of oxygen. The spectra were taken at the temperatures given in the legend and are plotted without processing.

dependent XPS measurements shown in Fig. 5.16. The Mg X-ray anode could not be used to identify the presence of magnesium on the surface. The measured binding energy of Mg*1s* is 1305.0 eV, thus higher than Mg Kα photon energy (1253.6 eV). The Mg *KLL* Auger peak can not be observed for the same reason, as the Mg Kα photon energy is insufficient for excitation of electron from the *K(1s)* level. The use of an Al X-ray anode allowed for reliable detection of magnesium.

The STM image in Fig. 5.17 was taken after annealing the Mg-contaminated sample to 300-350°C. The sample was previously annealed to 650°C without sputtering in between. Here, the quasi-hexagonal structure of mixed oxide is found in form of small, interconnected islands on the (2×1) reconstructed surface. We speculate that an intermediate annealing temperature (350 °C) leads to Mg segregation but is not sufficient to form compact terraces as shown in Fig. 5.13. The large, bright features located at the edges of the quasi-hexagonal islands might be aggregates of a magnesium compound, which did not yet incorporate into the oxide layer. The STM image was acquired after the sample was cooled to room temperature. The bright spots on both, the (2×1) reconstruction and the quasi-hexagonal mixed phase are attributed to hydroxyls from residual water in the chamber.

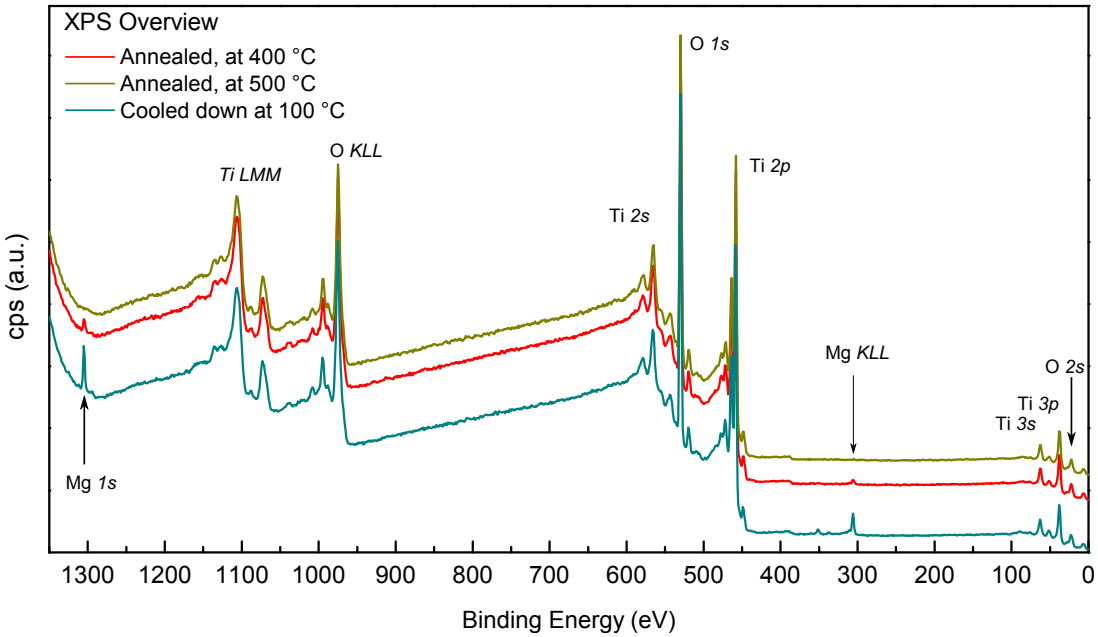

Figure 5.16 | Temperature-dependent XPS measurement of Mg-contaminated TiO_2(011) sample. The individual spectra were taken with the sample at the temperatures given in the legend. All spectra were acquired with Al Kα X-rays at normal emission and are vertically offset for clarity.

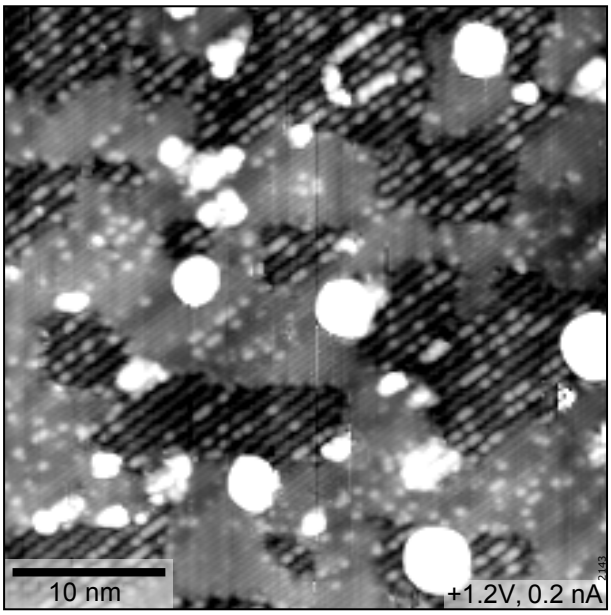

Figure 5.17 | STM of Mg-contaminated TiO_2(011) after annealing to 350°C. Interconnected islands of the quasi-hexagonal structure form on top of the (2×1) reconstructed surface. The image might capture an intermediate stage of mixed oxide monolayer formation.

5.7 Conclusion

To summarize, we have presented that the TiO_2(011)-(2×1) reconstruction is lifted upon contact with liquid H_2O, as predicted in ref. [123]. Additionally, we have shown that dissociated water remains on the unreconstructed (1×1) surface after evacuation, in the form of a (2×1) overlayer with two dissociated water molecules per (2×1) unit cell. Antiphase domain boundaries within the OH overlayer are responsible for the splitting of fractional-order spots in LEED and the FFT of STM images.

XPS and LEIS measurements excluded the possibility of impurity-induced restructuring and enabled assigning the ordered overlayer to dissociated water. In contrast, on another, contaminated crystal, magnesium impurities were reliably identified; this contamination lead to the formation of mixed-oxide monolayers with a similar quasi-hexagonal structure.

The exposure to liquid water was not reproduced by adsorption of gas-phase water in UHV at low temperature. Such an experiment resulted in fully hydroxylated ridges of the (2×1) reconstruction, but the reconstruction remained unaffected.

At room temperature, gas-phase water dosed in UHV adsorbs on surface defects and does not form compact layers under these low-pressure conditions. At low temperatures, dense water layers form, but the energy barrier for surface deconstruction and rearranging of the dissociated water cannot be overcome. In liquid water, both requirements are met, thus explaining its distinctly different behavior on TiO_2(011). The rutile TiO_2(011) is, therefore, an exemplary system, where the knowledge gained from studies in UHV cannot be simply extrapolated to real application conditions.

Chapter 6

Summary and outlook

In summary, this thesis reported on surface investigations of the two most stable terminations of rutile TiO_2, the (110) and (011) surfaces, when brought into contact with liquid water.

The (110) surface was shown to retain its bulk-terminated (1×1) structure when exposed to liquid water. Additionally, we clarified the chemical origin of the (2×1) ordered overlayer that readily forms at the surface of TiO_2(110) following exposure to air. The overlayer was attributed due to the adsorption of carboxylic acids. Although present at very low concentrations in the ambient atmosphere, these adsorb at the surface with high affinity, effectively displacing other adsorbates present at higher concentrations.

In order to separate the effect of liquid water from possible artifacts of exposure to air, a specialized apparatus was designed for dosing pure water under UHV-compatible conditions. Apart from showing that pure water leaves the (110) surface unaffected, we were able to use the apparatus for the controlled dosing of gases. However, no reaction of gases with liquid water forming these acids was observed, indicating adsorption of atmospheric carboxylic acids.

Our finding explained the formation of molecularly ordered monolayer following exposure to air, reported by several research groups, and provided additional insight into the self-cleaning properties of TiO_2. The fact that the undercoordinated Ti sites at the surface of TiO_2(110) are blocked by carboxylates in the ambient environment has important implications for photocatalysis, where these sites are often considered as active.

In contrast, the (011) surface of TiO_2 was found to lose its (2×1) reconstruction upon immersion in liquid water. In agreement with theoretical predictions, the sur-

face restructured into a bulk-terminated (1×1) configuration. Besides the predicted surface deconstruction, dissociated water was found to remain on the unreconstructed surface after evacuation in the form of a (2×1) overlayer with two dissociated water molecules per (2×1) unit cell. The restructuring was not reproduced in experiments with low-temperature adsorption of gas-phase water in UHV. The different results of these two experiments illustrate the need for surface-science studies closer to realistic conditions to enable the transfer of the knowledge into applications.

In retrospect, the (011) surface has demonstrated surprising inertness towards adsorption of carboxylic acids, as evidenced by spectroscopic techniques. Although it was treated identically to the (110) sample, only a minor increase of signal corresponding to carbonaceous impurities was detected. We speculate that the observed high affinity of the (110) surface towards the adsorption of carboxylic acids might be (at least partially) a consequence of the favorable distance (2.96 Å) between five-fold coordinated Ti surface atoms. On the unreconstructed (011)-(1×1) surface, the surface Ti sites are further apart (3.57 Å). On the (2×1)-reconstructed (011) surface, the five-fold coordinated Ti atoms are found at a similar distance (2.91 Å) as on the (110), however, they are bridged by protruding surface oxygen atoms. The bridging oxygen atoms might sterically hinder carboxylic acids from binding to surface Ti sites in bidentate configuration. On (110) surface the surface Ti sites are further from the protruding O_b sites, thus easily accessible. The same argument was used to explain the different adsorption behavior of gas-phase acetic acid on (110) and (011) surfaces in ref. [128]. Unlike the (110) surface, where acetate forms a homogeneous and compact layer upon dissociative adsorption in bidentate geometry, a monodentate form was shown to be the dominant adsorption configuration on the reconstructed (011) surface. Adsorption at room temperature was initiated at surface defects and later at higher exposures propagated in the form of linear clusters. As acetate binds to the surface with its carboxylic functional group, a similar adsorption mechanism is expected with formate and other carboxylates. The stable bidentate adsorption of atmospheric carboxylic acids occurring on the (110) surface is prohibited on the (011) surface due to steric hindrance owing to the different structure of these two surfaces.

Potentially interesting would be to study the interaction of liquid water with anatase TiO_2. Anatase is considered the more active polymorph of TiO_2 and thus relevant for photacatalysis.[137] Anatase is the major constituent (typically 70-90%)[138] of commonly used TiO_2 powder catalyst Degussa P25, the rest is rutile. While larger TiO_2

crystals are usually found in thermodynamically stable rutile phase, anatase is stable in the form of nanoparticles, due to the low free energy of its (101) facets.[9,139] The small size of synthetic anatase crystals has been prohibitive for surface science studies. The difficulty was overcome by growing anatase films, mostly with (001) orientation, on $SrTiO_3$ or $LaAlO_3$ substrates by hydrothermal synthesis,[140] or pulsed laser deposition,[141,142] also in our group.[143] The (001) surface of anatase is thought to be the reactive face, although it covers a substantially smaller surface fraction of anatase particles compared to the predominant (101) surface.[144] In ultrahigh vacuum, the reactive (001) surface is stabilized by a (4×1) reconstruction, which dramatically reduces its reactivity.[145] The surface is, however, expected to be unreconstructed in liquid.[146,147] Preliminary experiments demonstrated the retention of the (4×1) reconstruction upon immersion in liquid H_2O, in agreement with ref. [140]. A possible chemical route to prepare the (1×1)-terminated anatase (001) surface by immersion to the solution of carboxylic acid has been reported recently.[140] The proposed experiment would proceed in three steps. First, a UHV-prepared anatase (4×1) would be immersed in carboxylic acid solution in order to lift the reconstruction. Second, after reinsertion to UHV, the sample would be heated to an intermediate temperature (to be determined), sufficient to thermally desorb carboxylates from the surface but below the temperature required to activate the formation of the (4×1) reconstruction. In the last step, the unreconstructed, and presumably clean surface would be exposed to liquid water using the established experimental procedure.

The capability of the newly-designed apparatus might be further explored by investigating the interaction of liquid water with other materials and surfaces; experiments on various polymorphs of iron oxides are currently under way. Also, the setup is portable and can be adapted for other UHV chambers to access more analysis techniques, such as non-contact AFM for investigations of non-conductive samples. As outlined in the thesis, the apparatus could be used to perform more complex experiments, involving other chemical substances besides water. Furthermore, the purity of experiments might be further refined by modifications of the setup, such as passivation of surfaces exposed to water with inert coating.

References

1. Henrich, V. E. & Cox, P. A. *The Surface Science of Metal Oxides* (Cambridge University Press, 1994).
2. Setvin, M., Wagner, M., Schmid, M., Parkinson, G. S. & Diebold, U. Surface point defects on bulk oxides: atomically-resolved scanning probe microscopy. *Chemical Society Reviews* **46,** 1772–1784 (2017).
3. Henrich, V. E. The surfaces of metal oxides. *Reports on Progress in Physics* **48,** 1481 (1985).
4. Watts, J. F. & Wolstenholme, J. *An Introduction to Surface Analysis by XPS and AES* (John Wiley & Sons, Ltd, Chichester, 2003).
5. Oura, K., Lifshits, V. G., Saranin, A. A., Zotov, A. V. & Katayama, M. *Surface science : an introduction* (Springer, Berlin, 2003).
6. Freund, H.-J., Kuhlenbeck, H. & Staemmler, V. Oxide Surfaces. *Reports on Progress in Physics* **59,** 283 (1996).
7. Gong, X.-Q., Selloni, A., Batzill, M. & Diebold, U. Steps on anatase TiO_2(101). *Nature Materials* **5,** 665 (2006).
8. Tuller, H. L. & Bishop, S. R. Point Defects in Oxides: Tailoring Materials Through Defect Engineering. *Annual Review of Materials Research* **41,** 369–398 (2011).
9. Diebold, U. The surface science of titanium dioxide. *Surface Science Reports* **48,** 53–229 (2003).
10. Hanaor, D. A. H. & Sorrell, C. C. Review of the anatase to rutile phase transformation. *Journal of Materials Science* **46,** 855–874 (2011).
11. Li, J.-G. & Ishigaki, T. Brookite-rutile phase transformation of TiO_2 studied with monodispersed particles. *Acta Materialia* **52,** 5143–5150 (2004).

12. Grant, F. A. Properties of Rutile (Titanium Dioxide). *Reviews of Modern Physics* **31,** 646–674 (1959).

13. Li, M., Hebenstreit, W., Diebold, U., Tyryshkin, A. M., Bowman, M. K., Dunham, G. G. & Henderson, M. A. The influence of the bulk reduction state on the surface structure and morphology of rutile TiO_2(110) single crystals. *Journal of Physical Chemistry B* **104,** 4944–4950 (2000).

14. Meinhold, G. Rutile and its applications in earth sciences. *Earth-Science Reviews* **102,** 1–28 (2010).

15. Shannon, R. D., Shannon, R. C., Medenbach, O. & Fischer, R. X. Refractive Index and Dispersion of Fluorides and Oxides. *Journal of Physical and Chemical Reference Data* **31,** 931–970 (2002).

16. Henderson, M. A. A surface science perspective on TiO_2 photocatalysis. *Surface Science Reports* **66,** 185–297 (2011).

17. Fujishima, A. & Honda, K. Electrochemical Photolysis of Water at a Semiconductor Electrode. *Nature* **238,** 37 (1972).

18. Mills, A., Davies, R. H. & Worsley, D. Water purification by semiconductor photocatalysis. *Chemical Society Reviews* **22,** 417–425 (1993).

19. Fujishima, A., Zhang, X. & Tryk, D. A. TiO_2 photocatalysis and related surface phenomena. *Surface Science Reports* **63,** 515–582 (2008).

20. O'Regan, B. & Grätzel, M. A low-cost, high-efficiency solar cell based on dye-sensitized colloidal TiO_2 films. *Nature* **353,** 737 (1991).

21. Ramamoorthy, M., Vanderbilt, D. & Kingsmith, R. D. 1st-Principles Calculations of the Energetics of Stoichiometric TiO_2 Surfaces. *Physical Review B* **49,** 16721–16727 (1994).

22. Onishi, H. & Iwasawa, Y. Reconstruction of TiO_2(110) Surface - STM Study with Atomic-Scale Resolution. *Surface Science* **313,** L783–L789 (1994).

23. Torrelles, X., Cabailh, G., Lindsay, R., Bikondoa, O., Roy, J., Zegenhagen, J., Teobaldi, G., Hofer, W. A. & Thornton, G. Geometric Structure of TiO_2(011)(2×1). *Physical Review Letters* **101,** 185501 (2008).

24. Dulub, O., Di Valentin, C., Selloni, A. & Diebold, U. Structure, defects, and impurities at the rutile TiO_2(011)-(2×1) surface: A scanning tunneling microscopy study. *Surface Science* **600,** 4407–4417 (2006).

25. Wandelt, K. & Thurgate, S. *Solid-Liquid Interfaces* (Springer-Verlag, Berlin ; Heidelberg, 2003).

26. Thiel, P. A. & Madey, T. E. The Interaction of Water with Solid-Surfaces - Fundamental-Aspects. *Surface Science Reports* **7,** 211–385 (1987).

27. Ketteler, G., Yamamoto, S., Bluhm, H., Andersson, K., Starr, D. E., Ogletree, D. F., Ogasawara, H., Nilsson, A. & Salmeron, M. The nature of water nucleation sites on TiO_2(110) surfaces revealed by ambient pressure X-ray photoelectron spectroscopy. *Journal of Physical Chemistry C* **111,** 8278–8282 (2007).

28. Henderson, M. A. The interaction of water with solid surfaces: fundamental aspects revisited. *Surface Science Reports* **46,** 1–308 (2002).

29. Hodgson, A. & Haq, S. Water adsorption and the wetting of metal surfaces. *Surface Science Reports* **64,** 381–451 (2009).

30. Mu, R. T., Zhao, Z. J., Dohnalek, Z. & Gong, J. L. Structural motifs of water on metal oxide surfaces. *Chemical Society Reviews* **46,** 1785–1806 (2017).

31. Fenter, P. & Sturchio, N. C. Mineral-water interfacial structures revealed by synchrotron X-ray scattering. *Progress in Surface Science* **77,** 171–258 (2004).

32. Franking, R. & Hamers, R. J. Ultraviolet-Induced Grafting of Alkenes to TiO_2 Surfaces: Controlling Multilayer Formation. *Journal of Physical Chemistry C* **115,** 17102–17110 (2011).

33. Makowski, M. J., Galhenage, R. P., Langford, J. & Hemminger, J. C. Liquid-Jet X-ray Photoelectron Spectra of TiO_2 Nanoparticles in an Aqueous Electrolyte Solution. *Journal of Physical Chemistry Letters* **7,** 1732–1735 (2016).

34. Salmeron, M., Bluhm, H., Tatarkhanov, M., Ketteler, G., Shimizu, T. K., Mugarza, A., Deng, X., Herranz, T., Yamamoto, S. & Nilsson, A. Water growth on metals and oxides: binding, dissociation and role of hydroxyl groups. *Faraday Discussions* **141,** 221–229 (2009).

35. Yamamoto, S., Bluhm, H., Andersson, K., Ketteler, G., Ogasawara, H., Salmeron, M. & Nilsson, A. In situ X-ray photoelectron spectroscopy studies of water on metals and oxides at ambient conditions. *Journal of Physics: Condensed Matter* **20,** 184025 (2008).

36. Freund, H. J., Kuhlenbeck, H., Libuda, J., Rupprechter, G., Bäumer, M. & Hamann, H. Bridging the pressure and materials gaps between catalysis and surface science: clean and modified oxide surfaces. *Topics in Catalysis* **15,** 201–209 (2001).

37. Kendelewicz, T., Kaya, S., Newberg, J. T., Bluhm, H., Mulakaluri, N., Moritz, W., Scheffler, M., Nilsson, A., Pentcheva, R. & Brown, G. E. X-ray Photoemission and Density Functional Theory Study of the Interaction of Water Vapor with the Fe_3O_4(001) Surface at Near-Ambient Conditions. *Journal of Physical Chemistry C* **117,** 2719–2733 (2013).

38. Hoster, H. E. & Gasteiger, H. A. in *Handbook of Fuel Cells - Fundamentals, Technology and Applications* (eds Vielstich, W., Lamm, A. & Gasteiger, A. H.) 236–265 (John Wiley & Sons, Ltd, Chichester, 2003).

39. Gardin, D. E. & Somorjai, G. A. Ultrahigh-Vacuum Chamber Equipped with a Reaction Cell for Studying Liquid-Phase Catalytic Reactions. *Review of Scientific Instruments* **64,** 1304–1308 (1993).

40. Leung, L. W. H., Gregg, T. W. & Goodman, D. W. A New Combined Ultrahigh-Vacuum and Electrochemical Apparatus. *Review of Scientific Instruments* **62,** 1857–1858 (1991).

41. Faisal, F., Bertram, M., Stumm, C., Cherevko, S., Geiger, S., Kasian, O., Lykhach, Y., Lytken, O., Mayrhofer, K. J. J., Brummel, O. & Libuda, J. Atomically Defined Co_3O_4(111) Thin Films Prepared in Ultrahigh Vacuum: Stability under Electrochemical Conditions. *Journal of Physical Chemistry C* **122,** 7236–7248 (2018).

42. Hoster, H., Iwasita, T., Baumgartner, H. & Vielstich, W. Current-time behavior of smooth and porous PtRu surfaces for methanol oxidation. *Journal of the Electrochemical Society* **148,** A496–A501 (2001).

43. Aberdam, D., Durand, R., Faure, R. & Elomar, F. Structural-Changes of a Pt(111) Electrode Induced by Electrosorption of Oxygen in Acidic Solutions - a Coupled Voltammetry, LEED and AES Study. *Surface Science* **171,** 303–330 (1986).

44. Borup, R. L., Sauer, D. E. & Stuve, E. M. An Ex-Situ Study of Electrodeposited Lead on Platinum(111) .1. Examination of the Surface Redox Behavior of Lead and Dynamic Emersion. *Surface Science* **293,** 10–26 (1993).

45. Grumelli, D., Wurster, B., Stepanow, S. & Kern, K. Bio-inspired nanocatalysts for the oxygen reduction reaction. *Nature Communications* **4,** 2904 (2013).

46. Hoster, H., Iwasita, T., Baumgartner, H. & Vielstich, W. Pt-Ru model catalysts for anodic methanol oxidation: Influence of structure and composition on the reactivity. *Physical Chemistry Chemical Physics* **3,** 337–346 (2001).

47. Schnaidt, J., Beckord, S., Engstfeld, A. K., Klein, J., Brimaud, S. & Behm, R. J. A combined UHV-STM-flow cell set-up for electrochemical/electrocatalytic studies of structurally well-defined UHV prepared model electrodes. *Physical Chemistry Chemical Physics* **19,** 4166–4178 (2017).

48. Reniers, F. The development of a transfer mechanism between UHV and electrochemistry environments. *Journal of Physics D-Applied Physics* **35,** R169–R188 (2002).

49. Binnig, G. & Rohrer, H. Scanning Tunneling Microscopy. *Surface Science* **126,** 236–244 (1983).

50. Chen, C. *Introduction to Scanning Tunneling Microscopy* (Oxford University Press, 1993).

51. Tersoff, J. & Lang, N. D. in *Scanning Tunneling Microscopy* (eds Stroscio, J. A. & Kaiser, W. J.) 1–29 (Academic Press, San Diego, 1993).

52. Wiesendanger, R. *Scanning probe microscopy and spectroscopy : methods and applications* (Cambridge University Press, Cambridge England ; New York, 1994).

53. Schmid, M. *Experimental Methods of Surface Physics* (TU Wien, Institute of Applied Physics, 2018).

54. Schmid, M. & Varga, P. in *The Chemical Physics of Solid Surfaces* (ed Woodruff, D. P.) 1st ed., 118–151 (Elsevier, 2002).

55. Hebenstreit, E. L. D., Hebenstreit, W., Schmid, M. & Varga, P. $Pt_{25}Rh_{75}$(111), (110), and (100) studied by scanning tunnelling microscopy with chemical contrast. *Surface Science* **441,** 441–453 (1999).

56. Diebold, U., Anderson, J. F., Ng, K. O. & Vanderbilt, D. Evidence for the tunneling site on transition-metal oxides: TiO_2(110). *Physical Review Letters* **77,** 1322–1325 (1996).

57. Schmid, M. & Varga, P. Analysis of Vibration-Isolating Systems for Scanning Tunneling Microscopes. *Ultramicroscopy* **42,** 1610–1615 (1992).

58. Laegsgaard, E., Osterlund, L., Thostrup, P., Rasmussen, P. B., Stensgaard, I. & Besenbacher, F. A high-pressure scanning tunneling microscope. *Review of Scientific Instruments* **72,** 3537–3542 (2001).

59. Herbschleb, C. T., van der Tuijn, P. C., Roobol, S. B., Navarro, V., Bakker, J. W., Liu, Q., Stoltz, D., Canas-Ventura, M. E., Verdoes, G., van Spronsen, M. A., Bergman, M., Crama, L., Taminiau, I., Ofitserov, A., van Baarle, G. J. C. & Frenken, J. W. M. The ReactorSTM: Atomically resolved scanning tunneling microscopy under high-pressure, high-temperature catalytic reaction conditions. *Review of Scientific Instruments* **85,** 083703 (2014).

60. Rossler, M., Geng, P. & Wintterlin, J. A high-pressure scanning tunneling microscope for studying heterogeneous catalysis. *Review of Scientific Instruments* **76,** 023705 (2005).

61. Tao, F., Tang, D., Salmeron, M. & Somorjai, G. A. A new scanning tunneling microscope reactor used for high-pressure and high-temperature catalysis studies. *Review of Scientific Instruments* **79,** 084101 (2008).

62. Gentz, K. & Wandelt, K. Electrochemical Scanning Tunneling Microscopy. *Chimia* **66,** 44–51 (2012).

63. Yanson, Y. I., Schenkel, F. & Rost, M. J. Design of a high-speed electrochemical scanning tunneling microscope. *Review of Scientific Instruments* **84,** 023702 (2013).

64. Magnussen, O. M., Zitzler, L., Gleich, B., Vogt, M. R. & Behm, R. J. In-situ atomic-scale studies of the mechanisms and dynamics of metal dissolution by high-speed STM. *Electrochimica Acta* **46,** 3725–3733 (2001).

65. Rost, M. J., Crama, L., Schakel, P., van Tol, E., van Velzen-Williams, G. B. E. M., Overgauw, C. F., ter Horst, H., Dekker, H., Okhuijsen, B., Seynen, M., Vijftigschild, A., Han, P., Katan, A. J., Schoots, K., Schumm, R., van Loo, W., Ooster-

kamp, T. H. & Frenken, J. W. M. Scanning probe microscopes go video rate and beyond. *Review of Scientific Instruments* **76,** 053710 (2005).

66. Seah, M. P. & Dench, W. A. Quantitative electron spectroscopy of surfaces: A standard data base for electron inelastic mean free paths in solids. *Surface and Interface Analysis* **1,** 2–11 (1979).

67. Moulder, J. & Chastain, J. *Handbook of X-ray Photoelectron Spectroscopy: A Reference Book of Standard Spectra for Identification and Interpretation of XPS Data* (Physical Electronics Division, Perkin-Elmer Corporation, 1992).

68. Salmeron, M. & Schlogl, R. Ambient pressure photoelectron spectroscopy: A new tool for surface science and nanotechnology. *Surface Science Reports* **63,** 169–199 (2008).

69. Trotochaud, L., Head, A. R., Karslioglu, O., Kyhl, L. & Bluhm, H. Ambient pressure photoelectron spectroscopy: Practical considerations and experimental frontiers. *Journal of Physics: Condensed Matter* **29,** 053002 (2017).

70. Ogletree, D. F., Bluhm, H., Lebedev, G., Fadley, C. S., Hussain, Z. & Salmeron, M. A differentially pumped electrostatic lens system for photoemission studies in the millibar range. *Review of Scientific Instruments* **73,** 3872–3877 (2002).

71. Winter, B. & Faubel, M. Photoemission from liquid aqueous solutions. *Chemical Reviews* **106,** 1176–1211 (2006).

72. Weatherup, R. S., Eren, B., Hao, Y. B., Bluhm, H. & Salmeron, M. B. Graphene Membranes for Atmospheric Pressure Photoelectron Spectroscopy. *Journal of Physical Chemistry Letters* **7,** 1622–1627 (2016).

73. Lagally, M. G. & Martin, J. A. Instrumentation for Low-Energy Electron-Diffraction. *Review of Scientific Instruments* **54,** 1273–1288 (1983).

74. Niehus, H., Heiland, W. & Taglauer, E. Low-Energy Ion-Scattering at Surfaces. *Surface Science Reports* **17,** 213–303 (1993).

75. Halpegamage, S., Ding, P., Gong, X.-Q. & Batzill, M. Ordered Fe(II)Ti(IV)O_3 Mixed Monolayer Oxide on Rutile TiO_2(011). *ACS Nano* **9,** 8627–8636 (2015).

76. Gerhold, S., Wang, Z., Schmid, M. & Diebold, U. Stoichiometry-driven switching between surface reconstructions on $SrTiO_3$(001). *Surface Science* **621,** L1–L4 (2014).

77. Parkinson, G. S. Iron oxide surfaces. *Surface Science Reports* **71,** 272–365 (2016).

78. Stöger, B., Hieckel, M., Mittendorfer, F., Wang, Z. M., Schmid, M., Parkinson, G. S., Fobes, D., Peng, J., Ortmann, J. E., Limbeck, A., Mao, Z. Q., Redinger, J. & Diebold, U. Point defects at cleaved $Sr_{n+1}Ru_nO_{3n+1}$(001) surfaces. *Physical Review B* **90,** 165438 (2014).

79. Setvin, M., Reticcioli, M., Poelzleitner, F., Hulva, J., Schmid, M., Boatner, L. A., Franchini, C. & Diebold, U. Polarity compensation mechanisms on the perovskite surface $KTaO_3$(001). *Science* **359,** 572 (2018).

80. Schafhauser, M. *Projektarbeit über Nanostrukturen an Oberflächen* Project thesis. 2010.

81. Gullikson, E. M. *X-ray Interactions With Matter* <http://henke.lbl.gov/optical_constants/filter2.html> (1995-2010).

82. Krause, M. O. & Ferreira, J. G. K X-ray-Emission Spectra of Mg and Al. *Journal of Physics B-Atomic Molecular and Optical Physics* **8,** 2007–2014 (1975).

83. Cope, J. O. Production of Low Pressures with Sorption Pumps. *Vacuum* **18,** 665 (1968).

84. LenoxLaser. *Fluid Flow Through Calibrated Orifices* <https://lenoxlaser.com/resources/calculators/orifice-calculator/> (2015).

85. Kraushofer, F., Balajka, J., Müllner, M., Resch, N., Jakub, Z., Hulva, J., Meier, M., Schmid, M., Diebold, U. & Parkinson, G. S. *Stability of the Magnetite Fe_3O_4(001) ($\sqrt{2} \times \sqrt{2}$)R45° Reconstruction in Liquid and Ambient Pressure Water* in preparation. 2018.

86. Jakub, Z. *UHV-EC transfer system for electrochemical surface science studies* Master thesis. 2016.

87. Balajka, J., Pavelec, J., Komora, M., Schmid, M. & Diebold, U. Apparatus for dosing liquid water in ultrahigh vacuum. *Review of Scientific Instruments* **89.** https://doi.org/10.1063/1.5046846 (2018).

88. Glasser, L. Water, water, everywhere - Phase diagrams of ordinary water substance. *Journal of Chemical Education* **81,** 414–418 (2004).

89. Schmid, M. *Vapor pressure calculator [online]* <http://www.iap.tuwien.ac.at/www/surface/vapor_pressure> (2018).

90. Preston-Thomas, H. The International Temperature Scale of 1990 (ITS-90). *Metrologia* **27,** 3 (1990).

91. Wagner, W. & Pruss, A. International Equations for the Saturation Properties of Ordinary Water Substance. Revised According to the International Temperature Scale of 1990. Addendum to J. Phys. Chem. Ref. Data 16, 893 (1987). *Journal of Physical and Chemical Reference Data* **22,** 783–787 (1993).

92. Reutemann, W. & Kieczka, H. Formic acid. *Ullmann's Encyclopedia of Industrial Chemistry* (2000).

93. Chambers, S. A., Henderson, M. A., Kim, Y. J. & Thevuthasan, S. Chemisorption geometry, vibrational spectra, and thermal desorption of formic acid on TiO_2(110). *Surface Review and Letters* **5,** 381–385 (1998).

94. Balajka, J., Hines, M. A., DeBenedetti, W. J. I., Komora, M., Pavelec, J., Schmid, M. & Diebold, U. High Affinity Adsorption leads to Molecularly Ordered Interfaces on TiO_2 in Air and Solution. *Science.* doi: 10.1126/science.aat6752 (2018).

95. Zubkov, T., Stahl, D., Thompson, T. L., Panayotov, D., Diwald, O. & Yates, J. J. T. Ultraviolet light-induced hydrophilicity effect on TiO_2(110)(1×1). Dominant role of the photooxidation of adsorbed hydrocarbons causing wetting by water droplets. *Journal of Physical Chemistry B* **109,** 15454–15462 (2005).

96. Hussain, H., Tocci, G., Woolcot, T., Torrelles, X., Pang, C. L., Humphrey, D. S., Yim, C. M., Grinter, D. C., Cabailh, G., Bikondoa, O., Lindsay, R., Zegenhagen, J., Michaelides, A. & Thornton, G. Structure of a model TiO_2 photocatalytic interface. *Nat Mater* **16,** 461–466 (2017).

97. Serrano, G., Bonanni, B., Di Giovannantonio, M., Kosmala, T., Schmid, M., Diebold, U., Di Carlo, A., Cheng, J., VandeVondele, J., Wandelt, K. & Goletti, C. Molecular Ordering at the Interface Between Liquid Water and Rutile TiO_2(110). *Advanced Materials Interfaces* **2,** 1500246 (2015).

98. Sasahara, A. & Tomitori, M. An Atomic-Scale Study of TiO_2(110) Surfaces Exposed to Humid Environments. *Journal of Physical Chemistry C* **120,** 21427–21435 (2016).

99. Song, A. Q., Skibinski, E. S., DeBenedetti, W. J. I., Ortoll-Bloch, A. G. & Hines, M. A. Nanoscale Solvation Leads to Spontaneous Formation of a Bicarbonate Monolayer on Rutile (110) under Ambient Conditions: Implications for CO_2 Photoreduction. *Journal of Physical Chemistry C* **120,** 9326–9333 (2016).

100. Wendt, S., Schaub, R., Matthiesen, J., Vestergaard, E. K., Wahlström, E., Rasmussen, M. D., Thostrup, P., Molina, L. M., Laegsgaard, E., Stensgaard, I., Hammer, B. & Besenbacher, F. Oxygen vacancies on TiO_2(110) and their interaction with H_2O and O_2: A combined high-resolution STM and DFT study. *Surface Science* **598,** 226–245 (2005).

101. Wagner, C. D., Davis, L. E., Zeller, M. V., Taylor, J. A., Raymond, R. H. & Gale, L. H. Empirical atomic sensitivity factors for quantitative analysis by electron spectroscopy for chemical analysis. *Surface and Interface Analysis* **3,** 211–225 (1981).

102. Wagner, C. D. Sensitivity factors for XPS analysis of surface atoms. *Journal of Electron Spectroscopy and Related Phenomena* **32,** 99–102 (1983).

103. Wolff, M., Schultze, J. W. & Strehblow, H.-H. Low-energy implantation and sputtering of TiO_2 by nitrogen and argon and the electrochemical reoxidation. *Surface and Interface Analysis* **17,** 726–736 (1991).

104. Thomas, A. G. & Syres, K. L. Adsorption of organic molecules on rutile TiO_2 and anatase TiO_2 single crystal surfaces. *Chemical Society Reviews* **41,** 4207–4217 (2012).

105. Cocks, I. D., Guo, Q., Patel, R., Williams, E. M., Roman, E. & de Segovia, J. L. The structure of TiO_2(110) (1×1) and (1×2) surfaces with acetic acid adsorption - a PES study. *Surface Science* **377-379,** 135–139 (1997).

106. Grinter, D. C., Woolcot, T., Pang, C.-L. & Thornton, G. Ordered Carboxylates on TiO_2(110) Formed at Aqueous Interfaces. *Journal of Physical Chemistry Letters* **5,** 4265–4269 (2014).

107. Guo, Q., Cocks, I. & Williams, E. M. The adsorption of benzoic acid on a TiO_2(110) surface studied using STM, ESDIAD and LEED. *Surface Science* **393,** 1–11 (1997).

108. Skibinski, E. S., Song, A., DeBenedetti, W. J. I., Ortoll-Bloch, A. G. & Hines, M. A. Solution Deposition of Self-Assembled Benzoate Monolayers on Rutile (110): Effect of π-π Interactions on Monolayer Structure. *Journal of Physical Chemistry C* **120,** 11581–11589 (2016).

109. Wulser, K. W. & Langell, M. A. Carboxylic acid adsorption on NiO(100) characterized by X-ray photoelectron and high resolution electron energy loss spectroscopies. *Catalysis Letters* **15,** 39–50 (1992).

110. England, A. H., Duffin, A. M., Schwartz, C. P., Uejio, J. S., Prendergast, D. & Saykally, R. J. On the hydration and hydrolysis of carbon dioxide. *Chemical Physics Letters* **514,** 187–195 (2011).

111. Loerting, T., Tautermann, C., Kroemer, R. T., Kohl, I., Hallbrucker, A., Mayer, E. & Liedl, K. R. On the Surprising Kinetic Stability of Carbonic Acid (H2CO3). *Angewandte Chemie International Edition* **39,** 891–894 (2000).

112. Khare, P., Kumar, N., Kumari, K. M. & Srivastava, S. S. Atmospheric formic and acetic acids: An overview. *Reviews of Geophysics* **37,** 227–248 (1999).

113. Johnson, B. J., Betterton, E. A. & Craig, D. Henry's law coefficients of formic and acetic acids. *Journal of Atmospheric Chemistry* **24,** 113–119 (1996).

114. Heikes, B. G., Chang, W., Pilson, M. E. Q., Swift, E., Singh, H. B., Guenther, A., Jacob, D. J., Field, B. D., Fall, R., Riemer, D. & Brand, L. Atmospheric methanol budget and ocean implication. *Global Biogeochemical Cycles* **16,** 1133 (2002).

115. Li, Z., Smith, R. S., Kay, B. D. & Dohnálek, Z. Determination of Absolute Coverages for Small Aliphatic Alcohols on TiO_2(110). *Journal of Physical Chemistry C* **115,** 22534–22539 (2011).

116. Farfan-Arribas, E. & Madix, R. J. Characterization of the Acid-Base Properties of the TiO_2(110) Surface by Adsorption of Amines. *Journal of Physical Chemistry B* **107,** 3225–3233 (2003).

117. Henderson, M. A. Complexity in the Decomposition of Formic Acid on the TiO_2(110) Surface. *Journal of Physical Chemistry B* **101,** 221–229 (1997).

118. Wang, R., Hashimoto, K., Fujishima, A., Chikuni, M., Kojima, E., Kitamura, A., Shimohigoshi, M. & Watanabe, T. Light-induced amphiphilic surfaces. *Nature* **388,** 431 (1997).

119. Yates, J. T. Photochemistry on TiO_2: Mechanisms behind the surface chemistry. *Surface Science* **603,** 1605–1612 (2009).

120. Balajka, J., Aschauer, U., Mertens, S. F. L., Selloni, A., Schmid, M. & Diebold, U. Surface Structure of TiO_2 Rutile (011) Exposed to Liquid Water. *Journal of Physical Chemistry C* **121,** 26424–26431 (2017).

121. Ohno, T., Sarukawa, K. & Matsumura, M. Crystal faces of rutile and anatase TiO_2 particles and their roles in photocatalytic reactions. *New Journal of Chemistry* **26,** 1167–1170 (2002).

122. Gong, X. Q., Khorshidi, N., Stierle, A., Vonk, V., Ellinger, C., Dosch, H., Cheng, H. Z., Selloni, A., He, Y. B., Dulub, O. & Diebold, U. The 2×1 reconstruction of the rutile TiO_2(011) surface: A combined density functional theory, X-ray diffraction, and scanning tunneling microscopy study. *Surface Science* **603,** 138–144 (2009).

123. Aschauer, U. & Selloni, A. Structure of the Rutile TiO_2(011) Surface in an Aqueous Environment. *Physical Review Letters* **106,** 166102 (2011).

124. Di Valentin, C., Tilocca, A., Selloni, A., Beck, T. J., Klust, A., Batzill, M., Losovyj, Y. & Diebold, U. Adsorption of water on reconstructed rutile TiO_2(011)-(2×1): Ti=O double bonds and surface reactivity. *Journal of the American Chemical Society* **127,** 9895–9903 (2005).

125. He, Y. B., Li, W. K., Gong, X. Q., Dulub, O., Selloni, A. & Diebold, U. Nucleation and Growth of 1D Water Clusters on Rutile TiO_2(011)-2×1. *Journal of Physical Chemistry C* **113,** 10329–10332 (2009).

126. Woolcot, T., Teobaldi, G., Pang, C. L., Beglitis, N. S., Fisher, A. J., Hofer, W. A. & Thornton, G. Scanning Tunneling Microscopy Contrast Mechanisms for TiO_2. *Physical Review Letters* **109,** 156105 (2012).

127. Choi, J. I. J., Mayr-Schmölzer, W., Mittendorfer, F., Redinger, J., Diebold, U. & Schmid, M. The growth of ultra-thin zirconia films on Pd_3Zr(0001). *Journal of Physics: Condensed Matter* **26,** 225003 (2014).

128. Tao, J., Luttrell, T., Bylsma, J. & Batzill, M. Adsorption of Acetic Acid on Rutile TiO_2(110) vs (011)-2×1 Surfaces. *Journal of Physical Chemistry C* **115,** 3434–3442 (2011).

129. Halpegamage, S., Wen, Z. H., Gong, X. Q. & Batzill, M. Monolayer Intermixed Oxide Surfaces: Fe, Ni, Cr, and V Oxides on Rutile TiO_2(011). *Journal of Physical Chemistry C* **120,** 14782–14794 (2016).

130. Halpegamage, S., Bignardi, L., Lacovig, P., Kramer, A., Wen, Z.-H., Gong, X.-Q., Lizzit, S. & Batzill, M. An Ordered Mixed Oxide Monolayer Formed by Iron Segregation on Rutile-TiO_2(011): Structural Determination by X-ray Photoelectron Diffraction. *Journal of Physical Chemistry C* **120,** 26414–26424 (2016).

131. Halpegamage, S. & Batzill, M. Mixed oxides on rutile TiO_2(011): Cr_2O_3 and Cu_2O. *Journal of Vacuum Science & Technology A* **35,** 061406 (2017).

132. Hammond, C. *The Basics of Crystallography and Diffraction* (Oxford University Press, 2001).

133. Heinz, K. & Starke, U. in *Surface and Interface Science, Volume 2: Properties of Elemental Surfaces* (ed Wandelt, K.) 489–569 (Wiley-VCH, Weinheim, 2012).

134. Van Hove, M. A., Weinberg, W. H. & Chan, C. M. *Low-energy electron diffraction : experiment, theory, and surface structure determination* (Springer-Verlag, Berlin ; New York, 1986).

135. Estrup, P. J. & McRae, E. G. Surface studies by electron diffraction. *Surface Science* **25,** 1–52 (1971).

136. Duszak, R. & Prince, R. H. Optical-Simulation of LEED Patterns. *Surface Science* **234,** L259–L263 (1990).

137. Luttrell, T., Halpegamage, S., Tao, J., Kramer, A., Sutter, E. & Batzill, M. Why is anatase a better photocatalyst than rutile? - Model studies on epitaxial TiO_2 films. *Scientific Reports* **4,** 4043 (2014).

138. Ohno, T., Sarukawa, K., Tokieda, K. & Matsumura, M. Morphology of a TiO_2 Photocatalyst (Degussa, P-25) Consisting of Anatase and Rutile Crystalline Phases. *Journal of Catalysis* **203,** 82–86 (2001).

139. Setvín, M., Daniel, B., Mansfeldova, V., Kavan, L., Scheiber, P., Fidler, M., Schmid, M. & Diebold, U. Surface preparation of TiO_2 anatase (101): Pitfalls and how to avoid them. *Surface Science* **626,** 61–67 (2014).

140. DeBenedetti, W. J. I., Skibinski, E. S., Jing, D., Song, A. & Hines, M. A. Atomic-Scale Understanding of Catalyst Activation: Carboxylic Acid Solutions, but Not the Acid Itself, Increase the Reactivity of Anatase (001) Faceted Nanocatalysts. *Journal of Physical Chemistry C* **122,** 4307–4314 (2018).

141. Yamamoto, S., Sumita, T., Sugiharuto, Miyashita, A. & Naramoto, H. Preparation of epitaxial TiO_2 films by pulsed laser deposition technique. *Thin Solid Films* **401,** 88–93 (2001).

142. Zhang, Z., Wong, L. M., Zhang, Z., Wu, Z., Wang, S., Chi, D., Hong, R. & Yang, W. Pulse laser deposition of epitaxial TiO_2 thin films for high-performance ultraviolet photodetectors. *Applied Surface Science* **355,** 398–402 (2015).

143. Moser, S. *Growth of anatase TiO_2(001) on $SrTiO_3$(001) using pulsed laser deposition* Master thesis. 2017.

144. Selloni, A. Anatase shows its reactive side. *Nature Materials* **7,** 613 (2008).

145. Lazzeri, M. & Selloni, A. Stress-Driven Reconstruction of an Oxide Surface: The Anatase TiO_2(001)-(1×4) Surface. *Physical Review Letters* **87,** 266105 (2001).

146. De Angelis, F., Di Valentin, C., Fantacci, S., Vittadini, A. & Selloni, A. Theoretical Studies on Anatase and Less Common TiO_2 Phases: Bulk, Surfaces, and Nanomaterials. *Chemical Reviews* **114,** 9708–9753 (2014).

147. Selcuk, S. & Selloni, A. Facet-dependent trapping and dynamics of excess electrons at anatase TiO_2 surfaces and aqueous interfaces. *Nature Materials* **15,** 1107 (2016).